JOURNAL OF PETROLOGY | VOLUME 54 | NUMBER 2 | PAGES 351–391 | 2013 | doi:10.1093/petrology/egs071

Geochemistry and Petrogenesis of Silicic Magmas in the Intra-Oceanic Kermadec Arc

S. J. BARKER[1]*, C. J. N. WILSON[1], J. A. BAKER[1], M.-A. MILLET[1], M. D. ROTELLA[1], I. C. WRIGHT[2] AND R. J. WYSOCZANSKI[1,3]

[1]SCHOOL OF GEOGRAPHY, ENVIRONMENT AND EARTH SCIENCES, VICTORIA UNIVERSITY OF WELLINGTON,
PO BOX 600, WELLINGTON 6140, NEW ZEALAND
[2]NATIONAL OCEANOGRAPHY CENTRE, UNIVERSITY OF SOUTHAMPTON WATERFRONT CAMPUS, EUROPEAN WAY,
SOUTHAMPTON SO14 3ZH, UK
[3]NATIONAL INSTITUTE OF WATER AND ATMOSPHERIC RESEARCH, PO BOX 14901, KILBIRNIE, WELLINGTON 6021,
NEW ZEALAND

RECEIVED MARCH 12, 2012; ACCEPTED SEPTEMBER 11, 2012
ADVANCE ACCESS PUBLICATION NOVEMBER 11, 2012

The geochemistry of pyroclasts sampled from four volcanoes along the Kermadec arc in the SW Pacific is used to investigate the genesis of silicic magmas in a young (<2 Myr), archetypical intra-oceanic arc setting. Raoul, Macauley and Raoul SW volcanoes in the northern Kermadec arc, and Healy volcano in the southern Kermadec arc have all recently erupted dacitic to rhyolitic crystal-poor pumice. In addition to whole-rock analyses, we present a detailed study of mineral and glass chemistries to highlight the complex structure of the Kermadec magmatic systems. Major and trace element bulk-rock compositions mostly fall into relatively narrow compositional ranges, forming discrete groups by eruption for Raoul, and varying with relative crystal contents for Healy. In contrast, pumices from Macauley cover a wide range of compositions, between 66 and 72·5 wt % SiO_2. At all four volcanoes the trace element patterns of pumice are subparallel to both those of previously erupted basalts and/or whole mafic blebs found both as discrete pyroclasts and as inclusions within pumices. Pb and Sr isotopic compositions have limited ranges within single volcanoes, but vary considerably along the arc, being more radiogenic in the southern volcanoes. Distinctive crystal populations and zonation patterns in pumices, mafic blebs and plutonic xenoliths indicate that many crystals did not grow in the evolved magmas, but are instead mixed from other sources including gabbros and hydrothermally altered tonalites. Such open-system mixing is ubiquitous at the four volcanoes. Oxygen isotope compositions of both phenocrysts (silicic origin) and xenocrysts or antecrysts (mafic origin) are typical for mantle-derived melts. Whole-rock, glass and mineral chemistries are consistent with evolved magmas being generated at each volcano through ~70–80% crystal fractionation of a basaltic parent. Our results are not consistent with silicic magma generation via crustal anatexis, as previously suggested for these Kermadec arc volcanoes. Although crystallization is the dominant process driving melt evolution in the Kermadec volcanoes, we show that the magmatic systems are open to contributions from both newly arriving melts and wholly crystalline plutonic bodies. Such processes occur in variable proportions between magma batches, and are largely reflected in small-scale chemical variations between eruption units.

KEY WORDS: *fractional crystallization; Kermadec; magma mixing; oceanic arc, anatexis*

INTRODUCTION

The eruption of silicic magmas (dacite or rhyolite; >63 wt % SiO_2) is widely recognised as a prominent feature of intra-oceanic arc systems (e.g. Devine, 1995; Leat *et al.*, 2003; Smith *et al.*, 2003*a*, 2003*b*, 2006; Wright *et al.*, 2003, 2006; Shukuno *et al.*, 2006; Tani *et al.*, 2008; Tamura *et al.*, 2009). In contrast to continental settings, the oceanic arc crust is generally thinner and mafic in composition, and the ascending magmas have less opportunity to stall

---

*Corresponding author. Telephone: (+64) 4 463 9510. Fax: (+64) 4 463 5186. E-mail: smnbarker@gmail.com and differentiate (Tatsumi & Eggins, 1995). Important questions therefore arise as to how significant volumes of silicic magmas are produced, stored, and erupted in intra-oceanic arc settings.

In general, there are two end-member processes that can generate silicic magmas in oceanic arcs: (1) polybaric fractional crystallization, involving a range of different mineral phases, depending on pressure and composition (e.g. Sisson & Grove, 1993; Devine, 1995; Pearce *et al.*, 1995; Grove *et al.*, 2003; Sisson *et al.*, 2005; Wade *et al.*, 2005; Haase *et al.*, 2006, 2011; Brophy, 2008); (2) partial melting (anatexis) of pre-existing crust, which could be either a protolith of hornblende-rich diorite to granodiorite in the mid- to upper crust (e.g. Tamura & Tatsumi, 2002; Vogel *et al.*, 2004; Shukuno *et al.*, 2006; Tamura *et al.*, 2009) or a lower crustal mafic amphibolite (e.g. Smith *et al.*, 2003*a*, 2003*b*, 2006, 2010; Vogel *et al.*, 2006; Deering *et al.*, 2007). The relative importance of these two end-member processes in the generation of silicic magmas remains unclear, as the two processes are difficult to distinguish geochemically. In intra-oceanic arcs the dominant lower crustal lithologies are mainly mafic cumulates, gabbros and possibly amphibolite, with chemical and isotopic characteristics similar to those of their parental mantle-derived melts (Greene *et al.*, 2006; Brophy, 2008). This has made discrimination of fractional crystallization versus crustal melting models difficult, and studies of the same arcs have proposed contrasting views (e.g. South Sandwich arc: Pearce *et al.*, 1995; Leat *et al.*, 2003; Izu–Bonin–Mariana arc: Wade *et al.*, 2005; Tamura *et al.*, 2009). Brophy (2008), however, recently demonstrated that partial melting of amphibole-bearing crustal rocks should yield distinctive rare earth element (REE) patterns, and that REE patterns indicative of amphibolite melting are relatively uncommon in global examples of oceanic arc volcanoes.

The Kermadec arc (SW Pacific; Fig. 1) is an archetypical intra-oceanic arc where both amphibolite melting and fractional crystallization have been proposed to be primarily responsible for generating silicic magmas at single volcanoes. Smith *et al.* (2003*a*, 2003*b*, 2006, 2010) proposed that the absence of intermediate magmas, and large volumes of erupted silicic magmas and their aphyric nature in the northern Kermadec arc required an amphibolite melting model to produce such patterns of magmatism. In contrast, Haase *et al.* (2006) and Saunders *et al.* (2010) suggested that silicic magmas in the southern Kermadec arc could be produced by fractionation from a basaltic parent on the basis of major and trace element modelling. Here we present new petrological, geochemical and isotopic data from four volcanoes along the Kermadec arc to reassess silicic magma generation processes. In addition to bulk-rock analyses, *in situ* mineral and glass chemistry are used to investigate pre-eruptive magma storage conditions and to provide insights into the magmatic processes that produced the observed bulk-rock chemistry variations. We use these data, combined with the approach of Brophy (2008), to show that silicic melt generation in the Kermadec arc is primarily driven by open-system fractional crystallization, and that models involving crustal anatexis are not necessary to explain the observed compositional variations.

GEOLOGICAL SETTING AND SAMPLE COLLECTION

The Kermadec arc and associated Havre Trough represent the southern, 1200 km long section of the Tonga–Kermadec subduction system, associated with Pacific–Australian intra-oceanic plate convergence to the NE of New Zealand (Wright, 1993; Smith & Price, 2006; Fig. 1). The Kermadec arc consists dominantly of submarine volcanoes, with only Raoul, Macauley, Curtis and L'Esperance volcanoes being partially emergent (Fig. 1). The presence of silicic volcanism along the arc has long been recognised from subaerial deposits (e.g. Lloyd & Nathan, 1981; Lloyd *et al.*, 1996). However, not until detailed bathymetric mapping and submarine sampling was undertaken was it recognised that caldera-related, explosive silicic volcanism is widespread (Gamble *et al.*, 1993; Wright, 1994, 1996, 1997; Wright & Gamble, 1999; Haase *et al.*, 2002, 2006; Wright *et al.*, 2002, 2003, 2006; Graham *et al.*, 2008). Similar to other oceanic arc systems (e.g. Izu–Bonin: Tamura & Tatsumi, 2002; South Sandwich: Leat *et al.*, 2003), the erupted compositions show a bimodal distribution, with andesite being a relatively minor component volumetrically (Tamura & Wysoczanski, 2006).

The 2004 and 2007 research voyages of the R.V. *Tangaroa* (NZAPLUME III and TAN0706, respectively) sampled eruptive materials from four Kermadec volcanoes. Three of these (Healy, Macauley and Raoul; Fig. 1) have erupted silicic magmas within the last 10 kyr with associated caldera collapse (Lloyd & Nathan, 1981; Smith *et al.*, 1988, 2003*a*, 2006; Lloyd *et al.*, 1996; Worthington *et al.*, 1999; Wright *et al.*, 2003, 2006). In addition, opportunistic dredging at a fourth, newly discovered caldera volcano SW of Raoul Island recovered silicic pumice of unknown age but exceptional freshness. A brief geological summary of each volcano follows and a full sample list is presented in Electronic Appendix A (the electronic appendices are available for downloading at http://www.petrology.oxfordjournals.org).

Raoul volcano

Raoul is the northernmost emergent volcano in the Kermadec arc (Fig. 1). Raoul Island is the 30 km^2 emergent portion of a >200 km^3 edifice that rises 900 m from its base on the Kermadec ridge. Although the subaerial edifice of Raoul volcano is predominantly mafic in composition, in the past 4 kyr it has mainly produced dacitic

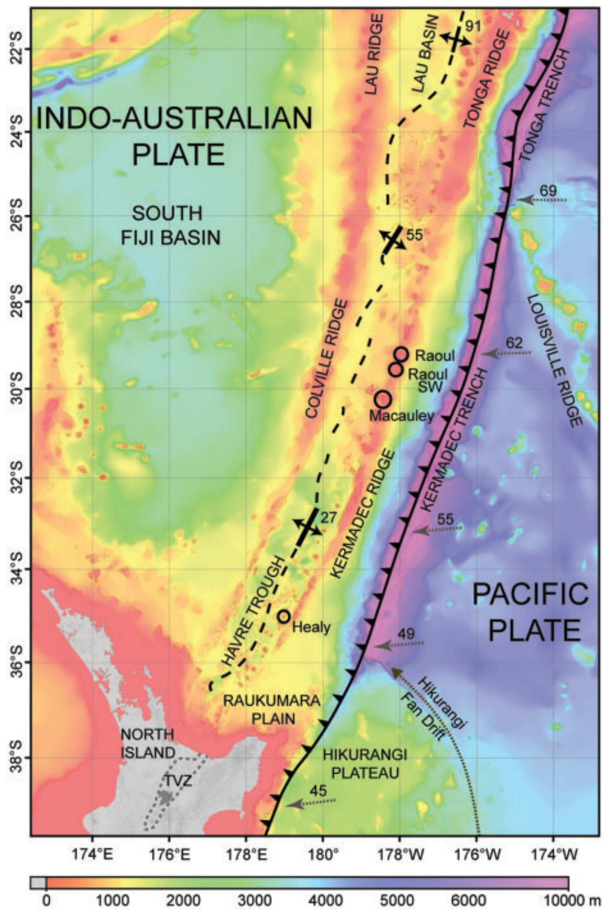

Fig. 1. Regional tectonic setting of the Tonga–Kermadec arc. Relative Pacific–Australian plate motions (mm a^{-1}) shown by arrows are from Wallace *et al.* (2009), after DeMets *et al.* (1994). Spreading axis marked by black dashed line in the Havre Trough and Lau Basin is from Wysoczanski *et al.* (2010). Modern Taupo Volcanic Zone (TVZ) dashed grey outline is from Wilson *et al.* (1995). The Hikurangi Fan Drift marks the direction of sediment drift into the Kermadec trench (from Carter *et al.*, 1996). The four volcanoes investigated in this study are marked by open circles.

eruptions, associated with development of two calderas (Lloyd & Nathan, 1981; Worthington *et al.*, 1999; Fig. 2a and b). Pumices and xenoliths were collected from fall deposits of the large caldera-related eruptions (Matatirohia, Oneraki, Fleetwood) in coastal exposures, and from localized fall deposits from the two youngest cone-forming eruptions (Green Lake, Rangitahua) from within Raoul caldera (Fig. 2b). In addition, we collected samples from a newly discovered unit of floated pumice blocks incorporated in lake sediments below the Green Lake Pumice deposit (Barker *et al.*, 2012).

Raoul SW volcano

EM300 multibeam mapping near Raoul Island in 2007 identified a previously unknown caldera volcano that Barker *et al.* (2012) informally named Raoul SW (Figs 1 and 2a). Raoul SW volcano has a 4 km diameter caldera, with a floor depth of ~1200 m and caldera walls reaching ~500 m high (Fig. 2a). Dredging of the volcano recovered a suite of exceptionally fresh pumice clasts, which, coupled with the pristine volcano morphology, are taken to be the product of recent explosive volcanism.

Macauley volcano

Macauley Island is the 3 km^2 emergent portion of a large submarine volcano (Lloyd *et al.*, 1996; Fig. 2c). The island is constructed dominantly of basaltic lavas and pyroclastic deposits, punctuated by deposition of dacitic ignimbrite during the 6·3 ^{14}C ka Sandy Bay eruption (Brothers & Martin, 1970; Lloyd *et al.*, 1996; Smith *et al.*, 2003*a*). Immediately NW of Macauley Island is the large, roughly circular ~11 km × 8 km Macauley caldera (Fig. 2c), interpreted to be formed during the Sandy Bay eruption (Latter *et al.*, 1992; Lloyd *et al.*, 1996; Smith *et al.*, 2003*a*), although Barker *et al.* (2012) presented evidence for the caldera being a composite feature. Pumice clasts and xenoliths were sampled from the subaerial Sandy Bay Tephra, and by dredging around the submarine volcano flanks and caldera rim (Fig. 2c).

Healy volcano

Healy is a composite volcanic complex consisting of a central edifice with a smaller caldera (1·3 km) on its upper SW flank and a ~2 km diameter caldera on the NE, mid- to lower flank (Wright & Gamble, 1999; Fig. 2d). The outer flanks of the volcanic complex, caldera floors and walls, and the main edifice are mantled with pumice deposits over >50 km^2 (Wright & Gamble, 1999; Wright, 2001; Wright *et al.*, 2003). The eruptive sequences at Healy are, however, unknown as only dredge samples are available. Samples from Healy were acquired by dredging inside the caldera, and down the central edifice flanks on both the NW and SE sides of the volcano (Fig. 2d).

ANALYTICAL TECHNIQUES

A summary of the analytical techniques is provided below. Further details and standards data are given in Electronic Appendix B.

Sample preparation

Most clasts chosen for analysis were large enough that all surface material could be removed, retaining only the fresh interior material, which was then crushed to <15 mm chips so that 'large' mafic inclusions and xenocrysts could be recovered. Seawater contamination was removed by repeated cleaning by boiling in Milli-Q ($>$18·2 MΩ) water until there was no remaining salt, tested by using the silver nitrate technique of Tani *et al.* (2003). Up to 120 g of cleaned dried material was then further crushed to 1–2 mm in a jaw crusher, of which ~30 g was powdered

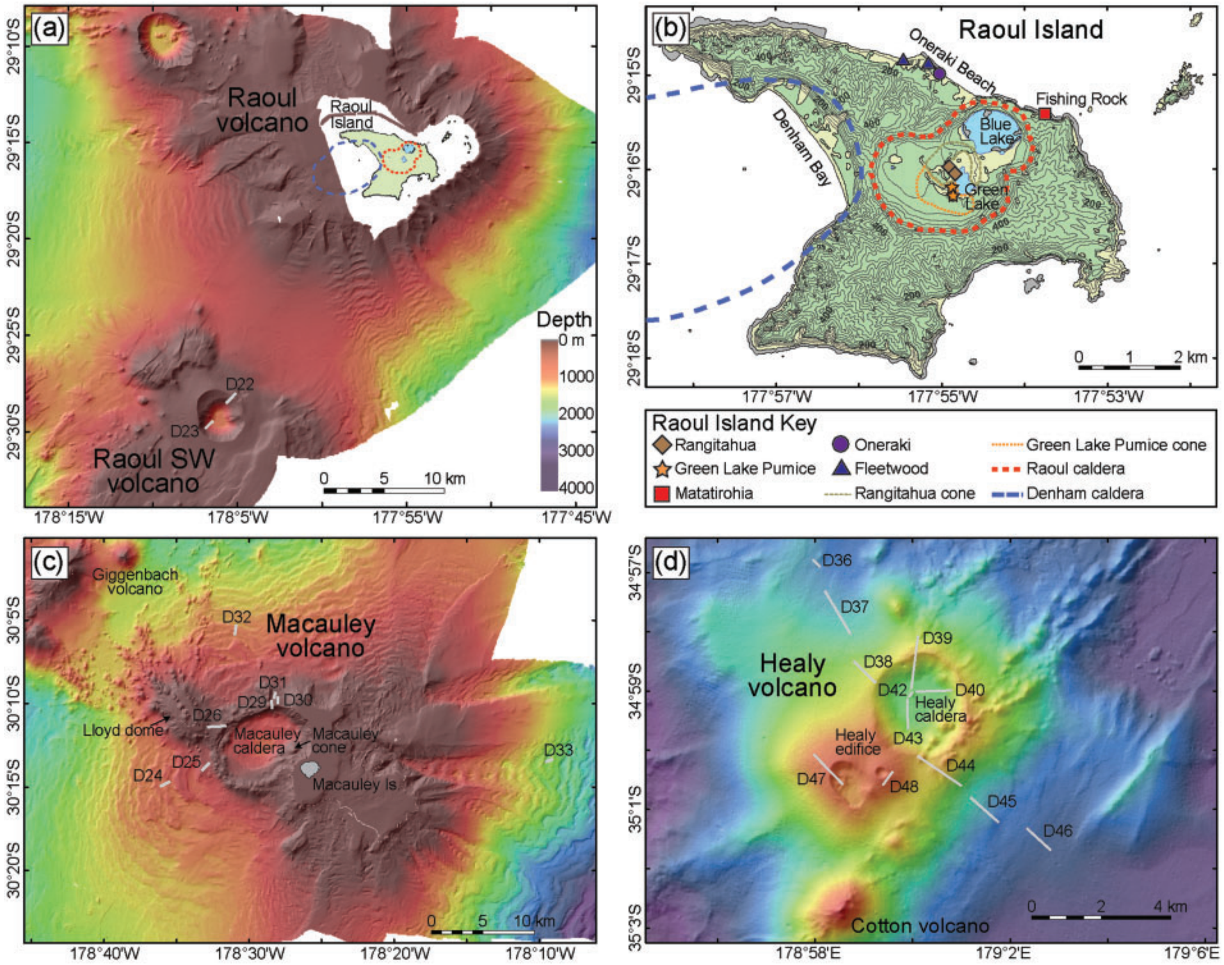

Fig. 2. Seafloor bathymetry, sample dredge sites and subaerial sample locations for the four volcanoes investigated. Dashed lines outline Denham and Raoul calderas. Bathymetry is from R.V. *Tangaroa* EM300 multibeam mapping (white areas lack multibeam data). Dredge locations are shown by light grey lines and labelled by dredge number. [Note the change in scale for map (d).]

in an agate Tema swing mill and used for whole-rock major, trace element and isotopic analyses.

Whole-rock major and trace element analysis

Major element data were measured by X-ray fluorescence (XRF) spectrometry. Whin Sill Dolerite (WS-E) and G94 (micro-granite) were measured at the beginning and end of each analytical run as internal standards. Two standard deviation (2 SD) analytical reproducibility, determined by 10 replicate analyses of the same standards, is generally <1–3 relative %. Average values are accurate to within <1–2% of the recommended values.

Trace element analyses were carried out by solution inductively coupled plasma mass spectrometry (ICP-MS) using methods similar to those of McCoy-West *et al.* (2010). ^{43}Ca was used to perform an internal correction, as CaO concentrations were known to ±1% from XRF. Diluted sample solutions were analysed using an Agilent 7500CS ICP-MS system at Victoria University of Wellington (VUW). Total procedural blanks were within background levels on all measured elements. Abundances of single trace elements were calculated by external normalization relative to a bracketing standard (BHVO-2), which was prepared and analysed under identical conditions to the samples. Approximate 2 SD analytical precisions derived from 13 replicate analyses of a secondary standard (BCR-2) are <±5% for most trace elements (exceptions are Zn ± 8·5%, Cu ± 8·8%, Cs ± 13·1%, Pb ± 13·7%, Ta ± 15·6% and Mo ± 43·4%). Most BCR-2 trace element analyses are accurate to ≤5 % (most are <1%), apart from Li, Cr and Ni, which are ≤10%.

Whole-rock Pb and Sr isotope analysis

Pb and Sr were chemically separated from samples in class 10 laminar flow hoods. Samples underwent leaching for 1 h in 1 M HCl at 120°C to remove anthropogenic Pb, and Sr contamination from seawater, prior to digestion (adapted from Millet *et al.*, 2008). Pb was separated using anion exchange techniques by eluting the sample matrix with 0·8 M HBr and collecting Pb in 7 M HCl. Sr was separated by a double pass through Eichrom Sr specific resin and collected in Milli-Q water. Isotopic ratios were measured by multi-collector (MC)-ICP-MS using a Nu-Plasma system at VUW, coupled to a desolvating nebulizer system (DSN-100). Pb isotope measurements were corrected for instrumental mass bias and drift by sample-standard bracketing using NBS-981. Two standard error (2 SE) internal precisions of $^{206}Pb/^{204}Pb$, $^{207}Pb/^{204}Pb$ and $^{208}Pb/^{204}Pb$ ratios were $<\pm 0{\cdot}0006$, $\pm 0{\cdot}0005$ and $\pm 0{\cdot}0013$, respectively. Pb isotope ratios are reported relative to $^{206}Pb/^{204}Pb = 16{\cdot}9416$, $^{207}Pb/^{204}Pb = 15{\cdot}5000$ and $^{208}Pb/^{204}Pb = 36{\cdot}7262$ for NBS-981 (Baker *et al.*, 2004). Repeat analyses of multiple digestions of the secondary standard JB-2 are within analytical error of the reference values from Baker *et al.* (2004). External reproducibility estimated from replicate digestions and analyses of JB-2 is 69 ppm for $^{206}Pb/^{204}Pb$, 143 ppm for $^{207}Pb/^{204}Pb$ and 197 ppm for $^{208}Pb/^{204}Pb$ (2 SD; $n = 5$). Sr isotope measurements were corrected by internal normalization to $^{86}Sr/^{88}Sr = 0{\cdot}1194$ and instrumental drift was corrected by sample-standard bracketing using SRM-987. Internal precisions (2 SE) of $^{87}Sr/^{86}Sr$ ratios were $<\pm 0{\cdot}000015$. Sr isotope ratios are reported relative to $^{87}Sr/^{86}Sr = 0{\cdot}710248$ for SRM-987. Analysis of the secondary standard BHVO-2 is within analytical error of the recommended reference values ($^{87}Sr/^{86}Sr = 0{\cdot}70347 \pm 4$: GEOREM database: www.georem.mpch-mainz.gwdg.de).

In situ mineral and glass major and trace element analysis

Mineral major element and glass analyses were undertaken on a JEOL JXA 8230 electron probe microanalyser (EPMA) at VUW using wavelength-dispersive spectrometry techniques. Calibrated international standards were analysed as unknowns to monitor instrumental drift and the precision and accuracy of the analyses. Approximate 2 SD analytical precisions calculated from repeated analysis of calibration standards are generally <5% for oxides that occur in concentrations >1 wt %. For lower concentration oxides, precision degrades with decreasing relative concentration.

Trace element analyses were measured *in situ* using a New Wave deep UV laser (193 nm solid state) coupled to the same Agilent ICP-MS system as used for solution whole-rock trace element analyses. The laser ablation (LA)-ICP-MS data acquisition technique used ^{43}Ca as the internal standard for secondary data normalization, which had previously been determined to ±5% by EPMA. Abundances of single trace elements were calculated relative to a bracketing standard (BCR-2G or NST 612), which was analysed under identical conditions throughout the analytical sessions. Using the same instrument and techniques, Allan *et al.* (2008) calculated approximate 2 SD analytical precisions of <10% and accuracies of <5% for most trace elements.

Stable oxygen isotope analysis

Pristine minerals previously analysed by EPMA and LA-ICP-MS were extracted from epoxy mounts and cleaned in sulphuric acid and Milli-Q to remove adhering epoxy. Oxygen was extracted from minerals for isotope analysis by laser fluorination (Sharp, 1990) with a 10·3 μm CO_2-laser and BrF_5 oxidation at GNS Science, Lower Hutt, New Zealand. Samples were evacuated for ~24 h and left overnight in a vapour of BrF_5. Blank BrF_5 analyses were performed until the oxygen yield was <2 μmol. Oxygen extracted from the samples was passed through a fluorine-getter before it was converted to CO_2 by a graphite furnace, yields were recorded, and the gas was analysed on a Geo20-20 mass spectrometer. All oxygen isotope values are reported in permil (‰) relative to Vienna Standard Mean Ocean Water (V-SMOW). Samples were normalized to international quartz standard NBS-28, using a value of +9·6‰. Values for four NBS-28 and UWG-2 standards analysed with the samples had values that varied by <0·15‰.

RESULTS

Sample characteristics and major element chemistry

Raoul volcano

Pumices from Raoul volcano are generally highly vesicular, and partially to wholly oxidized. Exceptions to this are the Green Lake floated pumice and Rangitahua eruption deposits, which comprise non-oxidized pumice clasts with a wide range of vesicularities (10–80 vol. % vesicles) (Barker *et al.*, 2012). Most clasts contain <3–5 vol. % crystals, dominantly plagioclase, with lesser clinopyroxene, orthopyroxene and magnetite. Trace amounts of olivine occur in the Matatirohia and Fleetwood samples, and trace amounts of quartz occur in the Oneraki, Green Lake and Rangitahua samples. In addition, sparse (<1–2 vol. %) sub-spherical, dark grey mafic inclusions (generally <5 mm, rarely 2–3 cm) are found in the Matatirohia, Oneraki and Fleetwood pumices (Fig. 3a and b). Rare <1 cm inclusions of white crystalline material are found in Oneraki, Green Lake and Rangitahua pumices (Fig. 3b).

The Raoul eruptions investigated in this study plot within the published fields of whole-rock major element data (Smith *et al.*, 2006, 2010), but are more tightly grouped for single eruptions, possibly because of our systematic removal of mafic inclusions. The data generally define linear trends, with Rangitahua samples being the least evolved (66–67 wt % SiO_2) and the Green Lake floated pumice the most evolved (69–70 wt % SiO_2) (Fig. 4a).

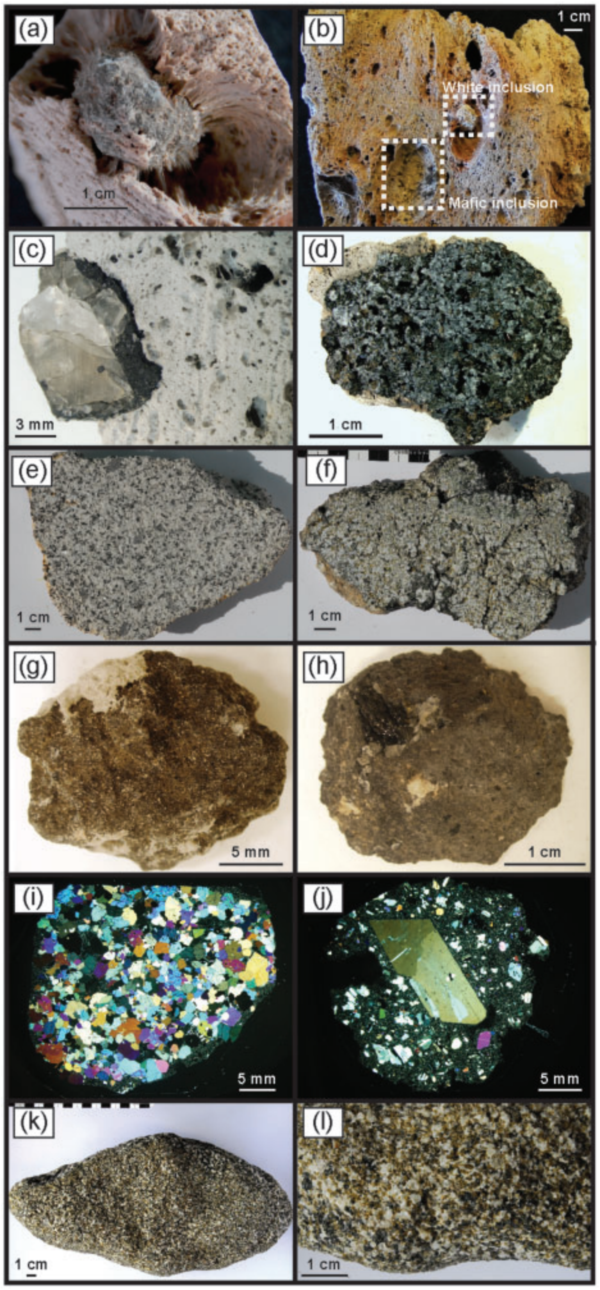

Fig. 3. Representative images of inclusions and xenolith types. (a) Mafic bleb within Matatirohia pumice (Raoul volcano) surrounded by large open vesicles. (b) White crystalline inclusion and small fragments of mafic material (outlined by white dotted boxes) within Oneraki pumice (Raoul volcano). (c) Large euhedral plagioclase within a mafic inclusion in pumice from Healy volcano. (d) Large crystalline mafic bleb with adhering pumice from Healy volcano. (e) Fragment of plutonic tonalite from the Matatirohia deposit. (f) Friable cumulate gabbroic xenolith from the Matatirohia deposit. (g) Exterior of a cauliform-textured mafic bleb with adhering white pumice from the Matatirohia deposit. (h) Exterior of a mafic bleb from the Matatirohia deposit with large crystals of clinopyroxene and plagioclase. (i) Thin section (crossed polarizers) of cauliform mafic bleb in (g) showing a crystalline granular texture and a thin adhering microcrystalline glass film. Phenocrysts are dominantly plagioclase and pyroxene, with lesser amounts of olivine and

Macauley volcano

Pumice clasts from the Sandy Bay Tephra are pale to mid-grey–brown and highly vesicular (Barker *et al.*, 2012), containing <2–3 vol. % crystals, dominated by larger (typically 0·5–1 mm) euhedral plagioclase and clinopyroxene, with smaller (<0·5 mm) orthopyroxene and Fe–Ti oxides. Large olivine crystals are also sparsely present (>0·5–1 mm), as well as sparse mafic inclusions that are generally small (<1–2 mm) but can reach up to 2 cm in diameter. Dredged pumice samples vary considerably in vesicularity and appearance when compared with the Sandy Bay Tephra pumices (see Barker *et al.*, 2012, for details). Dredged pumices are generally crystal poor (<1–3 vol. %), with crystal assemblages dominated by plagioclase and pyroxene, often represented by crystal clusters up to 2 mm in size. Large (generally <1–2 mm, but up to 2 cm), pale green clinopyroxenes were also noted in some pumices from dredge D33.

Whole-rock major element chemistry indicates that multiple silicic magma types have been erupted from Macauley volcano (Fig. 4b, Table 1; Barker *et al.*, 2012). Although prominent in the Macauley subaerial record, pumices with Sandy Bay pumice compositions form only a small proportion (four of 34 clasts analysed) of the total submarine compositional range (Barker *et al.*, 2012). Subaerial Sandy Bay Tephra pumices analysed in this study have compositions similar to those reported by Smith *et al.* (2003*a*), at ~70–71 wt % SiO_2. Macauley clasts with the most evolved compositions are lower vesicularity, crystal-poor blocky pumices and lava fragments dredged from the northern caldera rim. There are at least two other compositional groups within the submarine dredged pumices, with SiO_2 values ≤69 wt % (Fig. 4b). The first group shows notably higher TiO_2, and is composed mainly of pumice dredged from the southwestern caldera flank. A single clast analysed by Wright *et al.* (2006) from the Macauley cone (Fig. 2c) also plots within this chemical population. The second group shows lower TiO_2 and K_2O and is composed mainly of pumice from the northern caldera flank. Several of these pumice samples have distinctively high MgO contents corresponding to higher crystal contents (up to ~5 vol. %).

Healy volcano

Pumice recovered from Healy volcano displays a large variation in physical appearance ranging from white to dark grey in colour, often with banding (Wright &

Fig. 3 Continued
magnetite. (j) Thin section (crossed polarizers) of mafic bleb in (h) showing a single large plagioclase crystal and smaller crystals of olivine, pyroxene and plagioclase in a microcrystalline vesiculated groundmass. (k) Olivine-rich cumulate gabbro xenolith from the Sandy Bay Tephra. (l) Close-up of gabbroic xenolith from (k) showing crystalline granular texture with large high-An plagioclase, Mg-rich clinopyroxene and olivine.

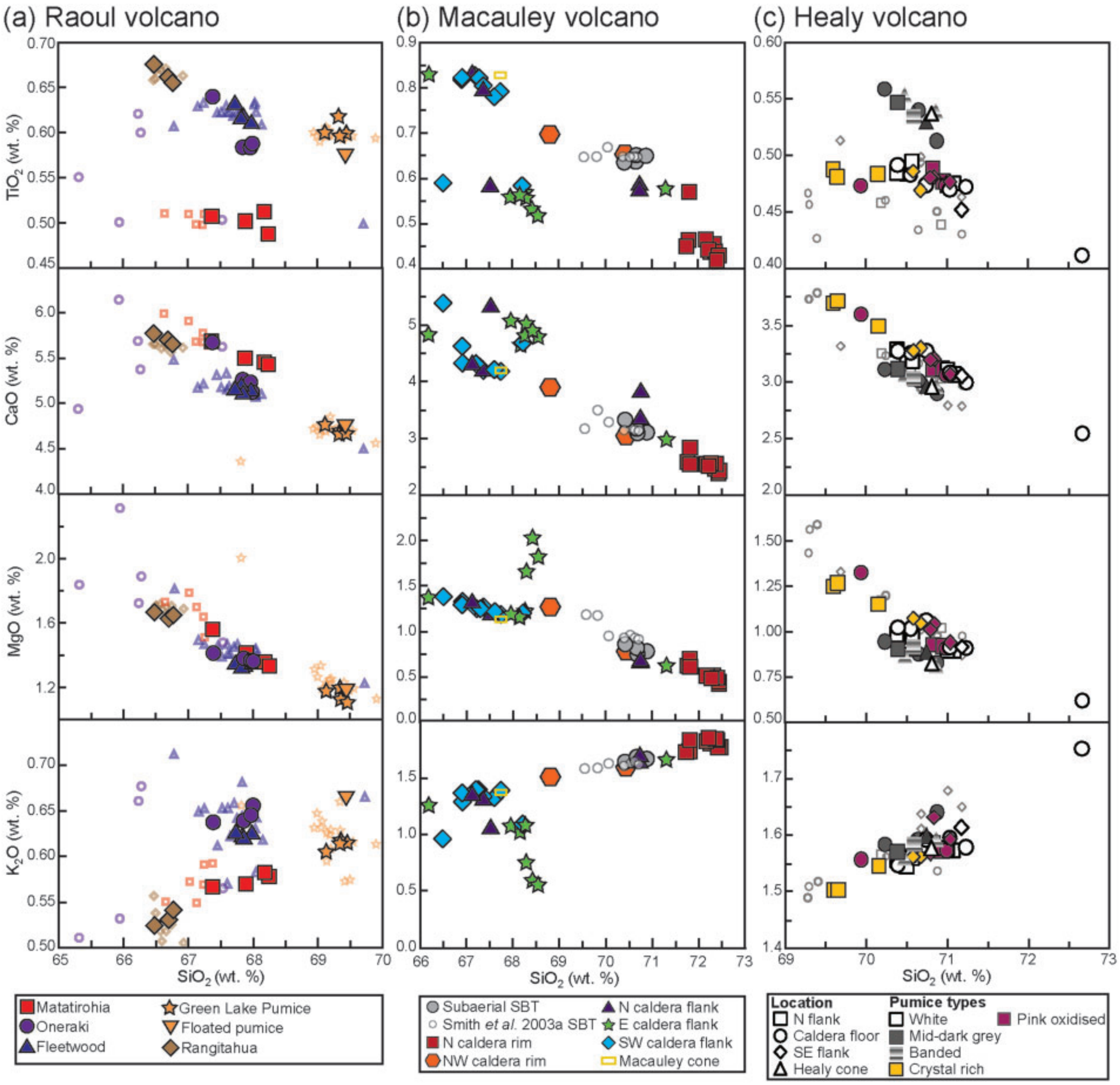

Fig. 4. Selected major element variation diagrams for pyroclasts from (a) Raoul volcano, (b) Macauley volcano, including subaerial deposits on Macauley Island (Sandy Bay Tephra: SBT) and dredge samples grouped by their relative location, and (c) Healy volcano with dredge samples grouped by their relative location and clast type. (See Fig. 2 for sample locations.) Large filled symbols are from this study; small open symbols are from Smith *et al.* (2006) for Raoul, Smith *et al.* (2003*a*) for Macauley SBT, Wright *et al.* (2006) for Macauley cone, and Wright & Gamble (1999) for Healy. All values have been normalized to 100%. (See Electronic Appendix C, Table C1 for raw data, original totals and LOI values.) Modified from Barker *et al.* (2012).

Gamble, 1999; Wright *et al.*, 2003; Barker *et al.*, 2012). Pumices in this study are mostly highly vesicular white- or grey-type pumices. In addition, multiple large fragments of lava were recovered from the central Healy edifice and caldera floor, of which two dark grey fragments from the caldera floor were analysed for comparison. Pumice crystal contents vary considerably, with most pumices having <3–5 vol. % crystals, but with several clasts containing up to 10–15 vol. % crystals. The crystal assemblage is dominated by <1–5 mm euhedral plagioclase, with lesser amounts of clinopyroxene, orthopyroxene, amphibole and minor amounts of quartz. Small (<0·1 mm) magnetite and ilmenite crystals are also common, often in higher concentrations in dark coloured or banded pumices. Large but generally sparse olivine crystals also occur in some pumices. Sparse dark grey mafic inclusions (averaging < 1–2 mm in size, but reaching up to 2–3 cm) are also present in many samples (Fig. 3c and d).

Although visibly diverse, there is little variation in the major element chemistry of the Healy pumices presented

Table 1: Representative major, trace element and isotopic compositions of Kermadec pumices and xenoliths

Sample:	RI03_P03	RI06_PC12	RI12_PC08	RI18_PC05	RI26_PC01	RI06_MB02	RI06_R01
Volcano:	Raoul	Raoul	Raoul	Raoul	Raoul	Raoul	Raoul
Type:	Pumice	Pumice	Pumice	Pumice	Pumice	Mafic bleb	Tonalite
Location:	Rangitahua	Matatirohia	Oneraki	GLP	Fleetwood	Matatirohia	Matatirohia
SiO_2	66·77	68·24	68·00	69·34	67·98	49·61	71·09
TiO_2	0·655	0·487	0·587	0·597	0·613	0·610	0·430
Al_2O_3	14·57	14·65	14·69	14·10	14·31	18·98	14·04
Fe_2O_3	6·30	5·48	5·41	5·27	5·90	11·34	4·57
MnO	0·184	0·159	0·162	0·163	0·158	0·190	0·100
MgO	1·650	1·333	1·361	1·133	1·359	5·460	1·110
CaO	5·65	5·43	5·12	4·71	5·16	12·34	4·14
Na_2O	3·55	3·53	3·86	3·93	3·74	1·58	4·20
K_2O	0·541	0·578	0·656	0·618	0·627	0·160	0·420
P_2O_5	0·137	0·113	0·156	0·147	0·153	0·050	0·060
LOI	1·21	1·14	1·86	1·40	1·60	−0·22	−0·02
Total	99·79	99·15	100·43	99·90	100·12	100·10	100·14
Sc	25·8	24·7	20·9	21·8	22·8	44·1	19·4
V	57·3	49·8	32·9	19·9	41·5	356·8	78·1
Cr	2·02	3·01	1·34	1·10	3·43	21·05	2·46
Ni	1·15	1·76	0·99	0·77	1·68	15·81	1·85
Cu	14·28	24·93	10·54	8·60	11·05	104·57	34·46
Zn	96·8	73·8	78·0	80·7	86·6	73·8	52·5
Ga	16·8	16·0	16·1	15·5	15·6	17·1	14·3
Rb	7·96	9·23	10·03	9·21	9·62	2·91	6·16
Sr	182	170	193	172	164	175	112
Y	37·8	36·3	37·4	39·6	38·6	13·1	40·8
Zr	65·0	66·1	75·1	70·9	71·6	23·3	n.d.
Nb	0·536	0·565	0·708	0·589	0·658	0·351	0·913
Mo	2·50	2·47	2·52	2·53	2·02	0·56	0·78
Cs	0·660	0·793	0·741	0·792	0·818	0·222	0·275
Ba	197	194	220	208	204	63	329
La	3·40	3·71	4·80	3·85	4·31	1·34	2·67
Ce	9·76	10·37	13·07	10·81	11·76	3·77	8·58
Pr	1·70	1·78	2·18	1·90	1·99	0·64	1·63
Nd	9·42	9·70	11·57	10·46	10·70	3·50	9·34
Sm	3·44	3·37	3·88	3·68	3·73	1·31	3·57
Eu	1·22	1·09	1·27	1·24	1·19	0·53	0·88
Gd	4·57	4·35	4·87	4·81	4·90	1·75	4·77
Tb	0·855	0·803	0·878	0·912	0·885	0·317	0·921
Dy	6·04	5·76	6·10	6·41	6·20	2·26	6·47
Ho	1·35	1·27	1·34	1·42	1·37	0·50	1·40
Er	4·02	3·90	4·10	4·32	4·13	1·49	4·15
Tm	0·612	0·597	0·613	0·660	0·620	0·225	0·615
Yb	4·14	4·05	4·17	4·52	4·19	1·51	4·06
Lu	0·629	0·612	0·630	0·680	0·639	0·227	0·582
Hf	2·21	2·21	2·49	2·45	2·39	0·97	n.d.
Ta	0·041	0·044	0·054	0·048	0·049	0·021	0·074

(continued)

Table 1: Continued

Sample:	RI03__P03	RI06__PC12	RI12__PC08	RI18__PC05	RI26__PC01	RI06__MB02	RI06__R01
Volcano:	Raoul	Raoul	Raoul	Raoul	Raoul	Raoul	Raoul
Type:	Pumice	Pumice	Pumice	Pumice	Pumice	Mafic bleb	Tonalite
Location:	Rangitahua	Matatirohia	Oneraki	GLP	Fleetwood	Matatirohia	Matatirohia
W	0·382	0·259	0·200	0·284	0·205	0·254	0·265
Pb	12·84	3·05	3·33	3·41	4·44	1·24	1·89
Th	0·447	0·493	0·684	0·510	0·580	0·531	0·492
U	0·204	0·209	0·267	0·223	0·231	0·068	n.d.
^{206}Pb/^{204}Pb	n.d.	n.d.	18·677	18·665	18·679	18·667	18·687
^{207}Pb/^{204}Pb	n.d.	n.d.	15·577	15·577	15·581	15·568	15·581
^{208}Pb/^{204}Pb	n.d.	n.d.	38·389	38·377	38·399	38·346	38·459
^{207}Pb/^{206}Pb	n.d.	n.d.	0·83403	0·83454	0·83416	0·83400	0·83380
^{208}Pb/^{206}Pb	n.d.	n.d.	2·05536	2·05614	2·05570	2·05421	2·05803
^{87}Sr/^{86}Sr	n.d.	0·703424	0·703355	0·703513	0·703494	0·703435	0·703816

Sample:	MI07__P03	D24__PC04	D25__PC01	D29__PC02	D33__PC02	D33__PC04	D38__PC06
Volcano:	Macauley	Macauley	Macauley	Macauley	Macauley	Macauley	Healy
Type:	Pumice	Pumice	Pumice	Pumice	Pumice	Pumice	Pumice
Location:	SBT	SW flank	SW flank	N rim	E flank	E flank	NW flank/rim
SiO_2	70·66	67·73	67·28	72·37	68·27	68·42	69·65
TiO_2	0·638	0·792	0·821	0·435	0·570	0·533	0·481
Al_2O_3	13·28	13·81	13·79	12·78	14·96	13·83	14·69
Fe_2O_3	4·99	6·16	6·41	4·62	4·83	5·22	3·72
MnO	0·141	0·168	0·172	0·124	0·135	0·175	0·117
MgO	0·816	1·193	1·241	0·488	1·206	2·033	1·265
CaO	3·16	4·18	4·25	2·53	4·79	4·91	3·72
Na_2O	4·51	4·34	4·40	4·75	4·02	4·13	4·74
K_2O	1·660	1·388	1·397	1·827	1·076	0·597	1·504
P_2O_5	0·125	0·235	0·251	0·076	0·144	0·157	0·106
LOI	2·44	0·54	0·55	1·11	0·65	0·62	1·48
Total	100·34	99·97	100·07	99·74	100·16	100·21	100·15
Sc	14·3	17·4	18·2	12·1	13·5	20·7	12·6
V	12·2	29·7	32·9	4·2	11·2	29·0	51·0
Cr	2·04	1·75	1·10	1·63	2·76	61·17	6·75
Ni	0·87	0·99	0·93	0·58	1·56	15·61	3·37
Cu	17·59	25·60	25·14	25·37	25·58	47·61	20·16
Zn	90·6	96·6	96·0	77·8	88·3	101·9	51·8
Ga	15·9	17·0	16·9	16·4	15·9	15·9	16·5
Rb	28·75	25·56	25·02	31·59	29·45	8·16	24·65
Sr	164	214	212	142	193	189	220
Y	46·1	47·0	46·7	49·4	47·0	40·1	38·8
Zr	150·6	149·4	147·8	178·9	154·8	89·3	162·5
Nb	1·713	1·877	1·858	2·125	1·738	0·883	2·996
Mo	2·20	1·81	1·85	2·17	2·32	1·93	1·65

(continued)

Table 1: Continued

Sample:	MI07_P03	D24_PC04	D25_PC01	D29_PC02	D33_PC02	D33_PC04	D38_PC06
Volcano:	Macauley	Macauley	Macauley	Macauley	Macauley	Macauley	Healy
Type:	Pumice	Pumice	Pumice	Pumice	Pumice	Pumice	Pumice
Location:	SBT	SW flank	SW flank	N rim	E flank	E flank	NW flank/rim
Cs	1·348	1·017	1·008	1·268	1·428	0·732	0·732
Ba	414	362	358	466	433	202	788
La	11·00	11·84	11·66	12·96	11·55	4·12	13·04
Ce	27·93	30·28	29·97	32·67	28·34	12·30	29·97
Pr	4·24	4·62	4·60	4·91	4·37	2·13	4·27
Nd	20·21	22·58	22·49	23·09	20·74	11·50	18·93
Sm	5·70	6·25	6·20	6·39	5·85	3·97	4·91
Eu	1·50	1·75	1·76	1·53	1·51	1·35	1·44
Gd	6·47	6·92	6·89	7·08	6·50	5·07	5·43
Tb	1·093	1·157	1·155	1·198	1·121	0·919	0·926
Dy	7·35	7·65	7·69	8·10	7·56	6·46	6·16
Ho	1·60	1·65	1·65	1·76	1·65	1·42	1·32
Er	4·85	4·95	4·90	5·28	5·04	4·23	4·08
Tm	0·729	0·745	0·751	0·809	0·768	0·633	0·634
Yb	4·96	5·02	4·96	5·47	5·18	4·36	4·32
Lu	0·754	0·761	0·751	0·837	0·778	0·645	0·659
Hf	4·43	4·34	4·33	5·24	4·55	2·72	4·34
Ta	0·109	0·118	0·117	0·134	0·111	0·068	0·198
W	0·313	0·240	0·448	0·264	0·389	0·247	0·253
Pb	7·64	5·80	5·57	6·80	8·24	4·71	3·81
Th	1·747	1·888	1·800	2·278	1·840	0·389	2·352
U	0·665	0·726	0·711	0·854	0·710	0·241	0·692
^{206}Pb/^{204}Pb	18·710	18·711	18·716	18·708	n.d.	18·663	18·824
^{207}Pb/^{204}Pb	15·582	15·585	15·590	15·586	n.d.	15·585	15·601
^{208}Pb/^{204}Pb	38·441	38·447	38·465	38·445	n.d.	38·398	38·607
^{207}Pb/^{206}Pb	0·83282	0·83291	0·83297	0·83307	n.d.	0·83506	0·82882
^{208}Pb/^{206}Pb	2·05455	2·05473	2·05513	2·05485	n.d.	2·05742	2·05095
^{87}Sr/^{86}Sr	0·703495	n.d.	0·703531	0·703507	n.d.	0·703368	0·703844

Sample:	D39_PC05	D44_PC02	D47_PC02	D44_MB03	D22_PC02	D23_PC02	D22_03 MB01
Volcano:	Healy	Healy	Healy	Healy	Raoul SW	Raoul SW	Raoul SW
Type:	Pumice	Pumice	Pumice	Mafic bleb	Pumice	Pumice	Mafic bleb
Location:	N rim/wall	SE flank/rim	Edificecrater	SE flank/rim	NE rim/wall	SW floor/wall	NE rim/wall
SiO$_2$	72·67	71·18	70·74	53·03	74·12	74·16	58·63
TiO$_2$	0·411	0·452	0·529	0·923	0·395	0·399	0·577
Al$_2$O$_3$	14·01	14·31	14·55	16·88	13·70	13·69	16·41
Fe$_2$O$_3$	2·81	3·31	3·39	11·24	2·60	2·58	8·33
MnO	0·112	0·114	0·135	0·198	0·119	0·121	0·179
MgO	0·618	0·914	0·886	4·623	0·646	0·699	4·331
CaO	2·54	3·05	2·97	9·68	3·64	3·62	8·98

(continued)

Table 1: Continued

Sample:	D39__PC05	D44__PC02	D47__PC02	D44__MB03	D22__PC02	D23__PC02	D22__03 MB01
Volcano:	Healy	Healy	Healy	Healy	Raoul SW	Raoul SW	Raoul SW
Type:	Pumice	Pumice	Pumice	Mafic bleb	Pumice	Pumice	Mafic bleb
Location:	N rim/wall	SE flank/rim	Edificecrater	SE flank/rim	NE rim/wall	SW floor/wall	NE rim/wall
Na_2O	5·00	4·95	5·09	2·88	4·02	3·97	2·26
K_2O	1·754	1·614	1·599	0·427	0·668	0·671	0·219
P_2O_5	0·074	0·099	0·113	0·119	0·090	0·095	0·080
LOI	1·11	1·68	0·85	−0·75	2·99	3·48	−0·34
Total	99·70	99·86	99·27	100·06	99·97	101·71	100·10
Sc	8·3	10·3	10·4	35·3	17·1	16·7	36·8
V	14·1	36·6	16·3	344·0	13·3	12·7	240·1
Cr	2·20	3·08	1·78	15·76	1·62	0·90	28·65
Ni	0·61	1·41	0·69	11·73	0·89	1·41	12·04
Cu	7·39	14·84	7·04	139·03	6·37	8·27	48·21
Zn	60·8	54·6	68·6	79·6	72·3	77·5	78·1
Ga	15·8	15·9	16·3	17·3	14·8	14·7	15·3
Rb	29·62	26·03	26·18	7·01	10·22	10·39	3·77
Sr	203	200	247	290	167	169	139
Y	41·7	39·6	40·2	22·4	38·9	38·6	19·8
Zr	178·9	168·8	162·8	52·2	81·9	82·9	31·0
Nb	3·396	3·088	2·983	1·098	0·708	0·725	0·464
Mo	1·09	1·38	1·35	1·12	1·87	1·86	0·82
Cs	0·754	0·760	0·716	0·274	0·838	0·841	0·419
Ba	915	811	833	300	225	231	88
La	14·17	13·62	13·75	4·35	5·08	5·11	1·87
Ce	32·34	30·92	32·06	10·75	13·49	13·59	5·12
Pr	4·52	4·41	4·49	1·72	2·19	2·21	0·85
Nd	20·26	19·63	20·13	8·74	11·27	11·46	4·74
Sm	5·16	5·07	5·17	2·66	3·73	3·75	1·67
Eu	1·47	1·41	1·56	1·03	1·20	1·20	0·66
Gd	5·58	5·64	5·70	3·19	4·70	4·86	2·36
Tb	0·968	0·947	0·961	0·559	0·857	0·878	0·445
Dy	6·45	6·35	6·37	3·80	6·06	6·17	3·21
Ho	1·40	1·37	1·37	0·81	1·34	1·37	0·72
Er	4·24	4·21	4·15	2·39	4·06	4·14	2·17
Tm	0·661	0·649	0·637	0·347	0·639	0·634	0·330
Yb	4·67	4·48	4·40	2·31	4·26	4·37	2·26
Lu	0·723	0·691	0·661	0·348	0·659	0·665	0·359
Hf	4·69	4·50	4·24	1·50	2·59	2·64	1·07
Ta	0·264	0·205	0·196	0·067	0·052	0·054	0·026
W	0·506	0·270	0·246	0·385	0·244	0·261	0·334
Pb	4·73	4·39	4·43	1·91	3·68	3·72	1·43
Th	2·711	2·434	2·429	0·638	0·697	0·722	0·250
U	0·805	0·731	0·722	0·175	0·277	0·294	0·097
$^{206}Pb/^{204}Pb$	18·824	18·820	18·826	n.d.	18·705	18·699	18·714

(continued)

Table 1: Continued

Sample:	D39__PC05	D44__PC02	D47__PC02	D44__MB03	D22__PC02	D23__PC02	D22__03 MB01
Volcano:	Healy	Healy	Healy	Healy	Raoul SW	Raoul SW	Raoul SW
Type:	Pumice	Pumice	Pumice	Mafic bleb	Pumice	Pumice	Mafic bleb
Location:	N rim/wall	SE flank/rim	Edificecrater	SE flank/rim	NE rim/wall	SW floor/wall	NE rim/wall
$^{207}Pb/^{204}Pb$	15·601	15·595	15·603	n.d.	15·582	15·583	15·590
$^{208}Pb/^{204}Pb$	38·607	38·592	38·613	n.d.	38·430	38·430	38·472
$^{207}Pb/^{206}Pb$	0·82879	0·82868	0·82876	n.d.	0·83305	0·83335	0·83309
$^{208}Pb/^{206}Pb$	2·05093	2·05056	2·05099	n.d.	2·05462	2·05514	2·05584
$^{87}Sr/^{86}Sr$	n.d.	0·703860	0·703810	n.d.	n.d.	0·703555	n.d.

Oxide abundances given in wt % and normalized to 100% on a volatile-free basis, with original LOI values and analytical totals given. LOI is weight loss on ignition at 1000°C for ~1 h. n.d., not determined. Trace elements given in ppm. Isotope ratios calculated relative to bracketing standard NBS-981 for Pb and SRM-987 for Sr. GLP, Green Lake Pumice; SBT, Sandy Bay Tephra (see Electronic Appendix A for sample details).

in this study and that of Wright & Gamble (1999) (Fig. 4c, Table 1). There are no strong correlations between clast physical appearance and major element chemistry with dredge location. All samples follow linear trends on major element variation diagrams, with SiO_2 between ~69·5 and 71·5 wt %. Most variations can be linked to crystal contents, with the lowest SiO_2 clasts being the most crystal rich. A single outlying clast with >72·5 wt % SiO_2 has unusually low crystal content (<1–2 wt %). Dark grey pumices and lava fragments have slightly higher TiO_2 than the white pumices, reflecting a higher abundance of Fe–Ti oxides.

Raoul SW volcano

Dredge sampling at Raoul SW recovered crystal-poor (1–3 vol. %), highly vesicular, white to slightly oxidized pumice (Barker *et al.*, 2012). The mineral assemblage is dominated by 1–5 mm euhedral plagioclase and clinopyroxene, with smaller (<0·5–1 mm) orthopyroxene and Fe–Ti oxides. Sparse quartz and amphibole are also present with trace amounts of <5 mm olivine crystals. Dark grey mafic inclusions <2–3 cm in size are also present within pumices. There is little variation in the major element chemistry of the Raoul SW pumice, which defines a narrow compositional range between ~73·5 and 75 wt % SiO_2, and strong linear correlations on variation diagrams (Fig. 5).

Xenoliths and inclusions

Previous studies have interpreted plutonic beach boulders on the northern coast of Raoul Island (Brothers & Searle, 1970; Lloyd & Nathan, 1981; Worthington, 1998) as xenoliths derived from the young pyroclastic units. In this study we analysed xenoliths occurring as plutonic beach boulders, as single clasts within the Matatirohia deposit and as inclusions within pumices. Our results show three lithological types that closely match those previously described in the beach rubble, as follows.

(1) Tonalites (Fig. 3e) composed dominantly of interlocking euhedral to subhedral plagioclase and quartz with lesser amounts of hornblende and variable amounts of hydrothermal alteration minerals and/or overgrowths of actinolite (after hornblende) and epidote (after plagioclase). Small crystals (<1 mm) of spinel and ilmenite are also present, with trace amounts of zircon.

(2) Cumulate gabbros (Fig. 3f), which have large (average 1–2 mm, maximum ~1 cm) crystals of olivine, clinopyroxene and plagioclase, interspersed with small irregular patches of dark grey, partially vesicular, microlite-rich glass. A thin layer of solidified melt pervades the gabbro, causing parts of the rock to be friable.

(3) Cauliform, variably crystalline blebs of mafic material that occur as sparse single lapilli and as inclusions inside pumices (Fig. 3a, g and h; Lloyd & Nathan, 1981; Worthington, 1998). Many mafic blebs have adhering pumice glass, suggesting that they are a juvenile component (not accidental lithic fragments) (e.g. Fig. 3g and h). A spectrum of textures is observed in the mafic blebs, from holocrystalline blebs (similar to the cumulate gabbros) with only a thin surrounding film of dark grey melt (Fig. 3i), to melt-dominated blebs with scattered olivine, plagioclase and clinopyroxene in a poorly vesiculated microlite-rich glassy groundmass (Fig. 3j).

Large, melt-dominant mafic blebs collected loose from the Matatirohia fall deposit and extracted from Healy and Raoul SW pumices were analysed for their major element chemistry. Matatirohia mafic blebs are basaltic (Table 1)

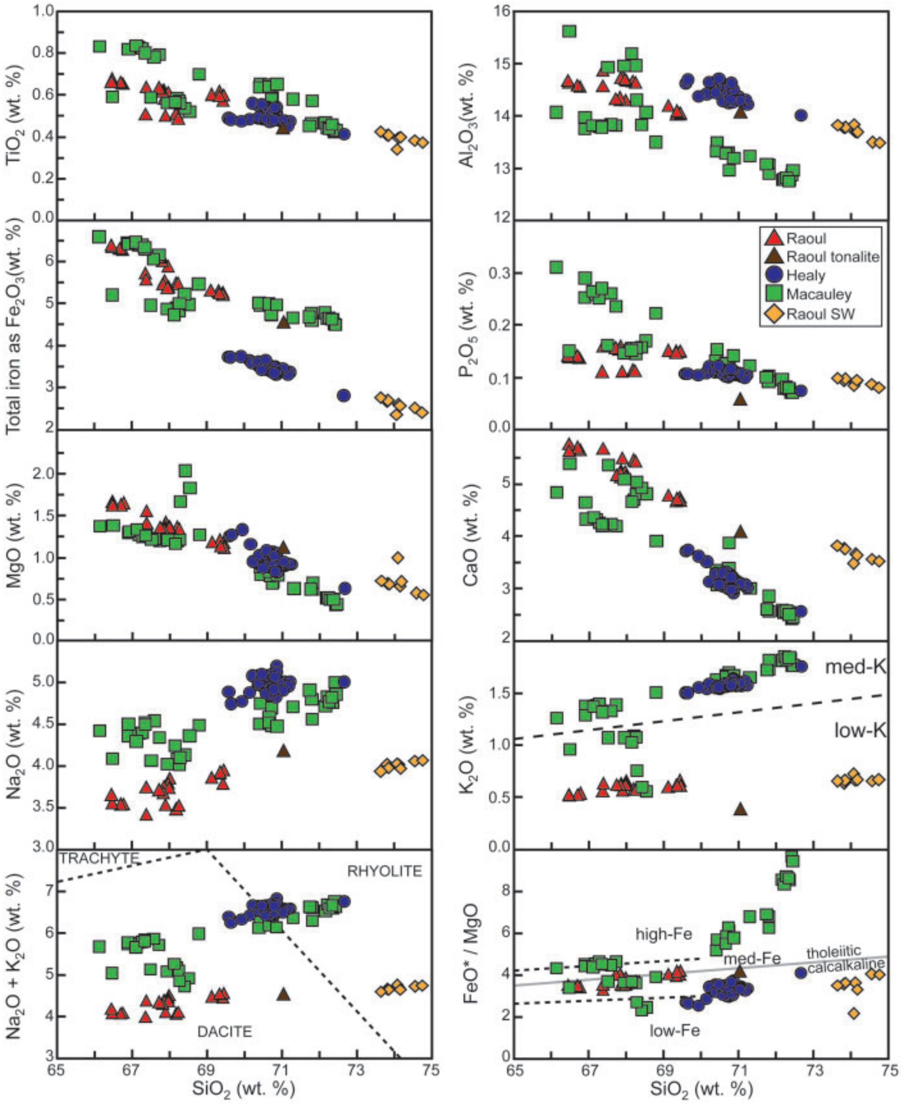

Fig. 5. Summary variation diagrams. Low- and medium-K discriminant boundary (from Gill, 1981) is marked by a dashed line on K_2O vs SiO_2 diagram. Compositional boundaries on total alkali ($Na_2O + K_2O$) vs SiO_2 (TAS) diagram are from Le Maitre (1989). Low-, medium- and high-Fe boundaries are marked by dashed lines on FeO*/MgO vs SiO_2 diagram, from Arculus (2003). The continuous grey line marks the discriminant boundary between tholeiitic and calc-alkaline suites (Miyashiro, 1974). All values have been recalculated based on oxide totals normalized to 100%. (See Electronic Appendix C, Table C1 for raw data, original totals and LOI values.) Modified from Barker *et al.* (2012).

and (similar to the dacites) have relatively low K_2O and TiO_2. The single Healy mafic bleb analysed is basaltic-andesite and similar in major element chemistry to the basalt reported by Wright & Gamble (1999). Consistent with the major element trends in the silicic samples, the Healy mafic bleb has higher total alkali contents than the Raoul blebs. The single Raoul SW mafic bleb analysed is andesitic, although intermingled rhyolite pumice glass could not completely be removed prior to analysis. In addition, a single tonalite xenolith analysed from the Matatirohia deposit (Table 1) is slightly more evolved than the Raoul dacites (~71 wt % SiO_2; Fig. 5), lying along the same trends but with notably lower K_2O and P_2O_5. Rare plutonic xenoliths have also been reported in the Sandy Bay Tephra on Macauley Island (Lloyd *et al.*, 1996; Smith *et al.*, 2003*a*). A single olivine-rich cumulate gabbro was collected as a xenolith from the Sandy Bay Tephra for crystal-specific analyses; this contains large (typically 1–5 mm, but up to 1–2 cm) euhedral plagioclase, clinopyroxene and olivine, with smaller (<0·5 mm) magnetite (Fig. 3k and l).

Whole-rock trace element variations

A subset of 46 samples was analysed for trace elements by solution ICP-MS. All samples have high concentrations of fluid-mobile large ion lithophile elements (LILE: Cs, Rb, Ba, U, K, Pb, Sr) and relatively low concentrations of fluid-immobile high field strength elements (HFSE: Ti, Zr, Hf, Nb, Ta) with respect to mid-ocean ridge basalts (MORB), typical for arc magmas (Pearce & Peate, 1995; Fig. 6). Raoul pumices show only small variations between eruptions, with all samples being slightly light rare earth element (LREE) depleted (Fig. 6a, Table 1) with $Eu/Eu^* = 0{\cdot}85$–$0{\cdot}94$ coupled with large negative Ti anomalies. The Matatirohia tonalite shows similar trace element patterns to the pumices but with $Eu/Eu^* = 0{\cdot}65$, indicating extensive plagioclase crystallization. The two Matatirohia mafic blebs have trace element concentrations that are considerably lower than those of the silicic magmas, but strongly parallel in their trace element patterns (Fig. 6a). Mafic blebs have $Eu/Eu^* = 1{\cdot}08$–$1{\cdot}11$ and no Ti anomalies, precluding plagioclase or magnetite fractionation. Similar patterns of trace element concentrations occur between pumices and the single mafic bleb from Raoul SW (Fig. 6b), which are also slightly LREE-depleted. In contrast, the majority of Macauley pumices are LREE-enriched (Fig. 6c, Table 1). Pumices from the caldera rim have the highest incompatible trace element concentration and the most pronounced $Eu/Eu^* = 0{\cdot}69$–$0{\cdot}73$ and negative Ti anomalies. The three samples that have low K and low Fe have similar trace element patterns to other Macauley pumices, although at lower concentrations and with $Eu/Eu^* = 0{\cdot}86$–$0{\cdot}92$. Notably, one Macauley pumice (D33.PC04) is LREE-depleted with similar trace element patterns to samples from Raoul and Raoul SW. Two basaltic samples from pre-Sandy Bay lavas, and a single Sandy Bay basaltic lithic fragment analysed by Smith *et al.* (2003*a*) have trace element patterns that are strongly parallel to those of the Sandy Bay pumices (Fig. 6c). Healy pumices are also LREE-enriched, with $Eu/Eu^* = 0{\cdot}78$–$0{\cdot}87$ and large negative Ti anomalies, but have distinctively higher Ba (Fig. 6d). Healy basalts have trace element patterns that generally are parallel to those of silicic pumices, but with $Eu/Eu^* = 1{\cdot}08$ and slightly higher Sr concentrations.

Whole-rock Pb and Sr isotopic compositions

Pb and Sr isotopic compositions are relatively uniform for each volcano, but differ significantly between volcanoes (Fig. 7, Table 1). Healy samples are the most radiogenic, having high $^{207}Pb/^{204}Pb$ and $^{208}Pb/^{204}Pb$ and also high $^{87}Sr/^{86}Sr$ ratios ($>0{\cdot}7038$), similar to other southern Kermadec volcanoes, which trend towards the Kermadec sediment field (Gamble *et al.*, 1996; Turner *et al.*, 1997; Ewart *et al.*, 1998; Haase *et al.*, 2002). Raoul, Macauley, and Raoul SW samples typically show only slight differences between volcanoes and rock types. Raoul basalts and dacites have similar isotopic compositions; however, Raoul tonalites have markedly higher $^{87}Sr/^{86}Sr$, resulting from hydrothermal alteration involving seawater (Fig. 7c). Pumices from Macauley and Raoul SW have isotopic compositions more similar to fluid from altered MORB and sedimentary Pb, according to Haase *et al.* (2002) (Fig. 7).

Mineral major and trace element chemistry

There are significant differences in crystal varieties, sizes, and compositional zoning between pumices from the four Kermadec volcanoes studied. In all samples, crystals tend to have three types of association: (1) single crystals with adhering felsic glass (Fig. 8a–e); (2) crystal clusters (<5 mm in size) dominated by pyroxene and plagioclase (Fig. 8f); or (3) single or multiple crystals sheathed by microlite-rich, poorly vesiculated glass, forming round blebs up to 2 cm (Figs 3a and 8g). Below we describe each crystal phase, focusing on their type of association, compositional range and zonation patterns between volcanoes.

Plagioclase

Plagioclase is the most abundant crystal phase and occurs in all three of the associations listed above. Plagioclase tends to be >0·5 mm and shows a wide range of textures and zonation patterns in backscattered electron (BSE) images (Fig. 8a), corresponding to a wide range of compositions (Fig. 9). Two dominant populations are identified in this study: (1) high-An (typically $>An_{80}$; Fig. 9), which can be unzoned or display strong compositional zoning with resorbed high-An cores and lower-An rims and/or overgrowths (Fig. 8a), occurring dominantly as large single crystals or in mafic blebs (Fig. 8g); (2) low-An (typically An_{40} to An_{70}; Fig. 9), which commonly shows both normal and reverse compositional zoning with some crystals displaying complex zoning (including sieve textures, resorbed cores and oscillatory zoning; Fig. 8a), typically occurring in crystal clusters (Fig. 8f) or as small single or groundmass crystals.

Plagioclase compositions vary between volcanoes, largely depending on the presence or relative proportions of the two plagioclase populations (Fig. 9). Raoul pumices contain dominantly high-An plagioclase, with two dominant high-An sub-modes (Fig. 9a), the most calcic of which (peak 1 a in Fig. 9a) is similar to crystals from the gabbroic xenolith (Fig. 9b). Raoul pumices also contain a tail of low-An plagioclase, dominantly as rims on high-An plagioclase and small groundmass crystals (peak 2 in Fig. 9a). A third outlier population (An_{56} to An_{20}) in the Oneraki and Green Lake samples (peak 3 in Fig. 9a) typically occurs as >1 mm normally zoned mottled and cracked, subhedral to anhedral crystals (Fig. 8a). These crystals are markedly similar to plagioclase from the tonalite xenolith (Fig. 9b). Plagioclase crystals from Raoul SW pumices are also dominantly high-An, with two high-An sub-modes similar to those at Raoul, but with fewer low-An plagioclase crystals (Fig. 9c). In contrast, plagioclase crystals

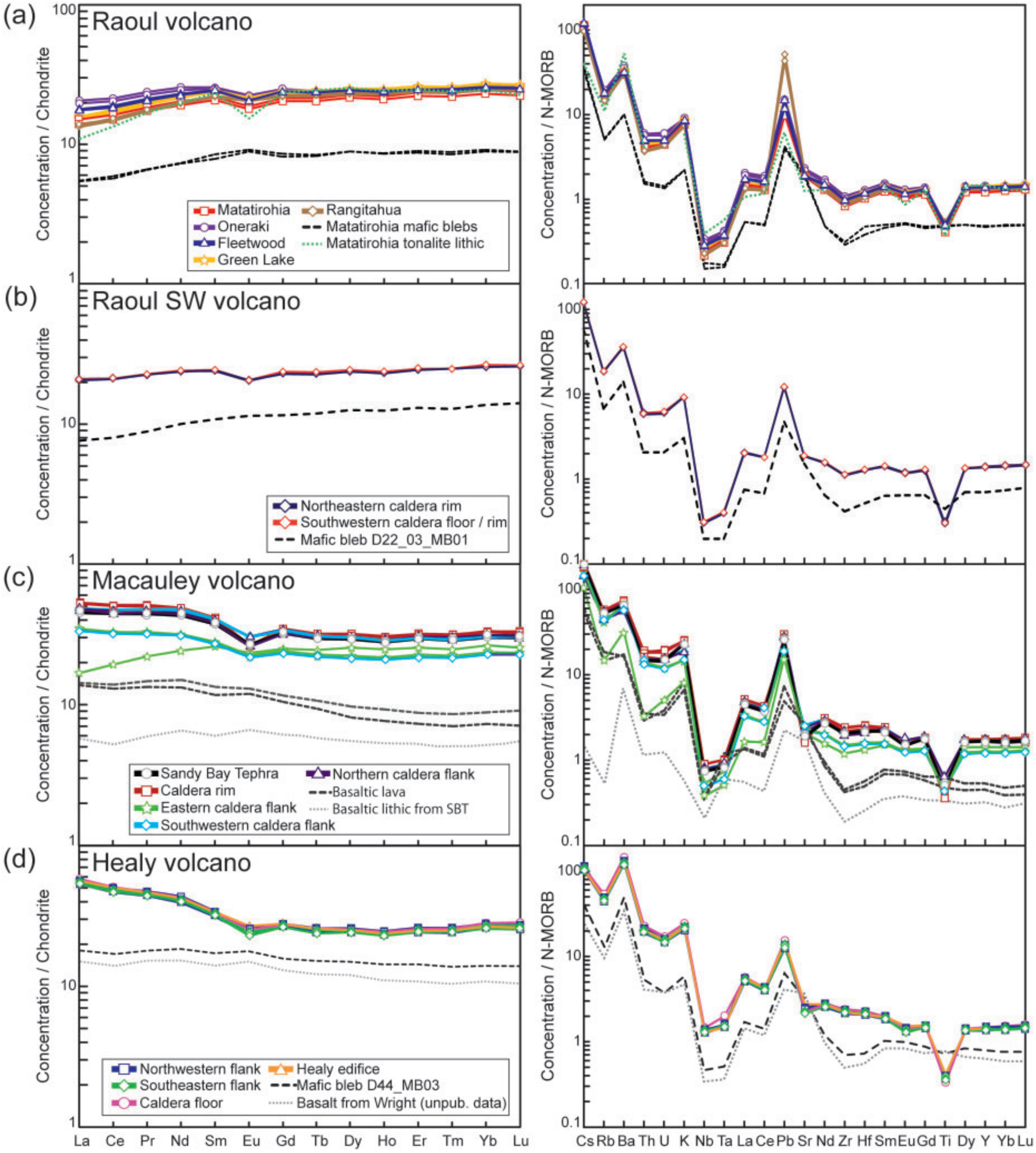

Fig. 6. REE diagrams normalized to chondrite (Palme & Beer, 1993), and multi-element diagrams normalized to normal-mid-ocean ridge basalt (N-MORB) values of Sun & McDonough (1989). (a) Raoul dacite pumices, Matatirohia mafic blebs and tonalite xenolith. It should be noted that U, Zr and Hf are not shown for the tonalite sample owing to the presence of zircon. The Rangitahua samples have anomalously high Pb concentrations, interpreted as hydrothermal clay contamination. (b) Samples from Raoul SW volcano, including a single mafic bleb. (c) Macauley pumice from this study compared with basaltic lavas and a Sandy Bay Tephra basaltic lithic fragment from Smith *et al.* (2003*a*). (d) Healy pumice and a single mafic bleb from this study and basaltic lava from I. C. Wright (unpublished data). (See Electronic Appendix C, Table C2 for raw data.)

from Macauley and Healy are dominantly low-An, show minor variations between crystal cores and rims (Fig. 9d–f) and often display complex oscillatory zoning (e.g. Fig. 8a). High-An (>An_{88}) plagioclase occurs sparsely as >1 mm crystals at Macauley with compositions similar to those of cores and unzoned crystals from the Sandy Bay gabbro xenolith (Fig. 9e). Healy pumices also contain a small population of large high-An plagioclase (>An_{88}), with

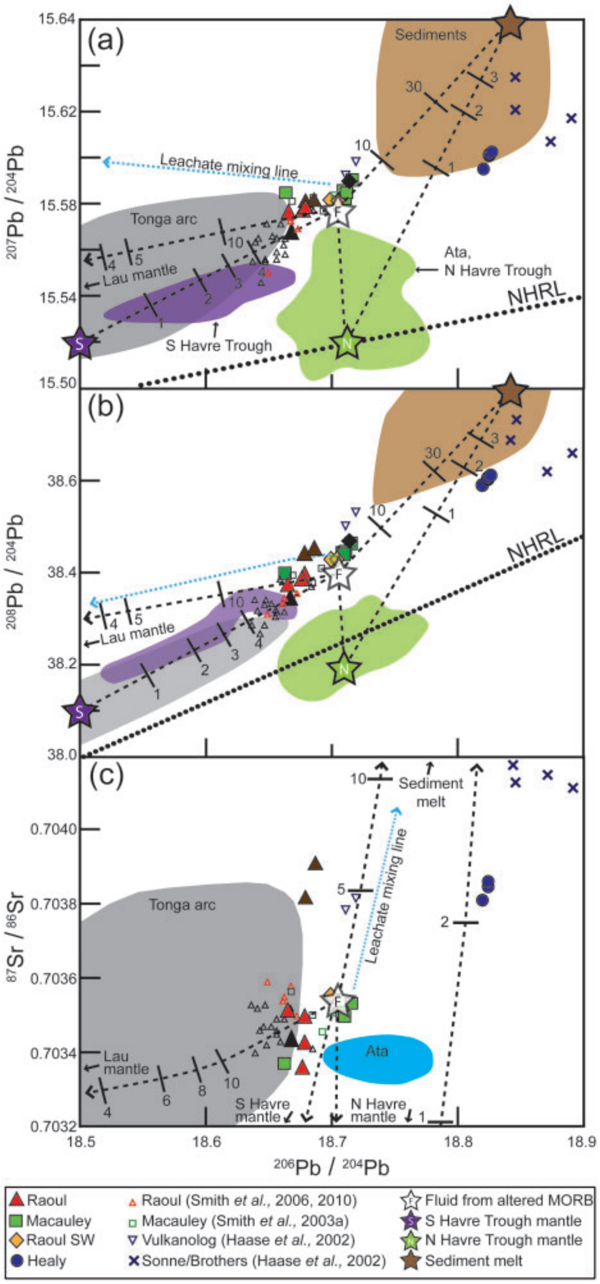

Fig. 7. Whole-rock isotopic compositions for selected samples from the Kermadec volcanoes investigated in this study compared with previous studies (cited in key). Dashed black lines connect end-member compositions for mantle and sediment components (shaded stars) from Haase *et al.* (2002) and with fluid from altered MORB (white star). Ticks on dashed lines mark the per cent mixing between the two end members [mixing calculations from Haase *et al.* (2002)]. Dotted line marks the leachate compositions for a single sample (see Electronic Appendix B). Shaded compositional fields represent published data from the Tonga–Kermadec region (Ewart & Hawkesworth, 1987; Loock *et al.*, 1990; Pearce *et al.*, 1995; Gamble *et al.*, 1996, 1997; Regelous *et al.*, 1997; Turner *et al.*, 1997; Bach *et al.*, 1998; Ewart *et al.*, 1998; Peate *et al.*, 2001; Haase *et al.*, 2002). Northern Hemisphere Reference Line (NHRL) from Hart (1984). Figure modified from Haase *et al.* (2002). (See Electronic Appendix C, Table C3 for raw data.)

subordinate outliers between An_{60} and An_{80}, representing cores of strongly zoned large crystal clusters (Fig. 8f), which are overgrown by low-An rims (Fig. 9f).

Most plagioclase trace element concentrations from Raoul, Macauley, and Healy (Fig. 10) increase with decreasing An values (i.e. changing melt compositions and consequent variations in trace element partitioning; Blundy & Wood, 1991). The exception is Sr, which begins to decrease at $< An_{50-60}$ (Fig. 10a). Eu and Ba concentrations show a slight increasing trend for An_{98} to An_{60} followed by a sharp increase at $< An_{60}$ for Macauley and Healy pumices (Fig. 10b and c).

Clinopyroxene

Clinopyroxene is the second most common mineral phase and also occurs as two compositional groups (Fig. 11): (1) Mg-rich crystals [with core compositions of $Mg\# > 70$, where $Mg\# = 100Mg/(Mg + Fe_{total} + Mn)$], which are euhedral and range from unzoned to strongly zoned, typically found as isolated > 0·5 mm crystals with adhering felsic glass (Fig. 8b), or as < 2 cm crystals inside mafic blebs (Fig. 8g); (2) Fe-rich crystals ($Mg\# < 70$), which are subhedral and lack strong compositional zonation, typically occurring as < 0·5 mm long single crystals (Fig. 8b), or clustered with low-An plagioclase and orthopyroxene (Fig. 8f).

Clinopyroxene compositional relationships are complex and variable (Fig. 11). At Raoul, many Mg-rich clinopyroxenes cores show strongly zoned rims that are similar in composition to unzoned Fe-rich clinopyroxenes (Fig. 11a). Rim thicknesses vary from absent to 10–20 μm in the Matatirohia and Fleetwood, 30–50 μm in the Oneraki and up to 100 μm in the Green Lake pumices. The Oneraki and Green Lake pumices also contain a higher proportion of Fe-rich clinopyroxene. Some strongly zoned Mg-rich clinopyroxenes also display resorbed cores (e.g. Fig. 8b and g), overgrown by an even more Mg- and Ca-rich band. Mg-rich clinopyroxenes from the Raoul pumices overlap in composition with those from the mafic bleb and gabbroic xenolith (Fig. 11b). Similar compositional trends are observed in pumices from Raoul SW (Fig. 11c). At Macauley, however, there is a broader spread of clinopyroxene types and compositions (Fig. 11d). All but the most evolved sample (D29_PC02) contain Mg-rich clinopyroxene cores, which overlap in composition with those from the gabbro xenolith, and rims that overlap with Fe-rich unzoned clinopyroxene compositions. In contrast, Healy clinopyroxenes show only minor variations in composition (Fig. 11e), but have a range of crystal sizes and zonations indicative of multiple populations. Samples D38_PC06 and D44_PC02 contain dominantly > 5 mm euhedral clinopyroxene, both as single crystals and within mafic blebs (Fig. 8g), often with thin higher-Fe rims (Fig. 11e). In contrast, samples D39_PC05 and D47_PC02

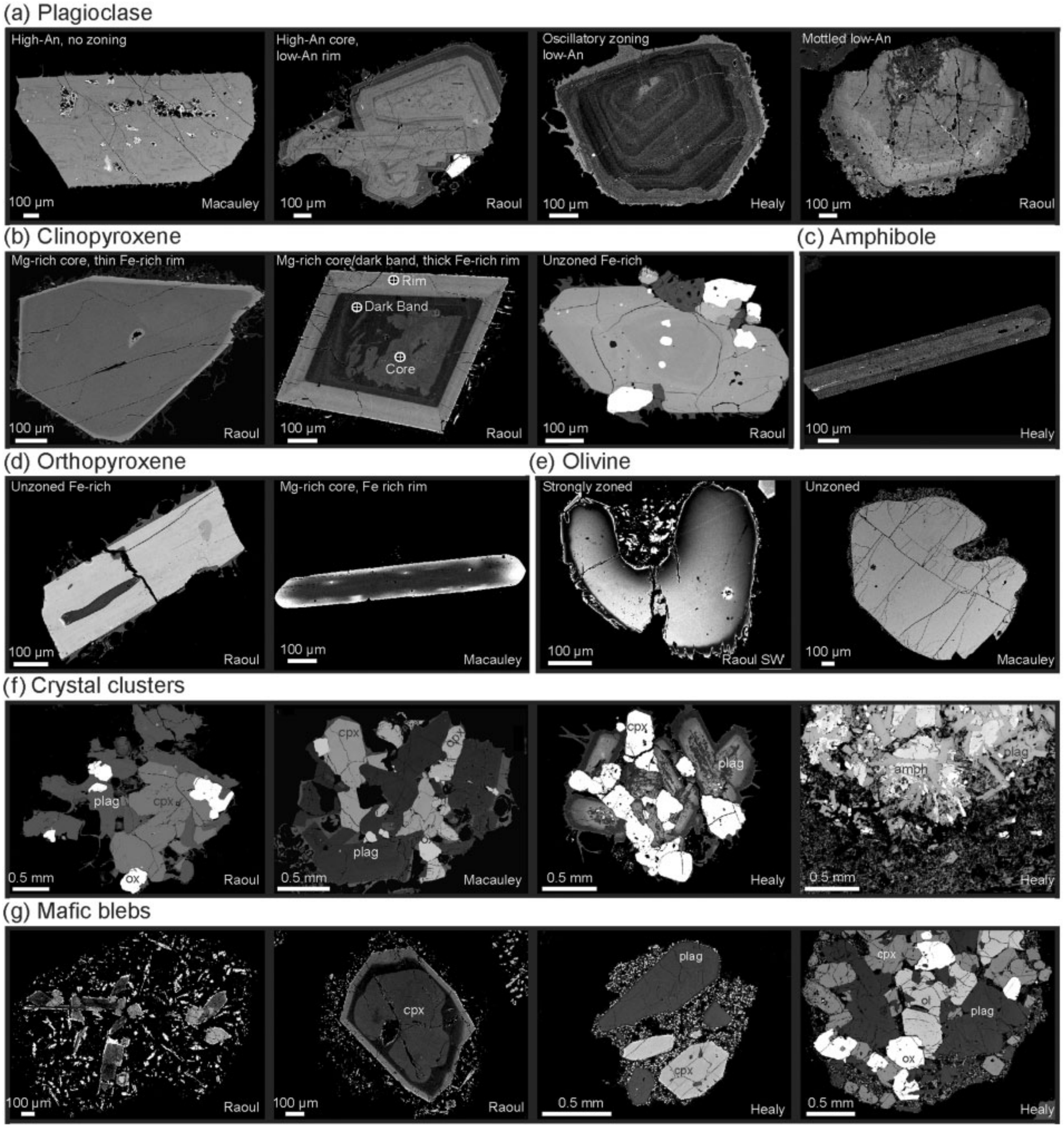

Fig. 8. Back-scattered electron images of representative crystal types found in pumices from the Kermadec volcanoes. (a) Representative end-member plagioclase types, including high-An, low-An and mottled 'tonalite-type' plagioclase. (b) Representative clinopyroxene types including both weakly zoned and strongly zoned Mg-rich clinopyroxene with dark coloured high-Mg resorbed core, and unzoned Fe-type clinopyroxene with inclusions of apatite and magnetite. (c) Weakly zoned amphibole. (d) Representative orthopyroxene types including both Fe-rich and Mg-rich types. (e) Representative olivine types including both strongly zoned Raoul SW olivine with an Fe-rich rim and completely unzoned Sandy Bay Tephra olivine. (f) Crystal clusters. (g) Mafic blebs from Raoul and Healy showing variable crystal contents encased within a microlite-rich mafic melt. cpx, clinopyroxene; ox, oxides (magnetite; ilmenite); plag, plagioclase; ol, olivine; amph, amphibole. (See text for details and discussion.)

are dominated by unzoned, or slightly zoned <5 mm single or clustered crystals (Fig. 8f).

Clinopyroxene trace element variations mirror the two compositional groups identified by major elements (Fig. 12). Two trends occur in clinopyroxene REE patterns for Raoul, Macauley and Healy, corresponding to Mg-rich (low-REE) and Fe-rich (>5–$10\times$ higher-REE concentrations), the latter being similar to or slightly

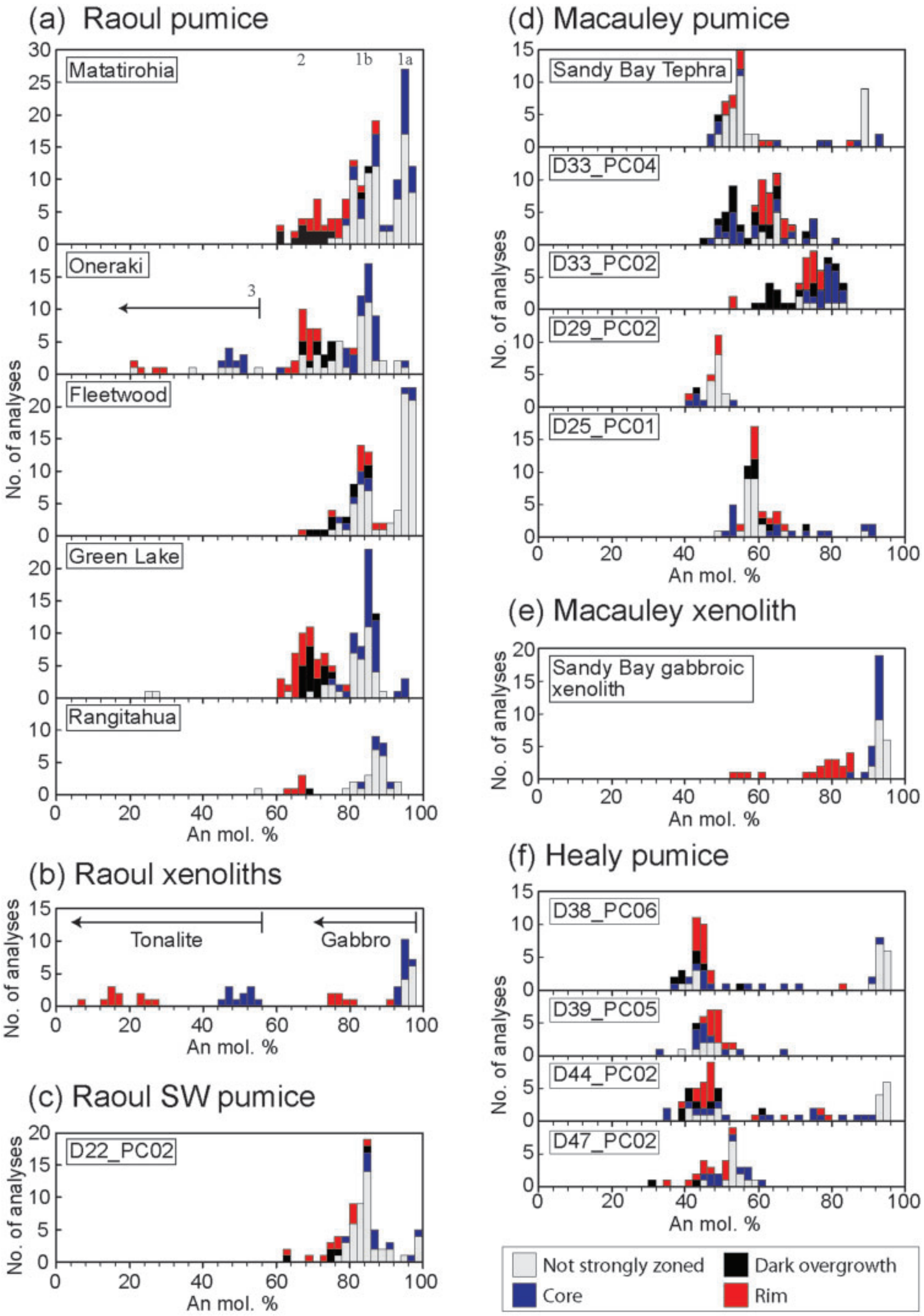

Fig. 9. Plagioclase compositions in representative pumice and xenoliths. Plagioclase anorthite content [An = 100 Ca/(Ca + Na + K)] for both unzoned and zoned crystals from: (a) Raoul pumices from five eruptions with three dominant modes numbered (see text for discussion); (b) Raoul xenoliths from the Matatirohia deposit including the cumulate olivine gabbro and tonalite; (c) Raoul SW pumice; (d) Sandy Bay Tephra pumice and four submarine dredged pumices from Macauley; (e) olivine gabbro xenolith from the Sandy Bay Tephra; (f) four submarine dredged pumices from Healy. (See Electronic Appendix C, Table C7 for raw data.)

greater in value than the corresponding whole-rock concentrations. In addition, trace element data show two Mg-rich sub-populations for Raoul and the Sandy Bay Tephra samples (Fig. 12a and b). The most primitive clinopyroxenes at Macauley have the lowest REE concentrations and the highest Cr values (Fig. 12b). At Healy, trace elements distinguish two clinopyroxene types more clearly than major elements (Fig. 12c).

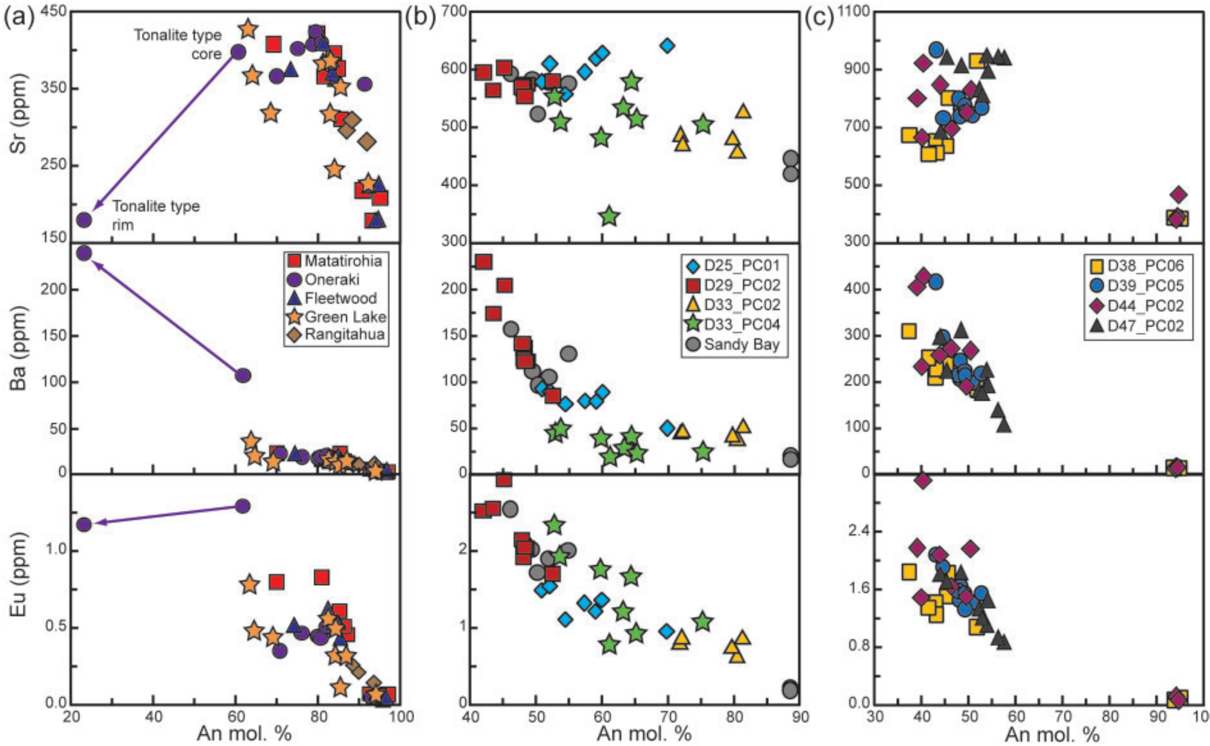

Fig. 10. Selected trace element vs anorthite content variation diagrams for plagioclase crystals in pumices from (a) Raoul, (b) Macauley and (c) Healy volcanoes. Arrow represents core-to-rim composition of a tonalite-type plagioclase. (See Electronic Appendix C, Table C13 for raw data.)

Amphibole

Amphibole occurs as a minor phase in Healy pumices (<5% of crystals) and in trace amounts (<1%) in pumices from Raoul SW, typically as acicular single crystals or in microcrystalline clots (Fig. 8). In addition, amphibole occurs in plutonic tonalite xenoliths from Raoul. Most amphiboles observed in pumices are unzoned or slightly zoned (e.g. Fig. 8c), with several crystals containing high-TiO_2 cores (Fig. 12d). Healy amphiboles have enriched REE patterns, which are LREE-depleted and have slight heavy REE (HREE) depletion (Fig. 12d; Brophy *et al.*, 2011), consistent with amphibole partition coefficients (Rollinson, 1993).

Orthopyroxene

Orthopyroxene is a minor phase (<5–10% of crystals) occurring as <5 mm long single crystals (Fig. 8d), or in crystal clusters with clinopyroxene and plagioclase (Fig. 8f). The majority of crystals have a narrow compositional range with no zoning (Fig. 13a). Compositional outliers that have strongly zoned Mg-rich cores (e.g. Fig. 8d) occur in the Matatirohia, Oneraki, and Fleetwood samples from Raoul and the Sandy Bay Tephra from Macauley.

Olivine

Olivine occurs as rare (≪1 vol. %) 1–5 mm single crystals and within mafic blebs in samples from all four volcanoes studied. Many isolated crystals have a thin selvedge of dark grey, microlite-rich glass and, despite being hosted in dacite pumice, disequilibrium features are relatively uncommon, with most crystals being unzoned or having <10–20 μm rims (Fig. 8e). Olivines between Fo_{70} and Fo_{84} (Fig. 13b) occur in the Matatirohia and Fleetwood pumices from Raoul, displaying both normal and reverse zoning, similar to olivines from the mafic bleb and gabbroic xenolith. At Macauley, olivine occurs in the Sandy Bay Tephra (Fo_{68-78}), dredge sample D33_PC04 (Fo_{80-90}), and the Sandy Bay gabbro xenolith (Fo_{76-78}) (Fig. 13b). At Healy, olivine (Fo_{72-82}) occurs in samples D38_PC06 and D44_PC02. For Raoul SW, in contrast, olivines are often zoned (Fig. 8e) and are in the range of Fo_{78-88}, with some reverse zoned crystals with rims that are 4–6% richer in Fo (Fig. 13b).

Fe–Ti oxides

Fe–Ti oxides are common in pumices from all four volcanoes studied, often attached to or included in Fe-rich clinopyroxenes and orthopyroxenes. Raoul pumices contain only titanomagnetite, which shows a wide compositional range, dominantly Mnt_{55-75}, but with some crystals (typically in mafic blebs) up to Mnt_{87} (Electronic Appendix C, Table C10). All Macauley samples contain titanomagnetite (Mnt_{50-70}), but only the Sandy Bay Tephra and dredged sample D33.PC04 contain ilmenite (Ilm_{85-87}). Pumices from Healy and Raoul SW, in contrast, show a narrow range of titanomagnetite compositions (Mnt_{72-82}) and also contain ilmenite (Ilm_{70-80}) (Electronic Appendix C, Tables C10 and C11).

Glass chemistry

As many pumice samples contained mafic blebs and/or large xenocrysts, major element analyses were carried out on matrix glasses to assess the effects of mixing on whole-rock chemistry. Glass from Raoul pumice has generally >70 wt % SiO_2, with compositional trends that contrast with the whole-rock data (Fig. 14a), particularly for the Matatirohia, Oneraki, and Fleetwood pumices, which contain mafic blebs, and have slightly higher crystal contents (3–5 vol. %) than the Green Lake pumices (<1–2 vol. %). A mixing vector that points towards the mafic bleb whole-rock composition parallels many of the trends on variation diagrams (Fig. 14a), and the glass compositions are difficult to distinguish by eruption. Raoul SW glass compositions continue the linear compositional trend on selected variation diagrams up to ~77·5 wt % SiO_2. Glass compositions from Macauley pumices plot in compositional fields consistent with those observed from whole-rock data (Fig. 14b). Apart from one sample (D25.PC01), all pumice glasses have >72 wt % SiO_2. Three clasts (including the Sandy Bay Tephra) have similar compositions to pumices analysed by M. D. Rotella *et al.* (unpublished data); however, two pumices have distinctively lower K_2O. Contrasts between whole-rock and glass compositions at Macauley are consistent with the observed mineralogy. For example, high MgO and CaO in the north caldera flank pumice (D33.PC04) can be explained by addition of olivine and/or high-Mg clinopyroxenes. There are also significant differences between the whole-rock major element chemistry and glass compositions at Healy (Fig. 14c), in part reflecting the presence of up to 10–15 vol. % crystals. Despite these differences in relative crystal content, the Healy glasses span a narrow compositional range.

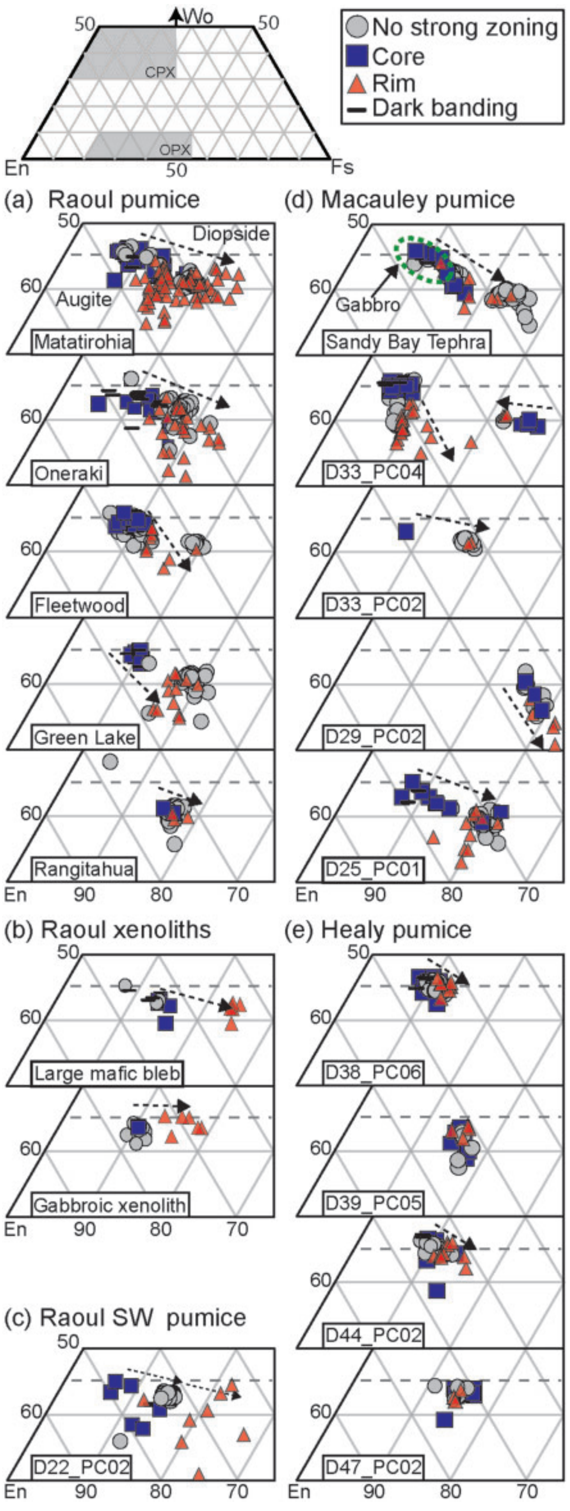

Fig. 11. Clinopyroxene compositions in representative pumices and xenoliths from the Kermadec volcanoes displayed on stacked Enstatite–Ferrosilite–Wollastonite (En–Fs–Wo) ternary diagrams. Compositions calculated as En = 100 Mg/(Ca + Mg + Fe), Fs = 100 Fe/(Ca + Mg + Fe), and Wo = 100 Ca/(Ca + Mg + Fe). Enlarged area for clinopyroxene (cpx) is highlighted in grey on the ternary diagram at the top. Compositions are displayed for both unzoned and zoned

Fig. 11 Continued

crystals as denoted by marker type. Only zones that vary by >3 wt % FeO are shown. Black dashed arrows indicate the direction of core to rim compositional variation. (a) Raoul pumices from five eruptions; (b) Raoul xenoliths from the Matatirohia deposit including large mafic bleb and the cumulate olivine gabbro; (c) Raoul SW pumice; (d) the Sandy Bay Tephra and four pumices dredged from Macauley; (e) four pumices dredged from Healy. In (d) the compositional field (dashed line) for unzoned clinopyroxene from the olivine gabbro xenolith is shown. (See Electronic Appendix C, Table C5 for raw data.)

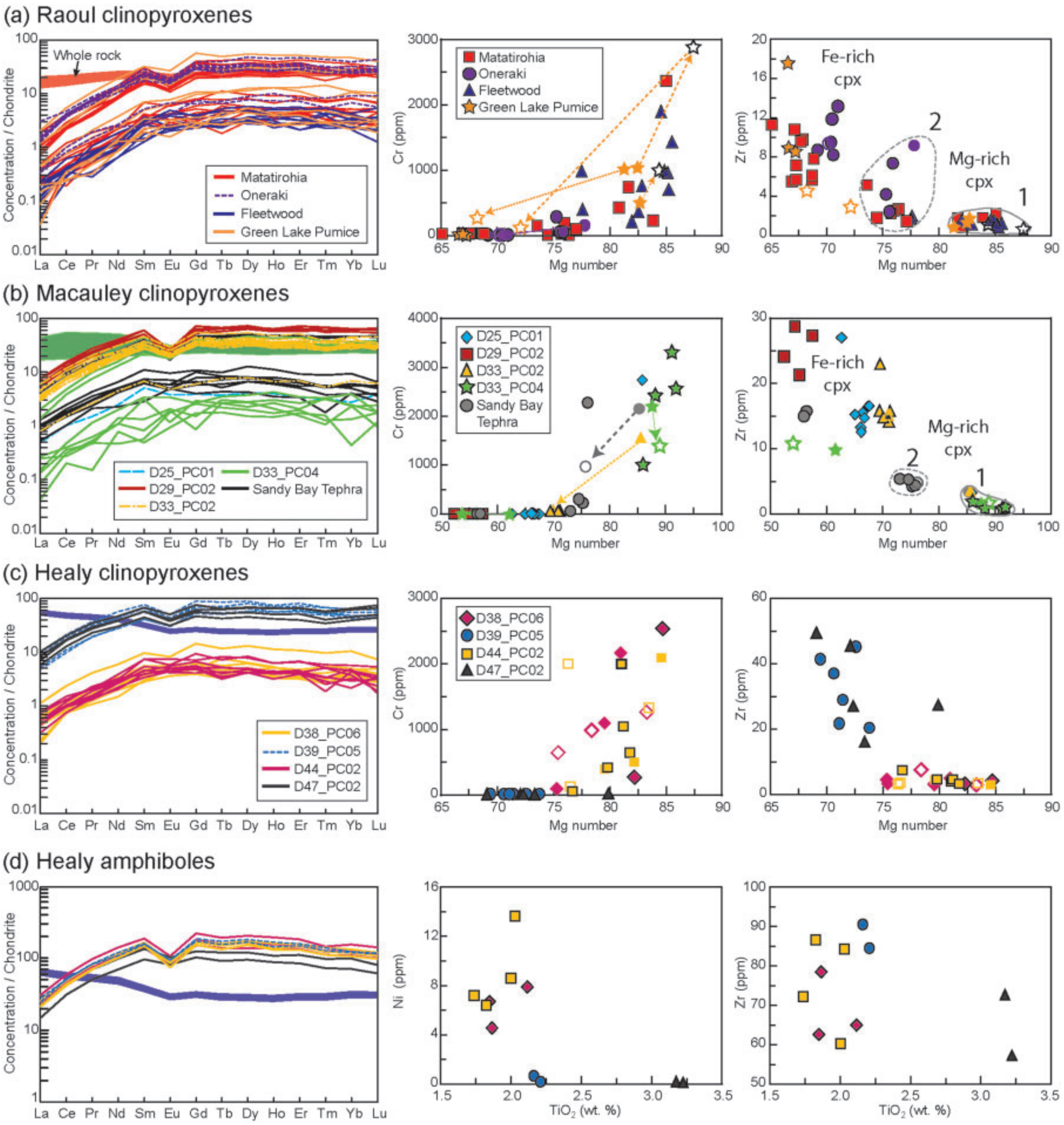

Fig. 12. Clinopyroxene and amphibole trace element characteristics. Chondrite normalization values from Palme & Beer (1993). Mg# $= 100\text{Mg}/(\text{Mg} + \text{Fe}_{\text{total}} + \text{Mn})$. Clinopyroxene compositions from (a) four pumices from different eruptions from Raoul, (b) Sandy Bay Tephra and four submarine dredged pumices from Macauley, and (c) four pumices from Healy. (d) Amphibole compositions from four pumices from Healy; colours and symbols as in (c). Shaded region on REE diagrams represents the total whole-rock trace element compositions of pumices from the respective volcanoes. The zones of strongly zoned crystals are marked accordingly: filled symbols with no outline are cores, open coloured symbols are rims, and open black symbols are dark bands. Analyses from single zoned crystals are joined by dashed coloured arrows on the Cr variation diagram to illustrate variations between zones within single crystals for the Raoul and Macauley samples. The two clinopyroxene types from Raoul are labelled on the Zr variation diagrams, and Mg-rich sub-groups 1 and 2 from Raoul and Macauley are labelled and outlined with continuous and dashed lines respectively (see text for discussion). Mineral trace elements were not determined for samples from Raoul SW. (See Electronic Appendix C, Tables C12 and C14 for raw data.)

Oxygen isotope compositions

As pumices show evidence for magma mixing, oxygen isotope compositions were determined for single crystals, rather than from whole pumices. Crystals selected were first analysed for major elements (and trace elements where feasible) before oxygen isotope analyses were undertaken. Despite large differences in major and trace element compositions, crystals from the Kermadec pumices show only small variations in δ^{18}O between mineral populations (Table 2). The minor differences between clinopyroxene

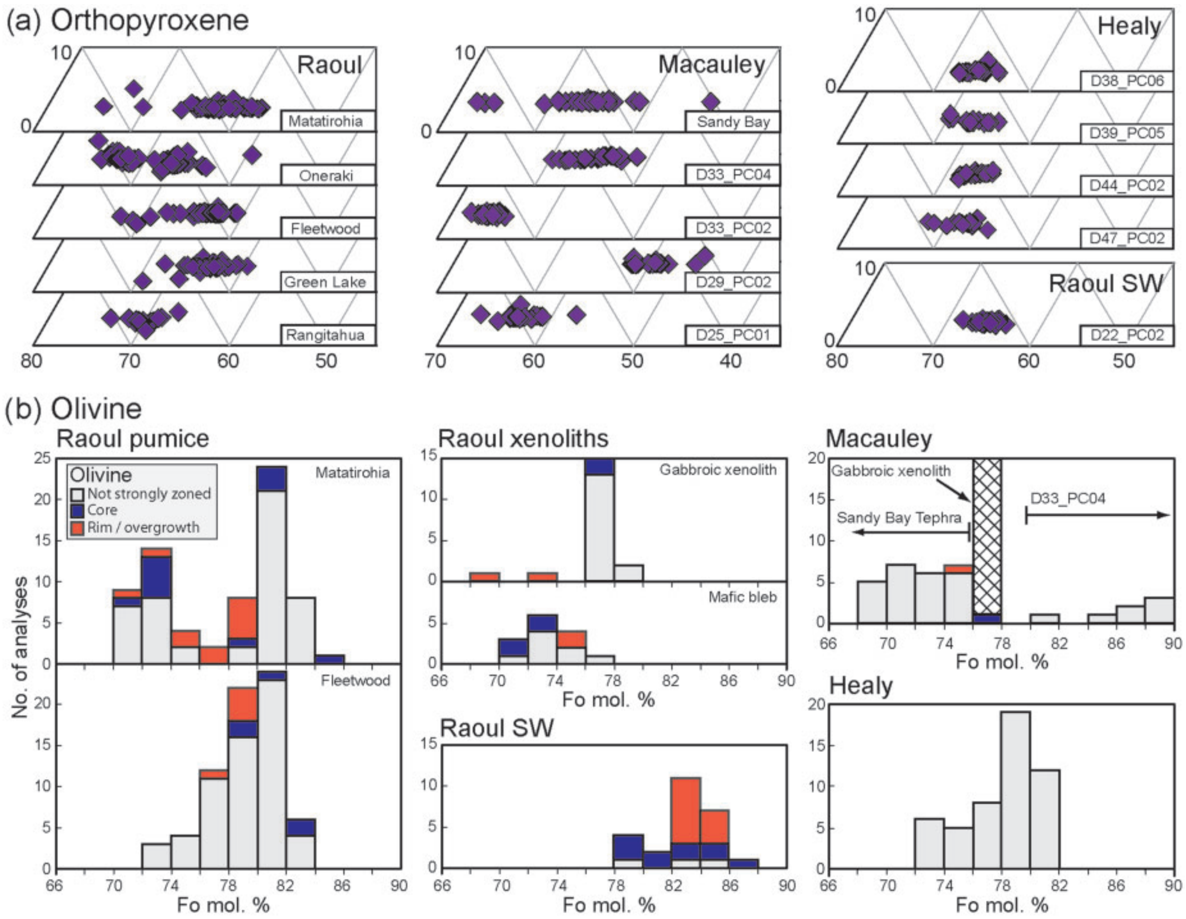

Fig. 13. Orthopyroxene and olivine compositions in representative pumices and xenoliths. (a) Orthopyroxene compositions displayed on stacked Enstatite–Ferrosilite–Wollastonite (En–Fs–Wo) ternary diagrams. Compositions reported as En = 100 Mg/(Ca + Mg + Fe), Fs = 100 Fe/(Ca + Mg + Fe) and Wo = 100 Ca/(Ca + Mg + Fe). Enlarged area for orthopyroxene (opx) is highlighted on the complete ternary diagram in Fig. 11. (b) Histograms stacked by volcano showing the variation in forsterite (Fo) content [Fo = 100 Mg/(Mg + Fe)] for unzoned and zoned olivines. (See Electronic Appendix C, Table C6 (orthopyroxene) and Table C8 (olivine) for raw data.)

types are interpreted to reflect Fe–Ti oxide and apatite inclusions that typically have low $\delta^{18}O$ values (Bindeman, 2008), slightly biasing the bulk crystal values. Plagioclase and olivine show only small variations, with values that would be expected from crystallization of normal arc mantle melts (Eiler *et al.*, 2000), and the mottled and altered plagioclase from Raoul pumice is lower by only ~0·5–1·0‰. Notably, low-An plagioclases have ~0·2–0·4‰ higher $\delta^{18}O$ values than the corresponding high-An plagioclase. The overall range of $\delta^{18}O$ corresponds closely to values observed in fresh MORB lavas (Eiler, 2001), in agreement with $\delta^{18}O$ measured in Kermadec glasses (Haase *et al.*, 2011).

INTENSIVE PARAMETERS AND EQUILIBRIUM CALCULATIONS

A range of methods has been used to determine the temperature, pressure, volatile contents, and oxygen fugacity of the Kermadec magmas, consistent with the differing mineral assemblages in each volcano sample suite.

The Fe–Ti two-oxide thermo-oxybarometer (Ghiorso & Evans, 2008) was used for Healy, Macauley and Raoul SW samples where both magnetite and ilmenite were present (Fig. 15a). Healy samples show a lower-temperature higher-fO_2 group [840–860°C; NNO (nickel–nickel oxide) + 1·0 to + 1·1], and a higher-temperature lower-fO_2 group (840–920°C; NNO + 0·7 to + 0·95). Macauley data cluster into two groups by sample D33.PC04 (920–<940°C and NNO + 0·05 to + 0·15) and the Sandy Bay Tephra sample (940–970°C; NNO −0·20 to + 0·05). In addition, the parameterizations presented by Ridolfi *et al.* (2010) were applied to amphibole compositions. Temperature estimates are similar to those from Fe–Ti oxide thermometry, but cover a wider range of temperatures from ~800 to 950°C for Healy and from ~760 to 860°C for Raoul SW (Fig. 15b and c). Amphiboles from Healy show two distinct groups in model values. The first group yields model

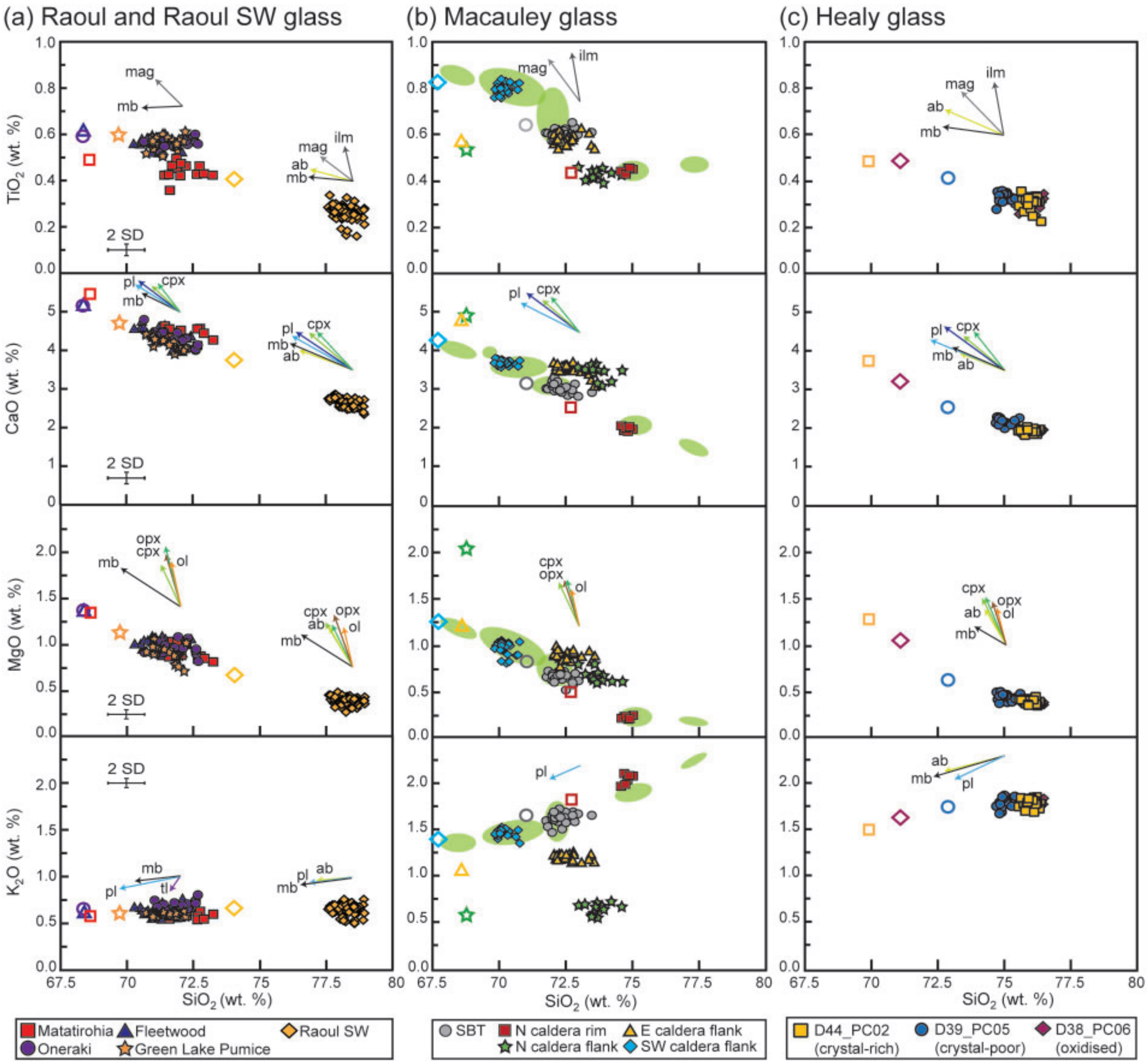

Fig. 14. Major element glass compositions with corresponding whole-rock compositions from Kermadec pumices. Filled symbols represent single glass analyses by EMPA. Shaded fields are compositional groups from M. D. Rotella *et al.* (unpublished data). Open symbols represent whole-rock compositions from the same pumice samples. Data have been normalized to 100% on a volatile-free basis. Arrows are vectors indicating in which direction addition of various crystal types or mafic blebs would drive the glass compositions (the opposite directions represent melt evolution with crystallization). Vectors are calculated from typical compositions of crystal phases found within pumice: pl, plagioclase (dark shade is high-An plagioclase, light shade is low-An plagioclase); cpx, clinopyroxene (dark shade is Mg-rich clinopyroxene, light shade is Fe-rich clinopyroxene); opx, orthopyroxene; ol, olivine; ab, amphibole; mag, magnetite; ilm, ilmenite. mb represents the vector calculated from the average whole-rock composition of mafic blebs from the corresponding volcano (Table 1). (See Electronic Appendix C, Table C4 for raw data.) The 2 SD uncertainties are calculated from repeated analysis of glass standards (Electronic Appendix B). Uncertainties for XRF analyses are typically less than the size of the symbols.

temperatures of 800–870°C, 4·4–5·3 wt % H_2O and pressures of 100–160 MPa, whereas the second has model temperatures of 900–950°C, 5–6 wt % H_2O and ~190–290 MPa. For the first cluster, the Ridolfi *et al.* (2010) ranges of model pressures and water contents are consistent with those from melt inclusions (Saunders, 2009). The majority of the analyses used for modelling are from unzoned crystals rims; however, strongly zoned crystal cores correspond to higher model temperatures, water contents and pressures. Amphiboles from Raoul SW also cluster into two groups, with a high-temperature group at ~860°C, <6·4 wt % H_2O and pressures of ~160 MPa, and a lower temperature group at 780–810°C, 5–6 wt % H_2O and ~80–120 MPa. Unaltered amphibole cores from the tonalite xenolith yield even lower temperatures of 760–795°C and pressures of 65–90 MPa.

Table 2: Oxygen isotope compositions of mineral types from selected Kermadec pumices

Volcano	Crystal type	Type	$\delta^{18}O$ (‰)
Raoul	Clinopyroxene (silicic)	Fe-rich (Mg# 68)	4·5*
Macauley	Clinopyroxene (silicic)	Fe-rich (Mg# 56)	5·1*
Raoul	Clinopyroxene (xenocryst)	Mg-rich (Mg# 85)	5·0
Macauley	Clinopyroxene (xenocryst)	Mg-rich (Mg# 85)	5·7
Healy	Clinopyroxene (xenocryst)	Mg-rich (Mg# 85)	5·2
Raoul	Olivine (xenocryst)	Unzoned (Fo_{81})	5·1
Macauley	Olivine (xenocryst)	Unzoned (Fo_{75})	4·9
Healy	Olivine (xenocryst)	Unzoned (Fo_{80})	5·1
Raoul	Plagioclase (silicic)	Zoned, low-An (An_{68})	5·7
Macauley	Plagioclase (silicic)	Unzoned, low-An (An_{50})	5·8
Healy	Plagioclase (silicic)	Unzoned, low-An (An_{45})	5·6
Raoul	Plagioclase (xenocryst)	Unzoned, high-An (An_{97})	5·3
Macauley	Plagioclase (xenocryst)	Unzoned, high-An (An_{89})	5·6
Healy	Plagioclase (xenocryst)	Unzoned, high-An (An_{95})	5·3
Raoul	Plagioclase (tonalite?)	Mottled, low-An (An_{50} core, An_{23} rim)	4·8
Raoul, xenolith	Plagioclase (tonalite)	Mottled, low-An	5·5
Healy	Amphibole (phenocryst)	Unzoned, magnesiohornblende	6·2

*Not considered totally representative of the mineral phase owing to small but abundant (up to ~20%) inclusions of Fe–Ti oxides and apatite.

Thermometers appropriate for other samples are limited by their restricted mineral assemblage and are therefore confined to two-pyroxene or mineral–liquid equilibrium (Putirka, 2008). Previous studies of Raoul dacite mineralogy have suggested that the majority of crystals were far from equilibrium with the host melt, and only crystal rims or small groundmass crystals were in equilibrium with the host melt (Worthington, 1998; Smith *et al.*, 2006, 2010). Multiple crystal populations, with wide compositional ranges, have also been identified in samples from this study. Selected crystal and melt compositions were tested under the equilibrium criteria outlined by Putirka (2008) to assess which minerals were suitable for thermometry (Table 3). Most Kermadec pumices contain minerals that fall within the equilibrium calculations of Putirka (2008), confined mainly to Fe-rich clinopyroxene and orthopyroxene types (typically <Mg# 70) and low-An plagioclase (typically $<An_{75}$ for Raoul plagioclase, $<An_{65-70}$ for Raoul SW and most Macauley plagioclase, and $<An_{50}$ for Healy). Exceptions to this are high-SiO_2 samples from Macauley and Healy, which have pyroxene–glass compositions that fall slightly outside the equilibrium criteria, possibly as a result of late-stage crystallization of other Fe- or Mg-bearing crystal phases such as amphibole. Temperature estimates are relatively consistent for the various thermometers, with only the clinopyroxene–melt thermometer yielding slightly higher values (typically by 30–50°C: Table 3). Temperature estimates from mineral–melt and two-pyroxene thermometers also yield similar temperatures to oxide and amphibole thermometers where these minerals were also present (Fig. 15).

DISCUSSION

The multiple types of data collected in this study underscore the complexity of silicic magma generation in the Kermadec arc. There are, however, several consistent patterns in the combined geochemical and petrological data that illuminate key processes that would otherwise be missed by using conventional bulk-rock analyses. To interpret the overall trends in chemistry, we first consider what potential sources and conditions may have given rise to the diverse mineralogies and xenoliths found within the Kermadec pumices. Then we examine the different lines of evidence to reassess the dominant petrogenetic processes responsible for the origin of silicic magmas. Finally, we use these interpretations to draw inferences about the

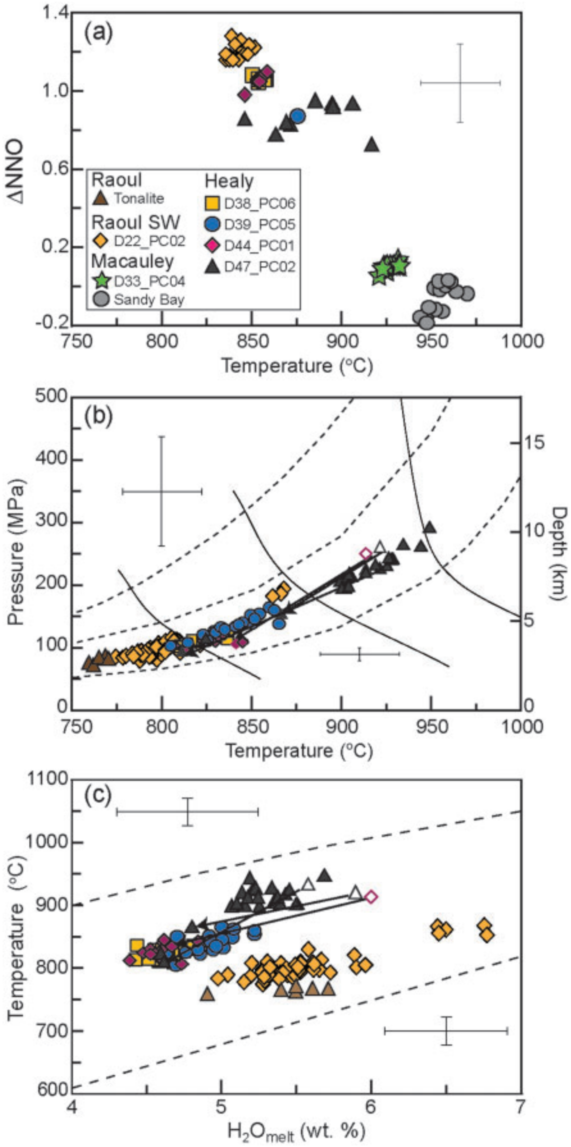

Fig. 15. Intensive parameters calculated for selected pumices from Macauley, Raoul SW and Healy volcanoes and tonalite from Raoul volcano. (a) Temperature and fO_2 [plotted as $\log_{10} fO_2$ relative to the Ni–NiO oxygen buffer of O'Neill & Pownceby (1993)] estimates from Healy, Macauley and Raoul SW, calculated from matched pairs of magnetite and ilmenite using the Fe–Ti exchange based thermometer of Ghiorso & Evans (2008). Only coexisting Fe–Ti oxide pairs (either sharing a common boundary or occurring together in the same phenocryst) were used to ensure textural equilibrium (Blundy & Cashman, 2008). Fe–Ti pairs were also tested for equilibrium using the Mg/Mn partioning test from Bacon & Hirschmann (1988). (b) Temperature and pressure estimates based on amphibole compositions using the thermometer and barometer of Ridolfi *et al.* (2010). Relative depth is calculated for oceanic crust, assuming a density of 2890 kg m^{-3}, and neglecting the overlying water column. Strongly zoned core–rim analyses from the same amphibole crystal are joined by tie lines with cores represented by open symbols. Error bars represent 2σ, calculated as the maximum uncertainty with changing amphibole composition (Ridolfi *et al.*, 2010). Symbols as in (a). (c) Temperature and water content estimates based on amphibole compositions using the thermometer and hydrometer of Ridolfi *et al.* (2010). Symbols as in (a); tie lines and error bars as in (b).

structure of the magmatic systems at these four Kermadec volcanoes.

Magmatic conditions: clues from the crystals

Origins of the observed crystal assemblages

The majority of pumices contain multiple crystal populations, some of which are close to equilibrium with their host glasses. Most, however, show disequilibrium, indicating that they have crystallized in melts of contrasting composition. Magma mixing and/or assimilation, expressed as mafic blebs and xenocrysts, has influenced the mineralogy and bulk compositions of many of the Kermadec pumices. Two major questions arise from these observations.

(1) What are the sources of the identified crystal populations?
(2) What is the crystal population's genetic, spatial, and temporal affiliation with the silicic melts?

To address these questions, we draw attention to the different crystal populations identified in pumice samples compared with those analysed in co-eruptive plutonic xenoliths and mafic inclusions (Figs 9, 11 and 13). Major element compositions of clinopyroxene, olivine and plagioclase from both the gabbro and the single mafic bleb correspond closely to the compositions of Mg-rich clinopyroxene, high-An plagioclase and olivine analysed from both smaller mafic blebs as well as single crystals identified in felsic pumices. Plagioclase compositions of zoned crystals in tonalite xenoliths also closely match those of the mottled low-An population of single plagioclase found in both the Oneraki and Green Lake Pumice samples. Given the close similarities between crystal populations in the plutonic xenoliths and those single crystals within single pumice samples, it is inferred that many crystals in pumices are derived from the host-rocks to the young felsic magma bodies. We propose that the close spatial proximity of the plutonic bodies to the silicic magmas resulted in magma mixing and/or assimilation, with the plutonic bodies representing either solid country rock or partially molten cumulates. The degree of assimilation and/or mixing with the mafic source varies considerably, with some xenolithic material represented only by single crystals with adhering silicic pumice glass, and other xenoliths represented by large centimetre-sized mafic blebs, or loose coherent blocks of plutonic material. The amount of material involved in magma mixing and/or assimilation also varies widely between samples as expressed by the variation in crystal populations between pumices, and also identified by offsets between glass and whole-rock compositions (Fig. 14).

Temporal relationships between the source of the mafic crystals and the host silicic magmas are difficult to interpret, especially for submarine dredged samples as there is

Table 3: Calculated temperatures (°C) and equilibrium compositions for Kermadec silicic magmas using mineral–mineral and mineral–liquid thermometers

Thermometer	Raoul volcano					Macauley volcano					Healy and Raoul SW volcanoes				
	eruption	av.	range	eq. comp.	*n*	sample	av.	range	eq. comp.	*n*	sample	av.	range	eq. comp.	*n*
Two-pyroxene (Brey & Kohler, 1990)	Matatirohia	922	886–974	Mg# 58–66	17	D25 PC01	946	908–987	Mg# 62–66	17	D38 PC06	*x*	*x*	*x*	*x*
	Oneraki	950	920–984	Mg# 63–70	16	D29 PC02	910	899–924	Mg# 49–51	3	D39 PC05	959	955–963	Mg# 68–69	3
	Fleetwood	931	899–980	Mg# 65–70	14	D33 PC02	*x*	*x*	*x*	*x*	D44 PC01	*x*	*x*	*x*	*x*
	Green Lake	928	868–1004	Mg# 62–66	10	D33 PC04	888	878–897	Mg# 54–58	5	D47 PC02	896	881–922	Mg# 69–70	5
	Rangitahua	955	926–995	Mg# 67–72	13	Sandy Bay	910	886–939	Mg# 55–60	11	D22 PC03	943	927–955	Mg# 61–63	4
Two-pyroxene (Putirka, 2008)	Matatirohia	934	905–978	Mg# 58–66	17	D25 PC01	943	916–975	Mg# 62–66	17	D38 PC06	*x*	*x*	*x*	*x*
	Oneraki	965	934–1013	Mg# 63–70	16	D29 PC02	911	908–917	Mg# 49–51	3	D39 PC05	931	928–934	Mg# 68–69	3
	Fleetwood	951	938–971	Mg# 65–70	14	D33 PC02	*x*	*x*	*x*	*x*	D44 PC01	*x*	*x*	*x*	*x*
	Green Lake	935	888–968	Mg# 62–66	10	D33 PC04	866	862–870	Mg# 54–58	5	D47 PC02	880	864–897	Mg# 69–70	5
	Rangitahua	998	930–1032	Mg# 67–72	13	Sandy Bay	914	901–931	Mg# 55–60	11	D22 PC03	859	849–868	Mg# 61–63	4
Cpx–liquid (Putirka *et al.*, 2003)	Matatirohia	1002	921–1033	Mg# 63–68	30	D25 PC01	988	977–992	Mg# 62–64	9	D38 PC06	*x*	*x*	*x*	*x*
	Oneraki	1013	1003–1023	Mg# 63–70	28	D29 PC02	*x*	*x*	*x*	*x*	D39 PC05	*x*	*x*	*x*	*x*
	Fleetwood	1000	978–1023	Mg# 65–72	14	D33 PC02	986	975–993	Mg# 68–70	10	D44 PC01	*x*	*x*	*x*	*x*
	Green Lake	999	967–1014	Mg# 63–70	57	D33 PC04	951	941–959	Mg# 54–62	10	D22 PC03	931	925–941	Mg# 61–63	3
						Sandy Bay	937	926–946	Mg# 56–59	6					
Opx–liquid (Putirka, 2008)	Matatirohia	925	914–940	Mg# 60–69	44	D25 PC01	943	932–950	Mg# 56–62	24	D38 PC06	880	872–882	Mg# 61–65	11
	Oneraki	984	967–1020	Mg# 61–68	42	D29 PC02	*x*	*x*	*x*	*x*	D39 PC05	870	864–873	Mg# 62–66	11
	Fleetwood	974	960–1000	Mg# 60–69	45	D33 PC02	942	934–951	Mg# 63–67	24	D44 PC01	871	867–874	Mg# 62–65	10
	Green Lake	970	952–994	Mg# 58–67	39	D33 PC04	899	887–913	Mg# 51–58	24	D22 PC03	855	845–862	Mg# 61–64	37
						Sandy Bay	913	897–921	Mg# 50–56	21					
Plag–liquid (Putirka, 2005, 2008)	Matatirohia	969	959–974	An_{59-78}	33	D25 PC01	939	932–944	An_{50-65}	50	D38 PC06	859	851–867	An_{37-50}	27
	Oneraki	978	967–977	An_{63-77}	39	D29 PC02	877	866–883	An_{40-52}	25	D39 PC05	873	859–876	An_{40-55}	31
	Fleetwood	983	977–985	An_{66-77}	10	D33 PC02	944	937–948	An_{59-72}	19	D44 PC01	858	848–866	An_{35-49}	26
	Green Lake	962	957–967	An_{61-75}	48	D33 PC04	936	925–943	An_{49-65}	57	D22 PC03	873	869–875	An_{60-67}	3
						Sandy Bay	919	910–929	An_{46-62}	43					

Temperatures calculated from matched mineral–glass pairs that fall within the equilibrium criterion for each thermometer as outlined by Putirka (2008), where $K_D(\text{Fe–Mg})^{\text{cpx–opx}} = 1{\cdot}09 \pm 0{\cdot}14$, $K_D(\text{Fe–Mg})^{\text{cpx–liq}} = 0{\cdot}27 \pm 0{\cdot}3$, $K_D(\text{Fe–Mg})^{\text{opx–liq}} = 0{\cdot}29 \pm 0{\cdot}6$ and $K_D(\text{Ab–An}) = 0{\cdot}1 \pm 0{\cdot}05$. Samples that did not have minerals or melt that met the equilibrium range are marked with an *x*. Pressure was set at 150 MPa for all thermometers based on amphibole barometry. Water in plagioclase–liquid thermometer was set at 5 wt % for Raoul SW samples, 4·5 wt % for Healy samples based on amphibole hydrometry, and estimated at 4 wt % for Macauley and Raoul samples. Column 'eq comp.' is the composition of the minerals that met the equilibrium criterion and were used for thermometry, *n*, number of pairs used for thermometry calculations.

no constraining stratigraphy. However, crystal chemistries reported by Smith *et al.* (2003*a*, 2006) on Macauley and Raoul basalts and basaltic-andesites generally overlap in major element composition with the mafic minerals from the pumices in our study. In addition, the bulk compositions of two Matatirohia mafic blebs plot within the low-Fe and low-Ti porphyritic suite of basaltic samples from the 4–10 ka Moumoukai lavas, which immediately pre-date the Ngaio Group dacites (Smith *et al.*, 2010), suggesting that they have a similar origin (Fig. 16). The mineral trace element chemistry of xenocrystic clinopyroxene has been used to back-calculate the composition of the equilibrium mafic liquids, resulting in compositions closely similar to those of the mafic blebs and/or previously erupted basalts (Fig. 17a).

Temporal relationships can be partially constrained for the tonalite source, which has been assimilated into the Oneraki and Green Lake Pumice units at Raoul volcano. Mortimer *et al.* (2010) reported a zircon U–Pb age (by LA-ICP-MS) of 1·25 ± 0·06 Ma from a single tonalite fragment collected from lithic breccias in the Matatirohia deposits, which is petrographically identical to the tonalite xenolith investigated in this study (PETLAB database: http://pet.gns.cri.nz/). If these tonalites share the same origin, they are considerably older than the host Ngaio group dacite deposits, suggesting that silicic magmatism is not necessarily confined to the recent (<4 kyr) Raoul magmatic system (see Smith *et al.*, 2003*b*). As the whole-rock REE pattern of the tonalite analysed in this study is subparallel to the patterns obtained for the dacite pumice units (Fig. 6) it is inferred that the tonalites represent an earlier episode of felsic magmatism (and volcanism?) similar to the <4 ka system. As the tonalite has undergone variable amounts of high-temperature hydrothermal alteration, the host plutonic body could be present within the hydrothermal envelope of Raoul Island. This is also supported by elevated whole-rock $^{87}Sr/^{86}Sr$ ratios and lower $\delta^{18}O$ for the mottled low-An plagioclase. Assimilation of tonalite minerals into the dacite magma indicates that interaction may have occurred close to the magmatic–hydrothermal interface, which could be as shallow as 2 km for Raoul (Graaf, 2006). Amphibole barometry for the tonalite further supports shallow magma emplacement and hydrothermal interaction (Fig. 15).

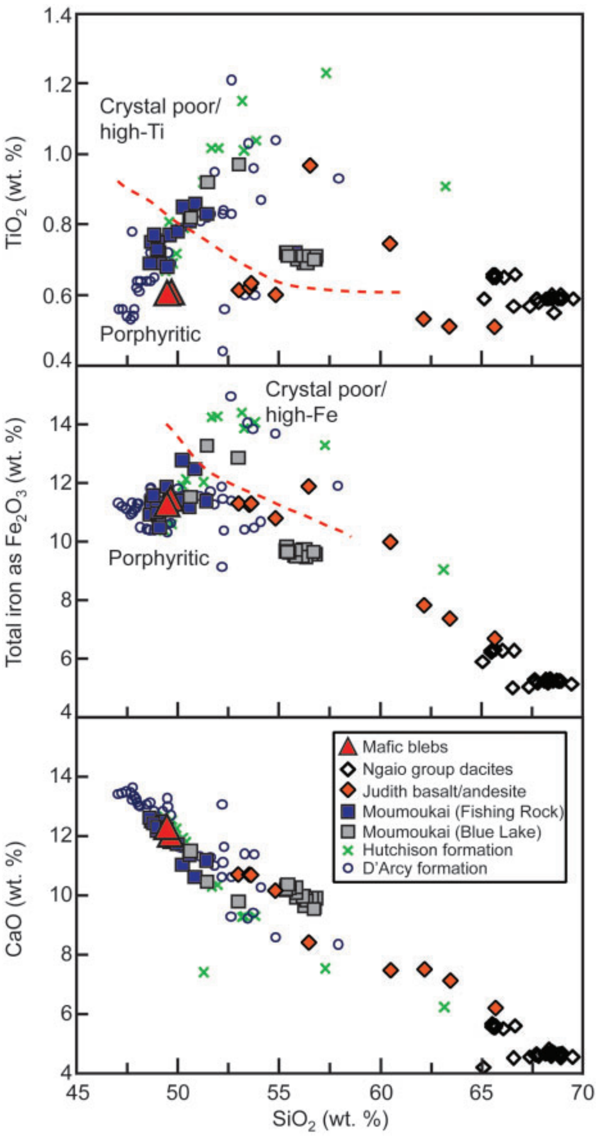

Fig. 16. Selected major element variation diagrams for mafic blebs from the Matatirohia deposit compared with published data from Smith *et al.* (2006, 2010). Filled symbols represent the youngest basaltic to basaltic andesite material. Large triangles represent two whole mafic blebs analysed in this study. Other symbols are older basaltic and basaltic andesite units and silicic units from the Ngaio Group eruptions (from Smith *et al.*, 2010). The dashed line separates high-Fe/high-Ti aphyric samples from low-Fe/low-Ti porphyritic samples (Smith *et al.*, 2010). The similar bulk compositions of the mafic blebs to those of previously erupted basalts should be noted.

Compositional zoning: diverse magmatic conditions

Compositional zoning and disequilibrium features (e.g. sieve and resorption textures) occur in many Kermadec pumice crystal populations. There is a diverse range of zoning patterns (e.g. normal, reverse, oscillatory), which vary in degree and in compositional range between crystal phases, single samples and volcanoes. There are two end-member types of zoning in plagioclase, which record either subtle variations in local conditions (e.g. temperature, water content, pressure, fO_2; Blundy & Wood, 1991; Berlo *et al.*, 2007) or extreme variations probably caused by large differences in melt composition (Bowen, 1913; Johannes & Holtz, 1990; Putirka, 2005). As a case example, Healy plagioclase compositions range from An_{30} to An_{98} (Fig. 9f) with two zoning types. At one extreme crystals display oscillatory zoning (e.g. Fig. 8a), in which there is only ~5–10 An mol % variation between zones, which may be caused by small variations in physical conditions

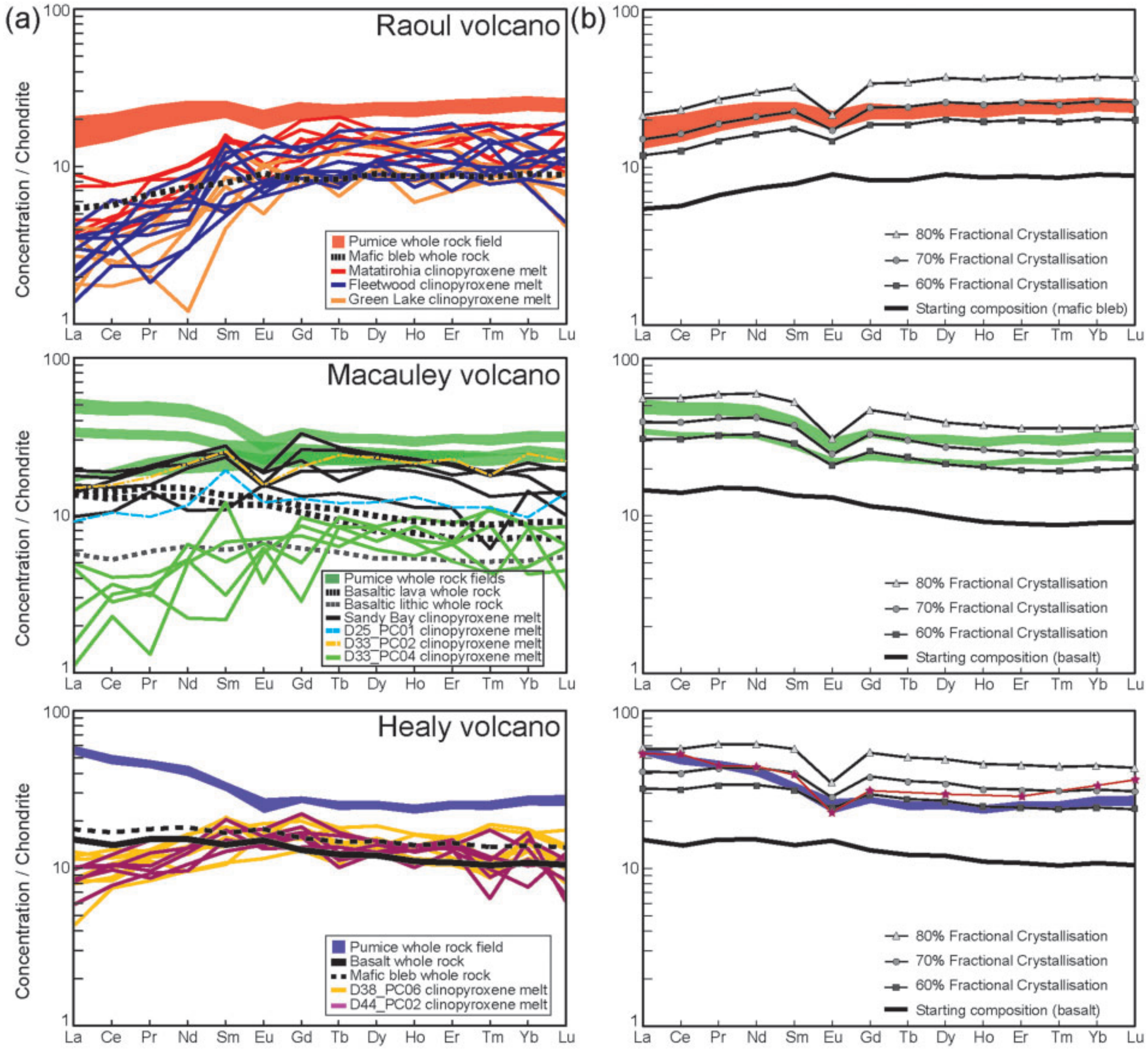

Fig. 17. (a) Calculated melt REE concentrations from mafic clinopyroxene xenocrysts compared with whole-rock REE compositions. Macauley basalts are from Smith *et al.* (2003*a*). The Healy basalt is from I. C. Wright (unpublished data). Clinopyroxene REE partition coefficients are from McKenzie & O'Nions (1991). (b) REE patterns calculated for Kermadec magmas with varying levels of perfect fractional crystallization from a basaltic parent. Mineral proportions used in the fractionation calculations are from Table 4. Also shown is the average Healy melt inclusion REE composition (trend with stars) from Saunders *et al.* (2010). The starting compositions used in the calculations are from the Matatirohia mafic bleb for Raoul, basaltic lava from Smith *et al.* (2003*a*) for Macauley, and basaltic lava from I. C. Wright (unpublished data) for Healy. Partition coefficients are from McKenzie & O'Nions (1991), except for magnetite (Lemarchand *et al.*, 1987) and ilmenite (Paster *et al.*, 1974). Chondrite normalization values from Palme & Beer (1993).

within the magma chamber. At the other extreme there can be as much 50 An mol % variation between zones, which can only be caused by a drastic change in the host melt composition, providing further evidence for magma mixing.

In contrast, many crystals have compositions that are far from equilibrium with their host glasses, but completely lack compositional zoning. For example, the majority of olivines within the Kermadec pumices have only minor (<10–20 μm) or no observed reaction rim. As shown by Coombs & Gardner (2004), in experiments with conditions (885°C, 150 MPa and 4·2 wt % H_2O) comparable with those for the Kermadec magmas, olivine rim growth rates in a rhyodacite melt were found to be relatively rapid at ~1 ±0·5 μm h^{-1}. The lack of reaction rims in the Kermadec pumices implies that in many cases magma mixing between the silicic melts and the mafic-sourced olivines occurred either immediately prior to eruption or conceivably syn-eruptively.

Petrogenesis of silicic magma in the Kermadec arc

The dominant process of differentiation: fractional crystallization or crustal anatexis?

To discriminate between fractionation and crustal anatexis, we consider what the key differences would be between silicic magmas generated by each mechanism. Smith *et al.* (2003*a*, 2003*b*, 2006, 2010) attributed the generation of silicic magmas to lower crustal dehydration melting of mafic amphibolite. In their model, amphibolite forms in the lower oceanic crust once the crust reaches an appropriate thickness (15 km) and heat-flow rate. Silicic magmas are formed in a narrow window of time and, owing to changing chemical and physical parameters, the composition of the melt phase can vary significantly between magma batches (Smith *et al.*, 2003*a*). If, however, silicic magmas at Raoul and Macauley were generated in this fashion, it could be expected that they would have trace element signatures that differ significantly from those of the basalts from the same volcanoes (see Greene *et al.*, 2006; Brophy, 2008). In particular, Brophy (2008) showed that a crystal fractionation origin for silicic magmas will generate positive trends between SiO_2 and REE concentrations, whereas dehydration melting of amphibolite crust leads to negative SiO_2–REE correlations. The silicic magma chemistry from a melting origin would also be expected to vary between magma batches with changes in the degree of melting or variables such as source mineralogy or degree of metasomatism. This study suggests that this is not the case, as the silicic magmas generally have trace element patterns that do not vary significantly between eruptions or chemical groups (with the exception of the outlier composition from Macauley), and are subparallel to the trace element patterns of basaltic material from the respective volcanoes (Fig. 6). Isotopic compositions also show little variation between mafic and silicic magmas (Fig. 7; Haase *et al.*, 2002; Smith *et al.*, 2003*a*, 2006, 2010). In addition, oxygen isotope compositions of both mafic and silicic minerals (this study), as well as basaltic and silicic glasses (Haase *et al.*, 2011), are within the expected range for mantle-derived melts. As highlighted by Geist *et al.* (1995) and Haase *et al.* (2011), melting of hydrothermally formed amphibolite (e.g. Smith *et al.*, 2003*a*) or hydrothermally altered crust would result in melts with noticeably lower $\delta^{18}O$ (e.g. Bindeman, 2008).

Similar problems arise when considering partial melting of silicic amphibole-bearing plutonic material as the main source for generation of the observed magmas. Melting of intermediate or silicic amphibole-bearing plutons by basaltic magmas has been proposed to generate silicic magmas in the Izu–Bonin arc (e.g. Tamura & Tatsumi, 2002; Shukuno *et al.*, 2006; Tamura *et al.*, 2009). Anatexis of a hornblende-bearing intermediate plutonic rock should yield the same REE–SiO_2 systematics as melting of more mafic amphibolite (Brophy, 2008), which is not the case in the Kermadec samples (Fig. 18). In addition, melting of granites previously formed by dehydration melting (e.g. Garrido *et al.*, 2006) would be expected to produce silicic melts with strongly differing chemical compositions compared with those of normal arc basalts. Tonalite xenoliths observed in this study are variably hydrothermally altered, with trace element and isotopic chemistries that would generate silicic melts with distinctive chemical characteristics owing to their altered composition. We infer that the tonalite xenoliths represent plutonic material above the silicic magma chamber (or possibly roof material; e.g. Geist *et al.*, 1995), at depths shallow enough (<2 km) to be within the hydrothermal envelope of Raoul volcano (Graaf, 2006). Crystals of tonalitic origin within the dacite pumices preserve their original zonation and do not have the anhedral or resorbed appearance that would be expected with high degrees of melting by a hot basaltic magma. As tonalite fragments and crystals are relatively rare in Raoul pumices and absent from other Kermadec pumices, we suggest that tonalite assimilation plays only a minor role in the Kermadec magmatic systems.

As an alternative to amphibolite melting, partial melting of basalt could be proposed for generating the range of silicic magma compositions (which would essentially be the reverse of modelling fractional crystallization), as suggested for the South Sandwich arc magmas (Leat *et al.*, 2003, 2007). Large amounts of superheated magma, however, are required to melt basaltic, non-hydrated oceanic crust (especially relatively cold upper crust) and are inconsistent with moderate volumes of silicic eruptive rocks (Geist *et al.*, 1995). Fractional crystallization is thermally an inevitable process in stalled basaltic magmas that can stay partially molten and susceptible to remobilization and melt extraction for long time periods (Koyaguchi & Kaneko, 1999). Nevertheless, partial melting processes cannot be ruled out, as newly arriving magmas could provide new heat and mass into crystallizing magma bodies (Murphy *et al.*, 2000; Bachmann *et al.*, 2002). Distinctive (but relatively uncommon) clinopyroxene crystals with resorbed cores and high-Mg overgrowths (Fig. 8b) provide evidence for some degree of partial melting or remobilization in the Kermadec magmatic systems. High concentrations of Cr and Ni (Fig. 12) in these resorbed crystals could be the result of newly arriving, hot, primitive basalt. However, our overall results provide overwhelming support for crystallization being the dominant differentiation process and crustal partial melting, although inevitably present, being of secondary importance for melt differentiation in the Kermadec volcanoes.

To further assess how much crystallization would be required to generate the observed compositions of the

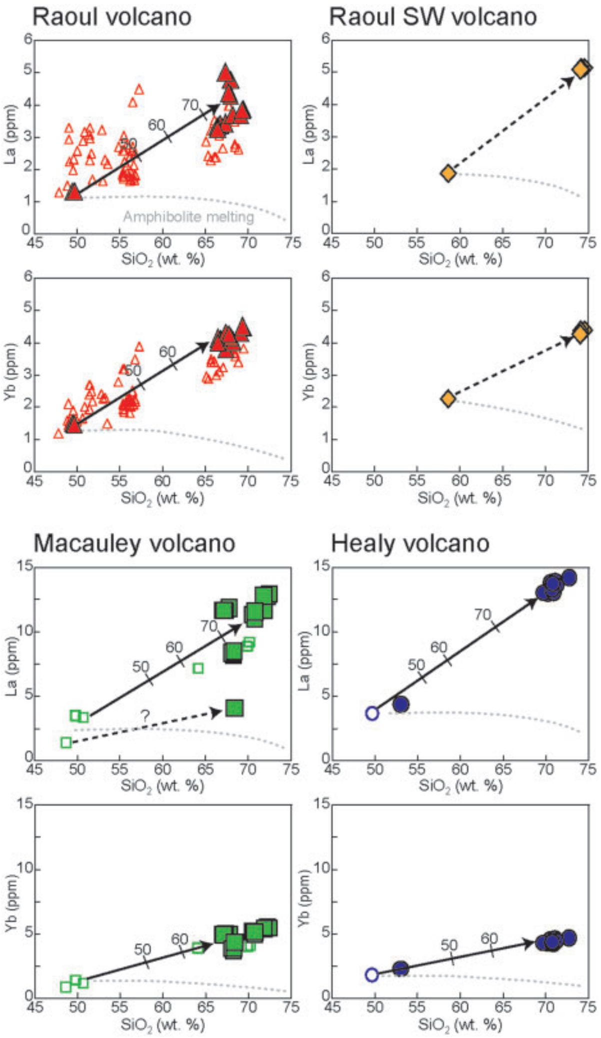

Fig. 18. Whole-rock variation diagrams showing La (LREE) and Yb (HREE) vs SiO$_2$ for samples from the four Kermadec volcanoes investigated in this study. Large filled symbols are from this study; small open symbols are from Smith *et al.* (2006, 2010) for Raoul, Smith *et al.* (2003*a*) for Macauley and I. C. Wright (unpublished data) for Healy volcano. The continuous-line arrows represent the fractional crystallization path from Fig. 17b. The compositional gap corresponding to ~50% crystallization for Raoul basalts should be noted. Dashed arrows are inferred fractional crystallization paths. Dashed grey lines represent a schematic illustration of the compositions that would be expected from amphibolite melting using the model results of Brophy (2008), showing that regardless of the type of melting (equilibrium, fractional, accumulated fractional) REE abundances remain essentially constant and then decrease, or steadily decrease with increasing liquid SiO$_2$ content. The starting composition for amphibolite is assumed to be similar to that of the most primitive samples at each volcano for illustrative purposes. It should be noted that the variation diagrams for Macauley and Healy have different *y*-axis scales from those for Raoul and Raoul SW.

Kermadec silicic magmas, differentiation of basalt has been modelled by least-squares mass balancing of the observed crystal compositions (Table 4; Cabero *et al.*, 2012). For Raoul, ~75% crystallization of basalt (based on the composition of a mafic bleb) yields a near-perfect match for the major element composition of the Green Lake Pumice (the least mixed bulk pumice composition). With ~80% crystallization using the same conditions, the composition of the Raoul SW pumices can be generated. The Sandy Bay Tephra can also be produced through fractional crystallization of magma compositions similar to previously erupted basalts (from Smith *et al.*, 2003*a*) and observed mafic crystal compositions, with TiO$_2$ slightly offset, most probably as a result of late-stage ilmenite crystallization. More evolved pumices at Macauley (e.g. D29_PC03) can also be generated by ~80% crystallization using similar compositions. Compositions from Healy can be modelled by ~80% crystallization of basalt to generate the observed glass compositions (Table 4), and ~75% to generate the bulk (mixed) pumice compositions.

Mineral proportions from major element modelling have been used to model REE abundances assuming perfect fractional crystallization (Fig. 17b). For Raoul, the REE contents of the observed dacites strongly correlate with ~70–75% fractional crystallization. The composition of silicic magmas from Macauley also have REE patterns that are subparallel to those of basalt lavas from Smith *et al.* (2003*a*; Fig. 17b), with pumice compositions occurring as two groups, and consistent with 70–80% fractional crystallization from basaltic lavas. In contrast, although Healy pumices are considerably enriched in REE relative to the basalts, basic fractional crystallization modelling cannot replicate the LREE enrichment or middle REE (MREE) depletion observed in the Healy pumices and melt inclusions analysed by Saunders *et al.* (2010). This REE pattern may be caused either by fractionation of another crystal phase not used in modelling (e.g. apatite, which has high K_d values for MREE), or by extensive late-stage amphibole crystallization from the evolved melt, as LREE have considerably lower partition coefficients in amphiboles than MREE or HREE in silicic magmas (Rollinson, 1993).

Although basic REE models generally support an origin by fractional crystallization, in reality REE variations during magmatic evolution are more complex, and difficult to model accurately. Many variables such as changes in crystallizing phases and changes in partition coefficients (D_{REE}) with magma evolution can greatly affect the final melt composition. To address this, Brophy (2008) incorporated changes in D_{REE} with SiO$_2$ into mass-balance models to discriminate between amphibolite melting and crystal fractionation processes. Brophy (2008) found that regardless of the type of melting (equilibrium, fractional or accumulated fractional), partial melting of either intermediate or mafic amphibolite should yield REE abundances that remain constant, and then decrease with increasing liquid SiO$_2$. At high SiO$_2$ values (>63 wt %), LREE abundances should range from slightly enriched to depleted (i.e. ~2–0·2 times those of source values), whereas

Table 4: Least-squares fractional crystallization modelling of the Kermadec magmas

Raoul mass-balance model	Parent (MB02)	Daughter (GLP)	Calculation	Difference	SSE	R^2	F/C %
SiO_2	49·77	69·56	69·56	<0·01	<0·01	1·00	−75·04
TiO_2	0·61	0·60	0·60	<0·01			
Al_2O_3	17·60	14·14	14·14	<0·01			
Fe_2O_3*	11·51	5·28	5·28	<0·01			
MgO	6·63	1·14	1·14	<0·01			
CaO	12·08	4·72	4·72	<0·01			
Na_2O	1·63	3·94	3·94	<0·01			
K_2O	0·16	0·62	0·62	<0·01			

Crystal comp.	Ol (Fo_{82})	Ol (Fo_{72})	OPX	CPX (Mg_{85})	Mag (Mnt_{85})	Plag An_{80}	Plag An_{95}
SiO_2	38·53	36·34	51·17	52·93	0·10	47·58	43·63
TiO_2			0·29	0·13	5·35		
Al_2O_3			2·99	2·14	5·05	32·98	35·48
Fe_2O_3*	18·22	27·50	18·62	5·80	86·39	0·61	0·77
MgO	43·08	35·99	25·17	17·45	3·11	0·06	0·10
CaO	0·18	0·16	1·76	21·45		16·54	19·63
Na_2O			0·01	0·10		2·21	0·38
K_2O						0·02	0·01
% crystallized	−0·11	−2·93	−6·89	−18·61	−7·82	−26·40	−12·28
sum 100%	0·15	3·90	9·18	24·80	10·42	35·19	16·37

Macauley mass-balance model	Parent (45656)	Daughter (SBT)	Calculation	Difference	SSE	R^2	F/C %
SiO_2	49·42	70·85	70·85	<0·01	0·08	1·00	−70·81
TiO_2	0·73	0·64	0·35	0·28			
Al_2O_3	17·07	13·32	13·31	0·01			
Fe_2O_3*	11·36	5·01	5·03	−0·03			
MgO	6·58	0·82	0·79	0·02			
CaO	12·73	3·17	3·19	−0·01			
Na_2O	1·71	4·53	4·54	−0·02			
K_2O	0·40	1·66	1·62	0·05			

Crystal comp.	CPX (Mg_{82})	Plag An_{93}	Mag (Mnt_{71})	Plag An_{65}	Ol (Fo_{73})	OPX
SiO_2	50·70	44·23	0·09	51·33	36·11	51·33
TiO_2	0·31	0·00	7·86	0·05		0·61
Al_2O_3	4·12	34·93	2·48	30·66		1·21
Fe_2O_3*	6·68	0·97	87·29	0·67	29·35	23·62
MgO	15·79	0·08	2·27	0·05	34·36	21·57
CaO	22·27	19·00		13·34	0·18	1·64
Na_2O	0·14	0·78		3·82		0·01
K_2O		0·01		0·08		
% crystallized	−26·97	−21·94	−8·65	−6·50	−6·29	−0·46
sum 100%	38·09	30·98	12·22	9·17	8·89	0·65

(continued)

Table 4: Continued

Healy mass-balance model	Parent (X594C)	Daughter (D38 glass)	Calculation	Difference	SSE	R^2	F/C %
SiO_2	49·83	76·22	76·22	0·00	<0·01	1·00	–81·87
TiO_2	0·99	0·31	0·23	0·08			
Al_2O_3	16·72	13·31	13·31	0·00			
Fe_2O_3*	12·99	2·10	2·11	–0·01			
MgO	5·41	0·38	0·37	0·01			
CaO	11·60	1·93	1·94	0·00			
Na_2O	2·12	3·96	3·96	0·00			
K_2O	0·34	1·79	1·79	0·00			

Crystal comp.	CPX	Plag	Mag	Plag	Ol	OPX
	(Mg_{78})	An_{95}	(Mnt_{76})	An_{66}	(Fo_{73})	
SiO_2	51·07	44·04	0·05	51·51	36·93	52·06
TiO_2	0·30		7·93	0·03		0·34
Al_2O_3	3·53	35·25	1·78	30·54		1·40
Fe_2O_3*	6·55	0·80	88·65	0·79	26·28	19·91
MgO	15·87	0·05	1·60	0·04	36·67	24·76
CaO	22·51	19·32		13·36	0·12	1·52
Na_2O	0·17	0·52		3·69		0·00
K_2O		0·01		0·05		
% crystallized	–22·80	–6·33	–10·79	–36·01	–0·51	–5·44
sum 100%	27·84	7·73	13·18	43·98	0·62	6·64

Mass-balancing calculations made using OPTIMASBA Microsoft® Excel© workbook from Cabero *et al*. (2012). SSE, sum of squares owing to error. F/C %, total amount of crystallization from the original melt. Daughter used for Raoul is sample RI18__PO5 from the Green Lake pumice. SBT, Sandy Bay Tephra (MI07__PO3). Parent melt for Macauley is a basaltic lava from Macauley Island from Smith *et al*. (2003*a*). Parent melt from Healy is a basalt analysed by Wright & Gamble (1999). CPX, clinopyroxene; OPX, orthopyroxene; Ol, olivine; Plag, plagioclase; Mag, magnetite.

HREE abundances should be slightly depleted (i.e. ~1–0·2 times those of source values). To test this hypothesis, La (LREE) and Yb (HREE) concentrations have been plotted against SiO_2 for samples analysed from both this and previous studies on the same Kermadec volcanoes (Fig. 18). None of the samples show indications that they formed through amphibolite melting (either mafic or intermediate in composition). Instead, they show significant increases in REE concentrations with increasing SiO_2. For Raoul and Raoul SW, increases in La and Yb are similar, between two and four times the concentration observed in the mafic blebs (Fig. 18), consistent with REE variations generated by upper-crustal hornblende-absent basalt fractionation (Brophy, 2008). For Macauley (excepting one outlier sample) and Healy, La is strongly enriched in the high SiO_2 samples by ~3–4 times, whereas Yb is only slightly enriched by ~2–3 times (Fig. 18), consistent with mid- to upper-crustal hornblende-bearing basalt fractionation. In addition, there is an apparent inconsistency between the REE data presented by Smith *et al.* (2003*a*, 2003*b*, 2006, 2010) and our data from the same eruption units, which show generally 20–30% higher REE concentrations for the Raoul and Macauley pumices (Fig. 18). However, the data presented for Raoul volcano by Smith *et al.* (2010) still show an overall positive trend in REE concentration with increasing SiO_2, especially for Yb. Furthermore, the raw data presented in the online appendices of the studies by Worthington (1998) and Smith *et al.* (2010) do not seem to match with data presented in fig. 13 of Smith *et al.* (2010). When replotted, the raw data of Smith *et al.* (2010) are not consistent with amphibolite melting, but instead suggest that fractional crystallization is the dominant process of melt differentiation at Raoul (Brophy, 2008; Fig. 18).

Fractional crystallization: potential problems?

Many studies have suggested that fractional crystallization alone cannot explain the chemical diversity of silicic magmas in intra-oceanic arcs when compared with contemporaneous basaltic or andesitic magmas (e.g. Tamura & Tatsumi, 2002; Leat *et al.*, 2003; Smith *et al.*, 2003*a*, 2003*b*, 2006, 2010; Vogel *et al.*, 2004; Shukuno *et al.*, 2006; Tamura *et al.*, 2009). Several lines of evidence have been proposed against fractional crystallization, which we address below.

1. *Large silicic eruption volumes*. The large volumes of silicic magma erupted have been proposed as a major argument against fractional crystallization both in the Kermadec arc (Smith *et al.*, 2003*a*, 2003*b*) and other oceanic arc settings (e.g. Leat *et al.*, 2003). In part this objection is, however, based on large estimates of eruption sizes (e.g. Latter *et al.*, 1992). Many of the constraints involved in these arguments are based on assumptions that fractional crystallization would require high degrees of crystallization, and that such prolonged fractionation would generate small melt volumes that contain a complexly zoned phenocryst assemblage. Several studies have shown that large silicic magma volumes can be generated by fractional crystallization, and erupted in large volumes (e.g. Baker *et al.*, 2000; Ukstins-Peate *et al.*, 2008). Current understanding of magma crystallization (e.g. Marsh, 1988, 1996; Vigneresse *et al.*, 1996) and of silicic magma reservoir structure (e.g. Hildreth & Wilson, 2007; Bachmann & Bergantz, 2008) suggests that large volumes of crystal-poor magma can be rapidly and effectively extracted from crystal mush zones (Bachmann & Bergantz, 2004; Hildreth, 2004; Wilson *et al.*, 2006; Lipman, 2007; Girard & Stix, 2009; Wilson & Charlier, 2009). These models may also be applicable to the Kermadec magmatic systems, as this study, combined with previous work on melt inclusions from Healy pumices (Saunders *et al.*, 2010), has shown evidence for extensive fractional crystallization in the generation of the silicic magmas. Although the amount of magma released in each eruption is poorly constrained, estimates of the volume of parental melt required to generate the range of silicic eruptive volumes can be made. The volume of parental melts required for ~70–80% fractional crystallization is ~2·5–5 times larger than the volume of silicic magma erupted. Modest eruption sizes of 1–2 km^3 would thus require a minimum of 2·5–10 km^3 of crystallizing parental melt, a more reasonable volume given the large total volume of the Kermadec volcanoes (e.g. Raoul > 200 km^3; Smith *et al.*, 2006) and the significant volumes of basalt erupted in recent cone-building episodes at Raoul and Macauley. Large volumes of partially to highly crystalline mush can hold extractable melt for long time periods (e.g. Bachmann & Bergantz, 2004), especially if the magma reservoir is primed and heated from newly arriving melts.
2. *The crystal-poor nature of the pumices*. This cannot rule out a fractional crystallization origin of the magmas as crystal–melt segregation in silicic systems depends on many contributing processes (see Bachmann & Bergantz, 2004, for review). As observed in continental volcanoes, silicic magmas erupted from mush-dominated magma reservoirs range from highly crystalline (up to 50 vol. % crystals; Bachmann *et al.*, 2002) to almost aphyric (e.g. Hildreth, 2004).
3. *Variations in magma chemistry over time*. Smith *et al.* (2003*a*, 2003*b*, 2006, 2010) used major element modelling to propose that the silicic magma batches from Raoul could not be related or derived from a common parent unless the composition of the extracted assemblage varied for each batch. As shown here, however, much of the perceived variation between these magma batches is caused by differing degrees of mixing or assimilation from multiple sources. We suggest that the Raoul magmas were held in an open magma chamber, exposed to mass and chemical exchange not only with progenitor mafic bodies, but also with hydrothermally altered felsic plutonic material.
4. *Bimodal erupted compositions*. Like other oceanic arc systems (e.g. Izu–Bonin: Tamura & Tatsumi, 2002; South Sandwich: Leat *et al.*, 2003) the Kermadec arc has erupted a bimodal whole-rock compositional distribution (Wright *et al.*, 2006). This is also evident in the composition of minerals within the pumice samples. Similar observations, however, apply across a broad range of magmatic settings (e.g. Daly, 1925; Baker, 1968; Reubi & Blundy, 2009), and are not a unique feature of Kermadec volcanoes, and hence cannot be used to discount fractional crystallization as the dominant differentiation process. In addition, experimental studies have shown that large compositional changes over small temperature intervals significantly reduce the likelihood of extracting andesite liquid compositions (Reubi & Blundy, 2009).
5. *The abrupt change from basalt to dacite*. At both Raoul and Macauley, the record of subaerial volcanism was used to suggest that prior to ~4 and 7 ka, respectively, basalt and basaltic-andesite were the dominant magmas erupted at each volcano (Brothers & Searle, 1970; Ewart *et al.*, 1977; Lloyd & Nathan, 1981; Lloyd *et al.*, 1996; Smith *et al.*, 2003*a*, 2003*b*, 2006). The presence of 1·25 Ma tonalite lithic fragments in the

'earliest' (Matatirohia) silicic deposits on Raoul and granitoid lithic fragments in the Sandy Bay tephra on Macauley demonstrates that silicic magmatism has persisted over long time periods, whether or not accompanied by surviving volcanic deposits. The record from sediment cores offshore from Raoul and Macauley also shows that multiple silicic eruptions have occurred in the Pleistocene (Shane & Wright, 2011).

(6) *Sr variations with plagioclase crystallization*. Trace element variations form a subparallel pattern between basalt and dacite or rhyolite at each of the Kermadec volcanoes on multi-element and REE plots (Figs 6 and 17). The trace elements that are an exception to this are Eu, Ti and Sr. As Eu and Ti depletions are the effects of plagioclase and magnetite fractionation respectively, these differences would be expected with magma evolution. However, the lack of Sr depletion in evolved magmas has previously been used as evidence against crystal fractionation at Raoul and Macauley volcanoes, as Sr is compatible in plagioclase (Smith *et al.*, 2003*a*, 2006). Sr partitioning into plagioclase, however, is highly dependent on the anorthite content of the plagioclase and therefore on changes in temperature, pressure, melt composition and water content (Blundy & Wood, 1991; Bédard, 2006; Smith *et al.*, 2009). In general, D_{Sr} in plagioclase increases with decreasing anorthite content (Blundy & Wood, 1991), evident in Sr variability in plagioclase of differing anorthite content from the Kermadec volcanoes (Fig. 10). The lack of Sr depletion in the silicic magmas could thus be interpreted to reflect plagioclase crystallization acting in concert with changing Sr partitioning with melt composition. All pumices in this study have negative Eu-anomalies, indicating that plagioclase has fractionated. In addition, many plagioclase crystals in the silicic melts are xenocrysts assimilated from less evolved melts, indicating that the evolved magma is open to chemical and mass exchange.

Inferred magmatic systems of the Kermadec volcanoes

This study demonstrates that fractional crystallization is the dominant process for the generation of silicic magmas at four Kermadec arc volcanoes, and that the basaltic and silicic magmas and previously crystallized plutons are closely related. It is envisaged that ascending basaltic magmas stall and form partially to wholly crystalline plutonic bodies, which subsequently differentiate to form silicic magmas. This concept is supported by the presence of gabbroic plutonic xenoliths on Raoul and Macauley Islands, as well as mafic-derived crystals mixed into many Kermadec pumices. Because of the strong genetic links between the mafic and silicic magmas, it is interpreted that mafic crystals previously termed xenocrysts might be better termed 'antecrysts' (Hildreth, 2004; Charlier *et al.*, 2005; Jerram & Martin, 2008), as they crystallized in the progenitor melts from which the silicic magmas fractionated.

The crystal mush model has been widely applied to continental volcanoes to explain the rapid generation and accumulation of large amounts of eruptible silicic magma (Bachmann & Bergantz, 2004; Hildreth, 2004; Wilson *et al.*, 2006; Hildreth & Wilson, 2007; Girard & Stix, 2009). We suggest that the crystal mush model may help explain many features of the Kermadec silicic magmas. The crystal mush model does not in itself favour crustal melting or fractional crystallization as the dominant process, as the 50–60 vol. % crystal window can be achieved by either mechanism. However, thermodynamic models of heat and mass transfer within the crust (Barboza *et al.*, 1999; Babeyko *et al.*, 2002; Dufek & Bergantz, 2005; Annen *et al.*, 2006) and field observations in exposed crustal sections (Barboza & Bergantz, 2000; Greene *et al.*, 2006; Hacker *et al.*, 2008) suggest that fractional crystallization occurring synchronously with some assimilation is the dominant differentiation process in most tectonic settings (Bachmann & Bergantz, 2008).

A schematic illustration (Fig. 19) highlights the role crystallization of previously emplaced basaltic magmas plays in the generation of silicic magmas, using Raoul volcano as a type example. The magma reservoir can be defined by four main zones, as follows.

Zone (1), stalled basaltic magma. Rising mantle-derived melts stall within the mid- to lower crust and crystallize, providing heat and new material to the overlying mush column (Marsh, 1988, 1996). The depth and extent of this zone is poorly constrained, and could vary significantly, possibly as far down as the base of the crust (~15 km). Although there is no evidence for large-scale exchange of melt into the evolved silicic magmas, some high-Mg clinopyroxene antecrysts in the dacite show evidence for resorption in primitive (high-Cr and -Ni) magmas (e.g. Fig. 8b). This suggests that primitive melts can make their way into the mush column and interact with more-evolved crystals. This process is considered to be likely given that newly arriving liquid basalts would have a lower density than the gabbroic cumulates that make up the base of the mush column. This also suggests that newly arriving primitive magmas could induce some partial melting in some parts of the overlying cumulate mush column. These findings differ from those of Smith *et al.* (2010), who suggested that the crystal reservoir formed from magma more primitive than the evolved magmas that ascended into it.

Zone (2), crystal-rich cumulate mush column. Crystallizing basalts form a zone of partly to wholly crystalline crystal

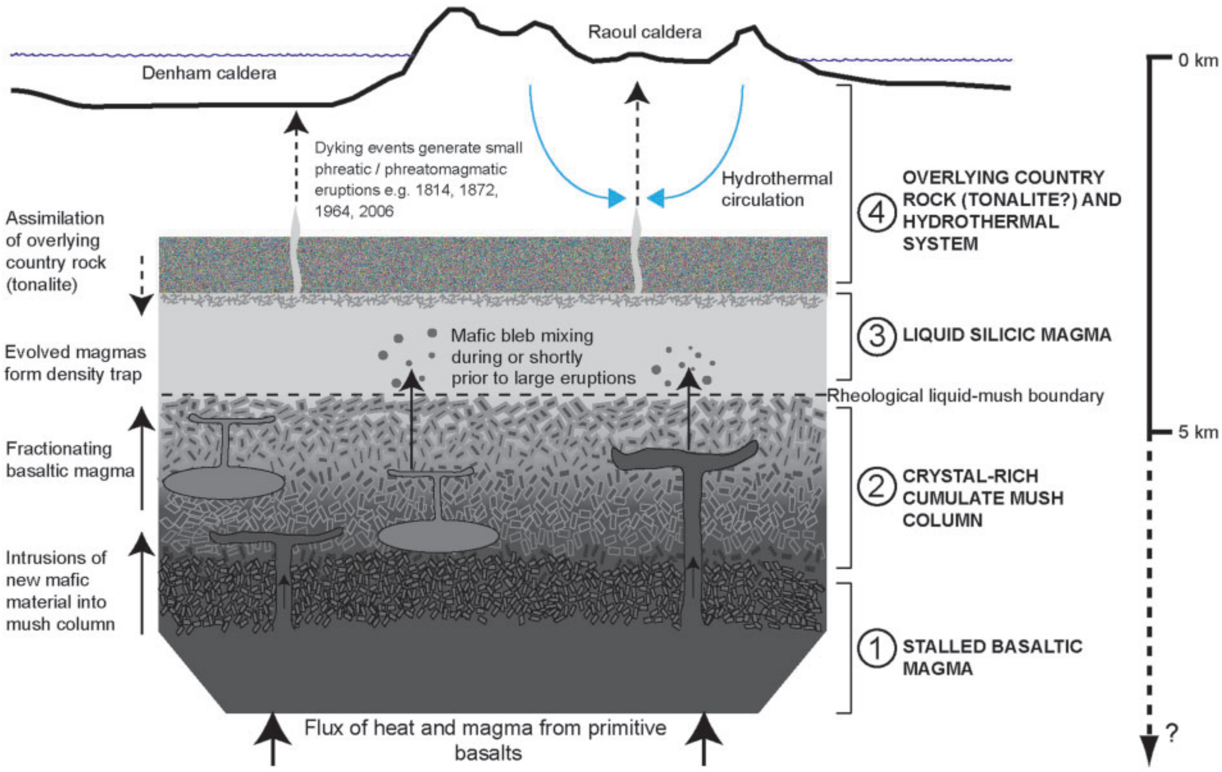

Fig. 19. Schematic illustration of the structure of the magmatic system below Raoul volcano. (See text for details.) Depth of the magma chamber is constrained by amphibole barometry; other dimensions are schematic. Depths of the zones 1 and 2 are unknown, as indicated by the dashed depth scale. The depth of hydrothermal circulation is from Graaf (2006).

mush [compare the partly molten dykes and sills extending vertically through the crust proposed by Smith *et al.* (2010)]. Crystallization may be induced by stalling or by decompression-induced H_2O exsolution (Brophy, 2009). The mush column behaves as a rheological solid, and chunks can be disaggregated and transported by the intruding magma. The crystals that make up a large part of the mush column include high-An plagioclase as well as clinopyroxene and olivine with high Mg numbers (>70–85). Many of these crystals are eventually erupted in the more evolved basalts and basaltic-andesites (Smith *et al.*, 2006, 2010), as well as dacites. It is inferred that the upper part of the mush column is more evolved, and largely crystalline (>55 vol. % crystals). This part of the mush column acts as a rigid sponge, from which eruptible silicic melt can be readily extracted into the overlying silicic melt-dominant body.

Zone (3), silicic melt dominant body. The dacite magma is hot (~900–1000°C for Raoul; Table 3) and crystal poor. As many crystals observed in the pumices are grouped into clots, crystallization may predominantly occur on the chamber walls and/or roof (Marsh, 1988). The exact size and shape of the silicic magma chamber is unknown, although because of the sizes of the Raoul and Denham calderas and the inferred magma volumes erupted, it is likely to have had a sill-like form. Whether this is a continuous body that encompasses both calderas is uncertain. However, as activity was observed from Denham Bay during eruptions from Raoul caldera (e.g. 1814, 1872 and 1964; Lloyd & Nathan, 1981), it is inferred that they have some close connection. Several studies have suggested that basaltic magma mixing can be a triggering mechanism for silicic eruptions (e.g. Pallister *et al.*, 1992; Leonard *et al.*, 2002; Wilson *et al.*, 2006). This may be the case for the Raoul eruptions, as unzoned olivine crystals indicate that magma mixing occurred very shortly before eruption. As some crystals in mafic blebs have been resorbed in primitive basalts (indicated by clinopyroxene zones with high Cr and Ni), they may be sourced from deeper in the mush column. This also suggests that influx of new primitive magma into the deeper reservoir may disrupt the overlying crystal mush, and possibly the silicic melt dominant body. Another possibility is that the eruption of silicic magma acted as a trigger for magma mixing, and largely crystalline basalt at the base of the silicic magma chamber was overturned during eruption and decompression (Woods & Cowan, 2009). Regardless of mixing mechanisms, the rounded cauliform appearance and internal textures of the mafic blebs indicate that they were partially molten when incorporated into the dacite magma. This also highlights how the formation of a silicic magma chamber(s) has affected the entire magmatic system. Owing to the density contrast between basaltic and silicic melts, rising basalts are not able to penetrate in quantity through the more evolved magmas (e.g. Geist *et al*., 1995), which may explain the change from basaltic to dacitic volcanism at Raoul during the last ~4000 years.

Zone (4), overlying country rock and hydrothermal system. The region above the silicic magma chamber plays an important role in the Raoul magmatic system. This study has shown that low-An plagioclase, probably from a shallow tonalite source, was assimilated into the dacite magmas. The tonalites are hydrothermally altered and are therefore likely to have been sourced from a region in close proximity to both silicic magmas and the hydrothermal system at Raoul (estimated at ~2–3 km depth from hydrothermal water chemistry; Graaf, 2006). As tonalite xenocrysts are assimilated only in younger eruptions from Raoul, it is possible that the silicic magma chamber may have shifted to shallower levels with time, even as eruption volumes have decreased. More recently, historical activity at Raoul has consisted of small phreatic or phreatomagmatic eruptions in 1814, 1872, 1964 and 2006, which may be caused by the intrusion of dikes into the hydrothermal system (Graaf, 2006).

The proposed magmatic system model for Raoul (Fig. 19) could also apply to Raoul SW, Macauley and Healy, as samples from these volcanoes share many of the features observed in Raoul pumices (e.g. mafic blebs, mafic crystals, crystal clusters). For Healy and Raoul SW, crystallization may play a larger role in the silicic magma chamber, as pumices contain large clots of clustered crystals of more evolved or hydrous compositions (e.g. amphibole and quartz). Many of the Healy crystals are not in equilibrium with their host glasses, indicating that there may be further crystal–melt segregation in the Healy silicic magma chamber(s). However, the lack of stratigraphic control on submarine dredge samples (Barker *et al*., 2012) and poor constraints on eruptive histories restrict further speculation for these volcanoes.

CONCLUSIONS

A detailed investigation of the compositional variations and mineralogical diversity in pumice samples from four Kermadec arc volcanoes has shown the following.

(1) Samples from Raoul have a relatively restricted whole-rock compositional range. Samples dredged from around Macauley caldera fall into several different compositional groups, demonstrating that the products sampled by dredging are from multiple eruptions and/or magma systems. In contrast, samples dredged from Healy and Raoul SW have restricted compositions. Subtle whole-rock compositional variations can be explained by magma mixing with variable amounts of crystal cargoes.

(2) Pumice samples from all volcanoes have a diverse crystal assemblage with multiple populations, many of which show evidence for complex magmatic histories. Although some crystals are in equilibrium with their host glasses many are not, with compositions that are more consistent with a mafic source. Hydrothermally altered plagioclase and quartz are also found in some Raoul pumices. Magma mixing and/or minor assimilation plays an important role in the Kermadec magmatic systems, as evident from the crystal assemblages and from inclusions of discrete mafic blebs. The origin of mixed crystals and melts at Raoul and Macauley is consistent with two sources as reflected in co-eruptive plutonic xenoliths: hydrothermally altered tonalite and cumulate olivine gabbros. The tonalite, through comparison with petrographically similar material dated at ~1·25 Ma (Mortimer *et al*., 2010), is inferred to represent earlier silicic magmatism at Raoul.

(3) At all four volcanoes, pumice trace element patterns are subparallel to those of basalts and whole mafic blebs extracted from within pumices. In addition, samples from single volcanoes show limited ranges in Pb and Sr isotopic compositions. Major and trace element compositions of the Kermadec silicic magmas can be modelled by 70–80% fractional crystallization of a basaltic parent. Variations of LREE/HREE ratios with SiO_2 are consistent with mid- to upper-crustal hornblende-absent basalt fractionation for Raoul and Raoul SW, and mid- to upper-crustal hornblende-bearing basalt fractionation for Macauley and Healy. Trace element patterns, mineral O-isotope compositions, major and trace element modelling, and considerations of thermal limitations suggest that fractional crystallization is the dominant process for generating silicic magmas, and not crustal anatexis as previously suggested.

(4) The magmatic systems of the Kermadec volcanoes can be envisaged as a column of crystallizing basalt forming a large cumulate mush zone from which more evolved magmas form. This mush column is recharged with heat and material from newly arriving primitive melts. Owing to large density contrasts, the rising basalts are not able to rise through the more evolved magmas. The silicic magma chamber is open to mixing of material from progenitor melts and overlying country rock, as recorded in pumice mineral assemblages.

ACKNOWLEDGEMENTS

We thank the Masters and crew members of the R.V. *Tangaroa* on the NZAPLUME III (2004) and TAN07/06

(2007) voyages for their logistical support, and Cornel de Ronde for giving C.J.N.W. the opportunity to first visit Raoul in 2004. The New Zealand Department of Conservation gave permission for the island field-work, and we especially acknowledge Karen Baird and Raoul Conservancy staff in 2004 and 2007 for their hospitality and field support. Max Borella, Darren Gravley and Mike Rosenberg helped with field studies in 2007, and John Watson is thanked for XRF analyses. Andy Phillips and Jannine Cooper provided much-appreciated guidance and assistance with oxygen isotope analyses. Andrew Rae provided help with bathymetric maps and GIS software. Monica Handler, Ian Smith and John Gamble provided helpful discussions. We would like to thank Jim Brophy, Jennifer Garrison and Bob Stewart for their helpful reviews of this paper, and Richard Price for editorial assistance.

FUNDING

Support from the Marsden Fund of the Royal Society of New Zealand (VUW0613) and the New Zealand Foundation for Research, Science and Technology (contract C01X0702-RJW) is acknowledged, as well as a Victoria University of Wellington Strategic Research Grant awarded to S.J.B.

SUPPLEMENTARY DATA

Supplementary data for this paper are available at *Journal of Petrology* online.

REFERENCES

Allan, A. S. R., Baker, J. A., Carter, L. & Wysoczanski, R. J. (2008). Reconstructing the Quaternary evolution of the world's most active silicic volcanic system: insights from an ∼1·65 Ma deep ocean tephra record sourced from Taupo Volcanic Zone, New Zealand. *Quaternary Science Reviews* **27**, 2341–2360.

Annen, C., Blundy, J. D. & Sparks, R. S. J. (2006). The genesis of intermediate and silicic magmas in deep crustal hot zones. *Journal of Petrology* **47**, 505–539.

Arculus, R. J. (2003). Use and abuse of the terms calcalkaline and calcalkalic. *Journal of Petrology* **44**, 929–935.

Babeyko, A. Y., Sobolev, S. V., Trumbull, R. B., Oncken, O. & Lavier, L. L. (2002). Numerical models of crustal scale convection and partial melting beneath the Altiplano–Puna Plateau. *Earth and Planetary Science Letters* **199**, 373–388.

Bach, W., Hegner, E. & Erzinger, J. (1998). Chemical fluxes in the Tonga subduction zone: Evidence from the southern Lau Basin. *Geophysical Research Letters* **25**, 1467–1470.

Bachmann, O. & Bergantz, G. W. (2004). On the origin of crystal-poor rhyolites: extracted from batholithic crystal mushes. *Journal of Petrology* **45**, 1565–1582.

Bachmann, O. & Bergantz, G. W. (2008). Rhyolites and their source mushes across tectonic settings. *Journal of Petrology* **49**, 2277–2285.

Bachmann, O., Dungan, M. A. & Lipman, P. W. (2002). The Fish Canyon magma body, San Juan volcanic field, Colorado: rejuvenation and eruption of an upper crustal batholith. *Journal of Petrology* **43**, 1469–1503.

Bacon, C. R. & Hirschmann, M. M. (1988). Mg/Mn partitioning as a test for equilibrium between coexisting Fe–Ti oxides. *American Mineralogist* **73**, 57–61.

Baker, I. (1968). Intermediate oceanic volcanic rocks and the 'Daly Gap'. *Earth and Planetary Science Letters* **4**, 103–106.

Baker, J. A., MacPherson, C. G., Menzies, M. A., Thirlwall, M. F., Al-Kadasi, M. & Mattey, D. P. (2000). Resolving crustal and mantle contributions to continental flood volcanism, Yemen; Constraints from mineral oxygen isotope data. *Journal of Petrology* **41**, 1805–1820.

Baker, J. A., Peate, D., Waight, T. & Meyzen, C. (2004). Pb isotopic analysis of standards and samples using a ^{207}Pb–^{204}Pb double spike and thallium to correct for mass bias with a double focusing MC-ICPMS. *Chemical Geology* **211**, 275–303.

Barboza, S. A. & Bergantz, G. W. (2000). Metamorphism and anatexis in the mafic complex contact aureole, Ivrea Zone, northern Italy. *Journal of Petrology* **41**, 1307–1327.

Barboza, S. A., Bergantz, G. W. & Brown, M. (1999). Regional granulite facies metamorphism in the Ivrea zone: Is the Mafic Complex the smoking gun or a red herring? *Geology* **27**, 447–450.

Barker, S., Rotella, M. D., Wilson, C. J. N., Wright, I. C. & Wysoczanski, R. J. (2012). Contrasting pyroclast density spectra from subaerial and submarine silicic eruptions in the Kermadec arc: implications for eruptive processes and dredge sampling. *Bulletin of Volcanology* **74**, 1425–1443.

Bédard, J. H. (2006). Trace element partitioning in plagioclase feldspar. *Geochimica et Cosmochimica Acta* **70**, 3717–3742.

Berlo, K., Blundy, J. D., Turner, S. P. & Hawkesworth, C. J. (2007). Textural and chemical variation in plagioclase phenocrysts from the 1980 eruptions of Mount St. Helens, USA. *Contributions to Mineralogy and Petrology* **154**, 291–308.

Bindeman, I. N. (2008). Oxygen isotopes in mantle and crustal magmas as revealed by single crystal analysis. In: Putirka, K. D. & Tepley, F. J., III (eds) *Minerals, Inclusions and Volcanic Processes. Mineralogical Society of America and Geochemical Society, Reviews in Mineralogy and Geochemistry* **69**, 445–473.

Blundy, J. & Cashman, K. V. (2008). Petrologic reconstruction of magmatic system variables and processes. In: Putirka, K. D. & Tepley, F. J., III (eds) *Minerals, Inclusions and Volcanic Processes. Mineralogical Society of America and Geochemical Society, Reviews in Mineralogy and Geochemistry* **69**, 179–231.

Blundy, J. D. & Wood, B. J. (1991). Crystal-chemical controls on the partitioning of Sr and Ba between plagioclase feldspar, silicate melts, and hydrothermal solutions. *Geochimica et Cosmochimica Acta* **55**, 193–209.

Bowen, N. L. (1913). The melting phenomena of the plagioclase feldspars. *American Journal of Science, Series 4* **35**, 577–599.

Brey, G. P. & Kohler, T. (1990). Geothermobarometry in four-phase lherzolites 2. New thermobarometers, and practical assessment of existing thermobarometers. *Journal of Petrology* **31**, 1353–1378.

Brophy, J. G. (2008). A study of rare earth element (REE)–SiO_2 variations in felsic liquids generated by basalt fractionation and amphibole melting: a potential test for discriminating between the two different processes. *Contributions to Mineralogy and Petrology* **156**, 337–357.

Brophy, J. G. (2009). Decompression and H_2O exsolution driven crystallization and fractionation: development of a new model for low-pressure fractional crystallization in calc-alkaline magmatic systems. *Contributions to Mineralogy and Petrology* **157**, 797–811.

Brophy, J. G., Ota, T., Kunihro, T., Tsujimori, T. & Nakamura, E. (2011). *In situ* ion-microprobe determinations of trace element partition coefficients for hornblende, plagioclase, orthopyroxene, and apatite in equilibrium with natural rhyolitic glass, Little Glass Mountain Rhyolite, California. *American Mineralogist* **96**, 1838–1850.

Brothers, R. N. & Martin, K. R. (1970). The geology of Macauley Island, Kermadec Group, Southwest Pacific. *Bulletin Volcanologique* **34**, 330–346.

Brothers, R. N. & Searle, E. J. (1970). The geology of Raoul Island, Kermadec Group, Southwest Pacific. *Bulletin Volcanologique* **34**, 7–37.

Cabero, M. T., Mecoleta, S. & López-Moro, F. J. (2012). OPTIMASBA: A Microsoft Excel workbook to optimise the mass-balance modelling applied to magmatic differentiation processes and subsolidus overprints. *Computers and Geosciences* **42**, 206–211.

Carter, R. M., Carter, L. & McCave, I. N. (1996). Current controlled sediment deposition from the shelf to deep ocean: the Cenozoic evolution of circulation through the SW Pacific gateway. *Geologische Rundschau* **85**, 438–451.

Charlier, B. L. A., Wilson, C. J. N., Lowenstern, J. B., Blake, S., van Calsteren, P. W. & Davidson, J. P. (2005). Magma generation at a large, hyperactive silicic volcano (Taupo, New Zealand) revealed by U–Th and U–Pb systematics in zircons. *Journal of Petrology* **46**, 3–32.

Coombs, M. L. & Gardner, J. E. (2004). Reaction rim growth on olivine in silicic melts: implications for magma mixing. *American Mineralogist* **89**, 748–759.

Daly, R. A. (1925). The geology of Ascension Island. *Proceedings of the American Academy of Arts and Sciences* **60**, 1–80.

Deering, C. D., Vogel, T. A., Patino, L. C. & Alvarado, G. E. (2007). Origin of distinct silicic magma types from the Guachipelím Caldera, NW Costa Rica: evidence for magma mixing and protracted subvolcanic residence. *Journal of Volcanology and Geothermal Research* **165**, 103–126.

DeMets, C., Gordon, R. G., Argus, D. F. & Stein, S. (1994). Effect of recent revisions to the geomagnetic reversal time scale on estimates of current plate motions. *Geophysical Research Letters* **21**, 2191–2194.

Devine, J. D. (1995). Petrogenesis of the basalt–andesite–dacite association of the Grenada, Lesser Antilles island arc, revisited. *Journal of Volcanology and Geothermal Research* **69**, 1–33.

Dufek, J. & Bergantz, G. W. (2005). Lower crustal magma genesis and preservation: a stochastic framework for the evaluation of basalt–crust interaction. *Journal of Petrology* **46**, 2167–2195.

Eiler, J. M. (2001). Oxygen Isotope Variations of Basaltic Lavas and Upper Mantle Rocks. In: Valley, J. W. & Cole, D. R. (eds) *Stable isotope geochemistry. Mineralogical Society of America and Geochemical Society, Reviews in Mineralogy and Geochemistry* **43**, 319–364.

Eiler, J. M., Crawford, A., Elliot, T., Farley, K. A., Valley, J. W. & Stopler, E. M. (2000). Oxygen isotope geochemistry of oceanic arc lavas. *Journal of Petrology* **41**, 229–256.

Ewart, A. & Hawkesworth, C. J. (1987). The Pleistocene–Recent and Tonga–Kermadec arc lavas: Interpretations of new isotopic and rare earth data in terms of a depleted mantle source model. *Journal of Petrology* **28**, 495–530.

Ewart, A., Brothers, R. N. & Mateen, A. (1977). An outline of the geology and geochemistry, and the possible petrogenetic evolution of the volcanic rocks of the Tonga–Kermadec–New Zealand island arc. *Journal of Volcanology and Geothermal Research* **2**, 205–250.

Ewart, A., Collerson, K. D., Regelous, M., Wendt, J. I. & Niu, Y. (1998). Geochemical evolution within the Tonga–Kermadec–Lau arc–back-arc systems: the role of varying mantle wedge composition in space and time. *Journal of Petrology* **39**, 331–368.

Gamble, J. A., Wright, I. C. & Baker, J. A. (1993). Seafloor geology and petrology in the oceanic to continental transition zone of the Kermadec–Havre–Taupo Volcanic Zone arc system, New Zealand. *New Zealand Journal of Geology and Geophysics* **36**, 417–435.

Gamble, J. A., Woodhead, J. D., Wright, I. C. & Smith, I. E. M. (1996). Basalt and sediment geochemistry and magma petrogenesis in a transect from oceanic island arc to rifted continental margin arc: the Kermadec–Hikurangi margin, SW Pacific. *Journal of Petrology* **37**, 1523–1546.

Gamble, J. A., Christie, R. H. K., Wright, I. C. & Wysoczanski, R. J. (1997). Primitive K-rich magmas from Clark Volcano, southern Kermadec arc: A paradox in the K–depth relationship. *Canadian Mineralogist* **35**, 275–290.

Garrido, C. J., Bodinier, J.-L., Burg, J., Zeilinger, G., Hussain, S. S., Dawood, H., Chaudhry, M. N. & Gervilla, F. (2006). Petrogenesis of mafic garnet granulite in the lower crust of the Kohistan paleo-arc complex (Northern Pakistan): implications for intra-crustal differentiation of island arcs and generation of continental crust. *Journal of Petrology* **47**, 1873–1914.

Geist, D., Howard, K. A. & Larson, P. (1995). The generation of oceanic rhyolites by crystal fractionation: the basalt–rhyolite association at Volcan Alcedo, Galapagos Archipelago. *Journal of Petrology* **36**, 965–982.

Ghiorso, M. S. & Evans, B. W. (2008). Thermodynamics of rhombohedral oxide solid solutions and a revision of the Fe–Ti two-oxide geothermometer and oxygen barometer. *American Journal of Science* **308**, 957–1039.

Gill, J. B. (1981). *Orogenic Andesites and Plate Tectonics*. Springer: Berlin.

Girard, G. & Stix, J. (2009). Buoyant replenishment in silicic magma reservoirs: Experimental approach and implications for magma dynamics, crystal mush remobilization, and eruption. *Journal of Geophysical Research* **114**, B08203, doi:10.1029/2008JB005791.

Graaf, J. H. (2006). The hydrothermal systems of Raoul Island: past and present. MSc thesis, University of Auckland.

Graham, I. J., Reyes, A. G., Wright, I. C., Peckett, K. M., Smith, I. E. M. & Arculus, R. J. (2008). Structure and petrology of newly discovered volcanic centers in northern Kermadec – southern Tofua arc, South Pacific Ocean. *Journal of Geophysical Research* **113**, B08S02, doi:10.1029/2007JB005453.

Greene, A. R., DeBari, S. M., Kelemen, P. B., Blusztajn, J. & Clift, D. (2006). A detailed geochemical study of island arc crust: the Talkeentna Arc section, south–central Alaska. *Journal of Petrology* **47**, 1051–1093.

Grove, T. L., Elkins-Tanton, L. E., Parman, S. W., Chatterjee, N., Muntener, O. & Gaetani, G. A. (2003). Fractional crystallization and mantle-melting controls on calc-alkaline differentiation trends. *Contributions to Mineralogy and Petrology* **145**, 151–533.

Haase, K. M., Worthington, T. J., Stoffers, P., Garbe-Schonberg, D. & Wright, I. (2002). Mantle dynamics, element recycling, and magma genesis beneath the Kermadec Arc–Havre Trough. *Geochemistry, Geophysics, Geosystems* **3**, 1071, doi:10.1029/2002GC000335.

Haase, K. M., Stroncik, N., Garbe-Schonberg, D. & Stoffers, P. (2006). Formation of island arc dacite magmas by extreme crystal fractionation: An example from Brothers Seamount, Kermadec island arc (SW Pacific). *Journal of Volcanology and Geothermal Research* **152**, 316–330.

Haase, K. M., Krumm, S., Regelous, M. & Joachimski, M. (2011). Oxygen isotope evidence for the formation of silicic Kermadec island arc and Havre–Lau backarc magmas by fractional crystallization. *Earth and Planetary Science Letters* **309**, 348–355.

Hacker, B. R., Mehl, L., Kelemen, P. B., Rioux, M., Behn, M. D. & Luffi, P. (2008). Reconstruction of the Talkeetna intraoceanic arc of Alaska through thermobarometry. *Journal of Geophysical Research* **113**, B03204, doi:10.1029/2007JB005208.

Hart, S. R. (1984). A large-scale isotope anomaly in the Southern Hemisphere mantle. *Nature* **309**, 753–757.

Hildreth, W. (2004). Volcanological perspectives on Long Valley, Mammoth Mountain, and Mono Craters: several contiguous but discrete systems. *Journal of Volcanology and Geothermal Research* **136**, 169–198.

Hildreth, W. & Wilson, C. J. N. (2007). Compositional zoning of the Bishop Tuff. *Journal of Petrology* **48**, 951–999.

Jerram, D. A. & Martin, V. M. (2008). Understanding crystal populations and their significance through the magma plumbing system. In: Annen, C. & Zellmer, G. F. (eds) *Dynamics of Crustal Magma Transfer, Storage and Differentiation. Geological Society,* London, Special Publications **304**, 133–148.

Johannes, W. & Holtz, F. (1990). Formation and composition of H2O-undersaturated granitic melts. In: Ashworth, J. R. & Brown, M. (eds) *High-Temperature Metamorphism and Crustal Anatexis. Mineralogical Society Series* **2**, 87–104.

Koyaguchi, T. & Kaneko, K. (1999). A two-stage thermal evolution model of magmas in continental crust. *Journal of Petrology* **40**, 241–254.

Latter, J. H., Lloyd, E. F., Smith, I. E. M. & Nathan, S. (1992). *Volcanic hazards in the Kermadec Islands, and at submarine volcanoes between Southern Tonga and New Zealand. Ministry of Civil Defense Information Series, 4.* Ministry of Civil Defense, Wellington, 44 pp.

Leat, P. T., Smellie, J. L., Millar, I. L. & Larter, R. D. (2003). Magmatism in the South Sandwich arc. In: Larter, R. D. & Leat, P. T. (eds) *Intra-Oceanic Subduction Systems: Tectonic and Magmatic Processes. Geological Society,* London: Special Publications **219**, 285–313.

Leat, P. T., Larter, R. D. & Millar, I. L. (2007). Silicic magmas of Protector Shoal, South Sandwich Arc: indicators of generation of primitive continental crust in an island arc. *Geological Magazine* **144**, 179–190.

Le Maitre, R. W. (1989). *A Classification of Igneous Rocks and Glossary of Terms: Recommendations of the International Union of Geological Sciences, Subcommission on the Systematics of Igneous Rocks*, Blackwell: Oxford, **193**.

Lemarchand, F., Villemant, B. & Calas, G. (1987). Trace element distribution coefficients in alkaline series. *Geochimica et Cosmochimica Acta* **51**, 1071–1081.

Leonard, G. S., Cole, J. W., Nairn, I. A. & Self, S. (2002). Basalt triggering of the *c.* AD 1305 Kaharoa rhyolite eruption, Tarawera Volcanic Complex, New Zealand. *Journal of Volcanology and Geothermal Research* **115**, 461–486.

Lipman, P. W. (2007). Incremental assembly and prolonged consolidation of Cordilleran magma chambers: evidence from the Southern Rocky Mountain volcanic field. *Geosphere* **3**, 42–70.

Lloyd, E. F. & Nathan, S. (1981). *Geology and tephrochronology of Raoul Island, Kermadec Group*, New Zealand: New Zealand Geological Survey Bulletin **105**.

Lloyd, E. F., Nathan, S., Smith, I. E. M. & Stewart, R. B. (1996). Volcanic history of Macauley Island, Kermadec Ridge, New Zealand. *New Zealand Journal of Geology and Geophysics* **39**, 295–308.

Loock, G., McDonough, W. F., Goldstein, S. L. & Hofmann, A. W. (1990). Isotopic compositions of volcanic glasses from the Lau Basin. *Marine Mining* **9**, 235–245.

Marsh, B. D. (1988). Crystal size distribution (CSD) in rocks and the kinetics and dynamics of crystallization I. *Theory.* Contributions to Mineralogy and Petrology **99**, 277–291.

Marsh, B. D. (1996). Solidification fronts and magmatic evolution. *Mineralogical Magazine* **60**, 5–40.

McCoy-West, A. J., Baker, J. A., Faure, K. & Wysoczanski, R. J. (2010). Petrogenesis and origins of Mid-Cretaceous continental intraplate volcanism in Marlborough, New Zealand: implications for the long-lived HIMU magmatic mega-province of the SW Pacific. *Journal of Petrology* **51**, 2003–2045.

McKenzie, D. & O'Nions, R. K. (1991). Partial melt distributions from inversion of rare earth element concentrations. *Journal of Petrology* **32**, 1021–1091.

Millet, M.-A., Doucelance, R., Schiano, P., David, K. & Bosq, C. (2008). Mantle plume heterogeneity versus shallow-level interactions: A case study, the São Nicolau Island, Cape Verde archipelago. *Journal of Volcanology and Geothermal Research* **176**, 265–276.

Miyashiro, A. (1974). Volcanic rock series in island arcs and active continental margins. *American Journal of Science* **274**, 321–355.

Mortimer, N., Gans, P. B., Palin, J. M., Meffre, S., Herzer, R. H. & Skinner, D. N. B. (2010). Location and migration of Miocene–Quaternary volcanic arcs in the SW Pacific region. *Journal of Volcanology and Geothermal Research* **190**, 1–10.

Murphy, M. D., Sparks, R. S. J., Barclay, J., Carroll, M. R. & Brewer, T. S. (2000). Remobilization of andesite magma by intrusion of mafic magma at the Soufrière Hills volcano, Montserrat, West Indies. *Journal of Petrology* **41**, 21–42.

O'Neill, H. S. & Pownceby, M. I. (1993). Thermodynamic data from redox reactions at high temperatures 1. An experimental and theoretical assessment of the electrochemical method using stabilized zirconia electrolytes, with revised values for the Fe-"FeO", Co-CoO, Ni-NiO and Cu-Cu_2O oxygen buffers, and new data for the W-WO_2 buffer. *Contributions to Mineralogy and Petrology* **114**, 296–314.

Pallister, J. S., Hoblitt, R. P. & Reyes, A. G. (1992). A basalt trigger for the 1991 eruptions of Pinatubo volcano? *Nature* **356**, 426–428.

Palme, H. & Beer, H. (1993). Abundances of the elements in the Solar System. In: Voigt, H. H. (ed.) *Astronomy and Astrophysics, 3.* Berlin: Springer, pp. 196–221.

Paster, T. P., Schauwecker, D. S. & Haskin, L. A. (1974). The behavior of some trace elements during solidification of the Skaergaard layered series. *Geochimica et Cosmochimica Acta* **38**, 1549–1577.

Pearce, J. A. & Peate, D. W. (1995). Tectonic implications of the composition of volcanic arc magmas. *Annual Review of Earth and Planetary Sciences* **23**, 251–285.

Pearce, J. A., Baker, P. E., Harvey, P. K. & Luff, I. W. (1995). Geochemical evidence for subduction fluxes, mantle melting and fractional crystallization beneath the South Sandwich Island Arc. *Journal of Petrology* **36**, 1073–1109.

Peate, D. W., Kokfelt, T. F., Hawkesworth, C. J., van Calsteren, P., Hergt, J. M. & Pearce, J. A. (2001). U-series isotope data on Lau Basin glasses: The role of subduction-related fluids during melt generation in back-arc basins. *Journal of Petrology* **42**, 1449–1470.

Putirka, K. (2005). Igneous thermometers and barometers based on plagioclase + liquid equilibria: tests of some existing models and new calibrations. *American Mineralogist* **90**, 336–346.

Putirka, K. (2008). Thermometers and barometers for volcanic systems. In: Putirka, K. D. & Tepley, F. J., III (eds) *Minerals, Inclusions and Volcanic Processes. Mineralogical Society of America and Geochemical Society, Reviews in Mineralogy and Geochemistry* **69**, 61–111.

Putirka, K., Ryerson, F. J. & Mikaelian, H. (2003). New igneous thermobarometers for mafic and evolved lava compositions, based on clinopyroxene + liquid equilibria. *American Mineralogist* **88**, 1542–1554.

Regelous, M., Collerson, K. D., Ewart, A. & Wendt, J. I. (1997). Trace element transport rates in subduction zones: evidence from Th, Sr and Pb isotope data for Tonga–Kermadec arc lavas. *Earth and Planetary Science Letters* **150**, 291–302.

Reubi, O. & Blundy, J. (2009). A dearth of intermediate melts at subduction zone volcanoes and the petrogenesis of arc andesites. *Nature* **461**, 1269–1273.

Ridolfi, F., Renzulli, A. & Puerini, M. (2010). Stability and chemical equilibrium of amphibole in calc-alkaline magmas: an overview, new thermobarometric formulations and application to subduction-related volcanoes. *Contributions to Mineralogy and Petrology* **160**, 45–66.

Rollinson, H. (1993). *Using Geochemical Data: Evaluation, Presentation, Interpretation*. Pearson Prentice Hall: Harlow.

Saunders, K. E. (2009). Micro-analytical studies of the petrogenesis of silicic arc magmas in the Taupo Volcanic Zone and southern Kermadec Arc, New Zealand. PhD thesis, Victoria University of Wellington.

Saunders, K. E., Baker, J. A. & Wysoczanski, R. J. (2010). Microanalysis of large volume silicic magma in continental and oceanic arcs: melt inclusions in Taupo Volcanic Zone and Kermadec Arc rocks, South West Pacific. *Journal of Volcanology and Geothermal Research* **190**, 203–218.

Shane, P. & Wright, I. C. (2011). Late Quaternary tephra layers around Raoul and Macauley islands, Kermadec Arc: implications for volcanic sources, explosive volcanism and tephrochronology. *Journal of Quaternary Science* **26**, 422–432.

Sharp, Z. D. (1990). A laser-based microanalytical method for the *in situ* determination of oxygen isotope ratios of silicates and oxides. *Geochimica et Cosmochimica Acta* **54**, 1353–1357.

Shukuno, H., Tamura, Y., Tani, K., Chang, Q., Suzuki, T. & Fiske, R. S. (2006). Origin of silicic magmas and the compositional gap at Sumisu submarine caldera, Izu–Bonin arc, Japan. *Journal of Volcanology and Geothermal Research* **156**, 187–216.

Sisson, T. W. & Grove, T. L. (1993). Experimental investigations of the role of H_2O in calc-alkaline differentiation and subduction zone magmatism. *Contributions to Mineralogy and Petrology* **113**, 143–166.

Sisson, T. W., Ratajeski, K., Hankins, W. B. & Glazner, A. F. (2005). Voluminous granitic magmas from common basaltic sources. *Contributions to Mineralogy and Petrology* **148**, 635–661.

Smith, I. E. M. & Price, R. C. (2006). The Tonga–Kermadec arc and Havre–Lau backarc system: Their role in the development of tectonic and magmatic models for the western Pacific. *Journal of Volcanology and Geothermal Research* **156**, 315–331.

Smith, I. E. M., Brothers, R. N., Muiruri, F. G. & Browne, P. R. L. (1988). The geochemistry of rock and water from samples from Curtis Island volcano, Kermadec Group, southwest Pacific. *Journal of Volcanology and Geothermal Research* **34**, 233–240.

Smith, I. E. M., Stewart, R. B. & Price, R. C. (2003*a*). The petrology of a large intraoceanic silicic eruption: the Sandy Bay Tephra, Kermadec Arc, Southwest Pacific. *Journal of Volcanology and Geothermal Research* **124**, 173–194.

Smith, I. E. M., Worthington, T., Stewart, R. B., Price, R. C. & Gamble, J. A. (2003*b*). Felsic volcanism in the Kermadec arc, SW Pacific: crustal recycling in an oceanic setting. In: Larter, R. D. & Leat, P. T. (eds) *Intra-Oceanic Subduction Systems: Tectonic and Magmatic Processes. Geological Society*, London: Special Publications **219**99–118.

Smith, I. E. M., Worthington, T. J., Price, R. C., Stewart, R. B. & Maas, R. (2006). Petrogenesis of dacite in an oceanic subduction environment: Raoul Island, Kermadec arc. *Journal of Volcanology and Geothermal Research* **156**, 252–265.

Smith, I. E. M., Stewart, R. B., Price, R. C. & Worthington, T. J. (2010). Are arc-type rocks the products of magma crystallisation? Observations from a simple oceanic arc volcano: Raoul Island, Kermadec Arc, SW Pacific. *Journal of Volcanology and Geothermal Research* **190**, 219–234.

Smith, V. C., Blundy, J. D. & Arce, J. L. (2009). A temporal record of magma accumulation and evolution beneath Nevado de Toluca, Mexico, preserved in plagioclase phenocrysts. *Journal of Petrology* **50**, 405–426.

Sun, S. S. & McDonough, W. F. (1989). Chemical and isotopic systematics of oceanic basalts: implications for mantle composition and process. In: Saunders, A. D. & Norry, M. J. (eds) *Magmatism in the Ocean Basins. Geological Society*, London: Special Publications **42**, 313–345.

Tamura, Y. & Tatsumi, Y. (2002). Remelting of an andesitic crust as a possible origin for rhyolitic magma in oceanic arcs: an example from the Izu–Bonin arc. *Journal of Petrology* **43**, 1029–1047.

Tamura, Y. & Wysoczanski, R. J. (2006). Silicic volcanism and crustal evolution in oceanic arcs: Introduction. *Journal of Volcanology and Geothermal Research* **156**, v–vii.

Tamura, Y., Gill, J. B., Tollstrup, D., Kawabata, H., Shukuno, H., Chang, Q., Miyazaki, T., Takahashi, T., Hirahara, Y., Kodaira, S., Ishizuka, O., Suzuki, T., Kido, Y., Fiske, R. S. & Tatsumi, Y. (2009). Silicic magmas in the Izu–Bonin oceanic arc and implications for crustal evolution. *Journal of Petrology* **50**, 685–723.

Tani, K., Kawabata, H., Chang, Q., Sato, K. & Tatsumi, Y. (2003). Quantitative analyses of silicate rock major and trace elements by X-ray fluorescence spectrometer: Evaluation of analytical precision and sample preparation. *Frontier Research on Earth Evolution* **2**, Article 2-16, 8 pp.

Tani, K., Fiske, R. S., Tamura, Y., Kido, Y., Naka, J., Shukuno, H. & Takeuchi, R. (2008). Sumisu volcano, Izu–Bonin arc, Japan: site of a silicic caldera-forming eruption from a small open-ocean island. *Bulletin of Volcanology* **70**, 547–562.

Tatsumi, Y. & Eggins, S. M. (1995). *Subduction Zone Magmatism*. Cambridge, MA: Blackwell Science, 211 pp.

Turner, S., Hawkesworth, C. J., Rogers, N. W. B., Bartlett, J., Worthington, T. J., Hergt, J., Pearce, J. A. & Smith, I. E. M. (1997). ^{238}U–^{230}Th disequilibria, magma petrogenesis, and flux rates beneath the depleted Tonga–Kermadec island arc. *Geochimica et Cosmochimica Acta* **61**, 4855–4884.

Ukstins-Peate, I., Kent, A. J. R., Baker, J. A. & Menzies, M. A. (2008). Extreme geochemical heterogeneity in Afro-Arabian Oligocene tephras: Preserving fractional crystallization and mafic recharge processes in silicic magma chambers. *Lithos* **102**, 260–278.

Vigneresse, J. L., Barbey, P. & Cuney, M. (1996). Rheological transitions during partial melting and crystallization with application to felsic magma segregation and transfer. *Journal of Petrology* **37**, 1579–1600.

Vogel, T. A., Patino, L. C., Alvarado, G. E. & Gans, P. B. (2004). Silicic ignimbrites within the Costa Rican volcanic front: evidence for the formation of continental crust. *Earth and Planetary Science Letters* **226**, 149–159.

Vogel, T. A., Patino, L. C., Eaton, J. K., Valley, J. W., Rose, W. I., Alvarado, G. E. & Viray, E. L. (2006). Origin of silicic magmas along the Central American volcanic front: Genetic relationship to mafic melts. Journal of Volcanology and Geothermal Research **156**, 217–228.

Wade, J. A., Plank, T., Stern, R. J., Tollstrup, D. L., Gill, J. B., O'Leary, J. C., Eiler, J. M., Moore, R. B., Woodhead, J. D., Trusdell, F., Fischer, T. P. & Hilton, D. R. (2005). The May 2003 eruption of Anatahan volcano, Mariana Islands: Geochemical evolution of a felsic island-arc volcano. *Journal of Volcanology and Geothermal Research* **146**, 139–170.

Wallace, L., Reyners, M., Cochran, U., Bannister, S., Barnes, P. M., Berryman, K., Downes, G., Eberhart-Phillips, D., Fagereng, A., Ellis, S., Nicol, A., McCaffrey, R., Beavan, R. J., Henrys, S., Sutherland, R., Barker, D. H. N., Litchfield, N., Townend, J., Robinson, R., Bell, R., Wilson, K. & Power, W. (2009). Characterizing the seismogenic zone of a major plate boundary subduction thrust: Hikurangi Margin, New Zealand. *Geochemistry, Geophysics, Geosystems* **10**, Q10006, doi:10.1029/2009GC002610.

Wilson, C. J. N. & Charlier, B. L. A. (2009). Rapid rates of magma generation at contemporaneous magma systems, Taupo volcano, New Zealand: insights from U–Th model-age spectra in zircons. *Journal of Petrology* **50**, 875–907.

Wilson, C. J. N., Houghton, B. F., McWilliams, M. O., Lanphere, M. A., Weaver, S. D. & Briggs, R. M. (1995). Volcanic and structural evolution of Taupo Volcanic Zone, New Zealand: a review. *Journal of Volcanology and Geothermal Research* **68**, 1–28.

Wilson, C. J. N., Blake, S., Charlier, B. L. A. & Sutton, A. N. (2006). The 26·5 ka Oruanui eruption, Taupo volcano, New Zealand: development, characteristics and evacuation of a large rhyolitic magma body. *Journal of Petrology* **47**, 35–69.

Woods, A. W. & Cowan, A. (2009). Magma mixing triggered during volcanic eruptions. *Earth and Planetary Science Letters* **288**, 132–137.

Worthington, T. J. (1998). Geology and petrology of Raoul volcano: magma genesis and fractionation processes beneath the Tonga–Kermadec arc. PhD thesis, University of Auckland.

Worthington, T. J., Gregory, M. R. & Bondarenko, V. (1999). The Denham Caldera on Raoul Volcano: dacite volcanism in the Tonga–Kermadec arc. *Journal of Volcanology and Geothermal Research* **90**, 29–48.

Wright, I. C. (1993). Pre-spread rifting and heterogeneous volcanism in the southern Havre Trough back-arc basin. *Marine Geology* **113**, 179–200.

Wright, I. C. (1994). Nature and tectonic setting of the southern Kermadec submarine arc volcanoes: An overview. *Marine Geology* **118**, 217–236.

Wright, I. C. (1996). Volcaniclastic processes on modern submarine arc stratovolcanoes: sidescan and photographic evidence from the Rumble IV and V volcanoes, southern Kermadec Arc (SW Pacific). *Marine Geology* **136**, 21–39.

Wright, I. C. (1997). Morphology and evolution of the remnant Colville and active Kermadec Arc ridges south of 33°30'S. *Marine Geophysical Researches* **19**, 177–193.

Wright, I. C. (2001). In situ modification of modern submarine hyaloclastic/pyroclastic deposits by ocean currents: an example from the Southern Kermadec arc (SW Pacific). *Marine Geology* **172**, 287–307.

Wright, I. C. & Gamble, J. A. (1999). Southern Kermadec submarine caldera arc volcanoes (SW Pacific): caldera formation by effusive and pyroclastic eruption. *Marine Geology* **161**, 207–227.

Wright, I. C., Stoffers, P., Hannington, M., de Ronde, C. E. J., Herzig, P., Smith, I. E. M. & Browne, P. R. L. (2002). Towed-camera investigations of shallow–intermediate water-depth submarine stratovolcanoes of the southern Kermadec arc, New Zealand. *Marine Geology* **185**, 207–218.

Wright, I. C., Gamble, J. A. & Shane, P. A. R. (2003). Submarine silicic volcanism of the Healy caldera, southern Kermadec arc (SW Pacific): I—volcanology and eruption mechanisms. *Bulletin of Volcanology* **65**, 15–29.

Wright, I. C., Worthington, T. J. & Gamble, J. A. (2006). New multibeam mapping and geochemistry of the 30°–35° S sector, and overview, of southern Kermadec arc volcanism. *Journal of Volcanology and Geothermal Research* **149**, 263–296.

Wysoczanski, R. J., Todd, E., Wright, I. C., Leybourne, M. I., Hergt, J. M., Adam, C. & Mackay, K. (2010). Backarc rifting, constructional volcanism and nascent disorganised spreading in the southern Havre Trough backarc rifts (SW Pacific). *Journal of Volcanology and Geothermal Research* **190**, 39–57.